====================== **TOKAMAKS** ======================

# MHD Limits in the T-15M Tokamak

## S. Yu. Medvedev* and V. D. Pustovitov**

*\*Keldysh Institute of Applied Mathematics, Russian Academy of Sciences, Miusskaya pl. 4, Moscow, 125047 Russia*
*\*\*Russian Research Centre Kurchatov Institute, pl. Kurchatova 1, Moscow, 123182 Russia*
Received February 14, 2003; in final form, April 17, 2003

**Abstract**—The problem of plasma MHD stability in the T-15M tokamak is considered in realistic geometry. Stability of the external kink modes with the toroidal wavenumbers $n = 1, 2$, and 3 is numerically investigated in equilibrium configurations similar to the systematically analyzed steady-state configurations with reversed shear in ITER. The stability limits in T-15M are found with and without account taken of the stabilizing influence of the first wall. The results of the calculations are used to compare T-15M with ITER. The stabilizing effect resulting from reducing the distance between the first wall and the plasma in T-15M is evaluated. © *2003 MAIK "Nauka/Interperiodica".*

## 1. INTRODUCTION

The projects of upcoming fusion devices are based on thoroughly elaborated physical evaluations providing a clear idea of the operational limits [1–17]. One of the major characteristics is the $\beta$ limit (the ratio of the plasma pressure to the magnetic pressure) since, at a given magnetic field, the specific fusion power is proportional to $\beta^2$. Continuous attention to the problem of $\beta$ limits is also related to the fact that even in tokamaks, which are closer to a reactor than other systems, the achievable values of $\beta$ are obviously insufficient for reliable extrapolations and the decisive step toward a reactor. Theoretical and experimental results inevitably lead to the conclusion that, at present, a prototype of a fusion reactor can only be a tokamak operating in a rather extreme regime, actually near the $\beta$ limit. Therefore, an increase in the $\beta$ limit and the study of the physics of high-$\beta$ plasma discharges in tokamaks remain the main problems of present-day research on tokamaks.

In recent years, the possibility of constructing the T-15M tokamak at the Kurchatov Institute has been discussed [18]. The achievement of high $\beta$ values is considered to be one of the main objectives of the T-15M experimental program. On the whole, the dimensions and main engineering parameters of this device have already been specified. The present study is a first step in the physical evaluation of the T-15M project from the viewpoint of operational $\beta$ limits.

It is known that the problems of plasma equilibrium in tokamaks are being solved quite efficiently, and that the restrictions on $\beta$ arise from plasma instabilities [1]. It is also known that the predictions of MHD theory provide a reliable guide in estimating the $\beta$ limits [1, 19]. In all the projects of fusion devices, MHD calculations are a necessary and rather important element of the physical assessment. Such work must be done before arriving at a final decision on the T-15M project. Here, we consider the problem of plasma stability in the

T-15M tokamak within classical ideal magnetohydrodynamics. The purpose of the present study is to determine the MHD limits caused by the ideal modes for a given geometry of T-15M with account taken of the stabilizing influence of its first wall. The shape of the wall is a factor that substantially affects the result and is the reason for the difference between T-15M and ITER, from the standpoint of the MHD ideal limits.

The T-15M tokamak is being planned as an ITER-like device. Its operation should be coordinated with the ITER program in order to contribute as much as possible to solving the basic problems of the tokamak reactor. Naturally, any theoretical analysis of T-15M should be organized so that the results obtained can be easily compared with those for ITER. Following this principle, we lean here on the earlier results of MHD and transport calculations for ITER [20, 21], using them as initial data. The calculations for T-15M are performed here in the same way, using the same means as described in [21].

In Section 2, the statement of the equilibrium problem for an ITER-like configuration with T-15M parameters is described. In Section 3, the results of calculations of the plasma stability limits set by the ideal external kink modes in T-15M are discussed. In the conclusion, the results obtained are summarized.

## 2. EQUILIBRIUM CONFIGURATIONS

To study the plasma stability in T-15M, we chose scenarios similar to the 4A ITER scenario with noninductive (stationary) current drive, described in detail in [20, 21]. To obtain ITER-like equilibrium plasma configurations with the T-15M dimensions, we rescale the initial ITER configurations so that the radius of the plasma center is $R = 1.55$ m. In so doing, the dimensionless parameters describing the plasma shape are kept unchanged. The basic characteristics of the equi-

Main parameters of the analyzed equilibrium configurations in the T-15M

| Equilibrium | 1 | 2 |
|---|---|---|
| $a$, m | 0.5 | " |
| $\delta_{95}$ | 0.39 | " |
| $\kappa_{95}$ | 1.76 | " |
| $R$, m | 1.55 | " |
| $B(R)$, T | 2.5 | " |
| $I$, MA | 1.4125 | " |
| $q_{95}$ | 4.14 | 4.14 |
| $q_{\min}$ | 2.16 | 1.66 |
| $\beta_N$ | 3.53 | 3.74 |
| $p_0/\bar{p}$ | 2.55 | 3.1 |
| $l_i$ | 0.58 | 0.74 |

librium configurations, whose stability is analyzed below, are given in the table. Here, as in [21], we solve the equilibrium problem for T-15M with a fixed plasma boundary whose shape exactly replicates a standard separatrix in the 4A ITER scenario.

The first equilibrium corresponds exactly to one of the equilibrium configurations adopted for ITER scenarios (the fourth column in Table 1 in [21], the 4A scenario), differing only in smaller $a$ and $R$ and smaller values of the magnetic field and net current. Briefly, the plasma shape prescribed in our calculations for T-15M is the ITER shape with a separatrix at the boundary. The values of $q_{95}$ and $q_{\min}$ also coincide here with those in ITER, so the first equilibrium is an exact analogue of the 4A scenario [21]. The second equilibrium differs from the first by the choice of the profiles, in particular by a smaller value of $q_{95}$ and larger peaking factor of the plasma pressure, $p_0/\bar{p} = 3.1$, where $p_0$ is the plasma pressure at the magnetic axis and $\bar{p}$ is the volume-averaged pressure. As a measure of $\beta$, we use here the widely accepted Troyon factor

$$\beta_N = \beta[\%]\frac{a\ [\text{m}]\ B\ [\text{T}]}{I\ [\text{MA}]}, \qquad (1)$$

where $a$ is the minor radius of the plasma, $B$ is the magnetic field, and $I$ is the net current in the plasma.

Let us note in advance that the $\beta_N$ values given in the table for the two equilibrium states in T-15M are actually far in the unstable region. However, the first equilibrium would be stable if the first wall of T-15M were similar to the ITER wall.

The problem of plasma equilibrium in a tokamak is reduced to solving the Grad–Shafranov equation [22], which can be written as

$$\mu_0 j_\varphi = -\frac{r}{2\pi}\boldsymbol{\nabla}\cdot\frac{\boldsymbol{\nabla}\psi}{r^2}, \qquad (2)$$

where $\psi$ is the poloidal flux, related to the magnetic field $\mathbf{B}$ by the equality

$$2\pi\mathbf{B} = \boldsymbol{\nabla}\psi\times\boldsymbol{\nabla}\varphi + F\boldsymbol{\nabla}\varphi, \qquad (3)$$

and $j_\varphi$ is the toroidal component of the current density $\mathbf{j} = \boldsymbol{\nabla}\times\mathbf{B}/\mu_0$ (in SI units), which, for an axially symmetric equilibrium configuration, is explicitly expressed through poloidal current $F$ and the plasma pressure $p$:

$$2\pi p'(\psi) = \mathbf{j}\cdot\boldsymbol{\nabla}\varphi - \frac{FF'(\psi)}{2\pi\mu_0 r^2}. \qquad (4)$$

Hereinafter, $r$, $\varphi$, and $z$ are the cylindrical coordinates attached to the main axis of the tokamak.

Following the procedure in [21], we consider below equilibrium configurations with the parameters given in the table. The toroidal current density $j_\varphi$ in Eq. (2) is given by the formula

$$j_\varphi = j_n\left\{\frac{r}{R}\alpha G(\psi) + \frac{R}{r}[H(\psi) - \alpha G(\psi)]\right\}, \qquad (5)$$

where $j_n$ is a constant determining the net current in the plasma; $G$ and $H$ are the functions corresponding at $\alpha = 1$ to self-consistently calculated steady state ITER scenarios [21]; $R$ is, generally speaking, an arbitrary constant not necessarily equal to the major radius of the device. Let us say that $\alpha = 1$ gives the main equilibrium state. Varying $\alpha$ at fixed $G$ and $H$ and, accordingly, the given profiles of the pressure and current density, we can consider similar equilibria with different values of $\beta$. The profiles of the current density, pressure, and other characteristics of the main state (the first equilibrium) are shown in Fig. 1. In the main state, we have $p_0/\bar{p} = 2.55$, where $p_0$ is the plasma pressure at the magnetic axis and $\bar{p}$ is the volume-averaged pressure. In addition to the main state, we will also consider the second equilibrium with a larger pressure peaking factor, $p_0/\bar{p} = 3.1$. The peakedness of the pressure profile is an important factor determining the plasma stability, especially in configurations with reversed shear. The profiles of the equilibrium plasma parameters for the second scenario considered here are shown in Fig. 2. The bootstrap current density shown in Figs. 1 and 2 was calculated by Hirshman's formulas [23] in the low-collisional approximation (the "banana" regime) at similar profiles of the density and temperature.

Under the procedure in given boundary conditions, the properties of equilibrium configurations are completely determined by the functions $G$ and $H$ in Eq. (5). One can express them explicitly through the equilib-
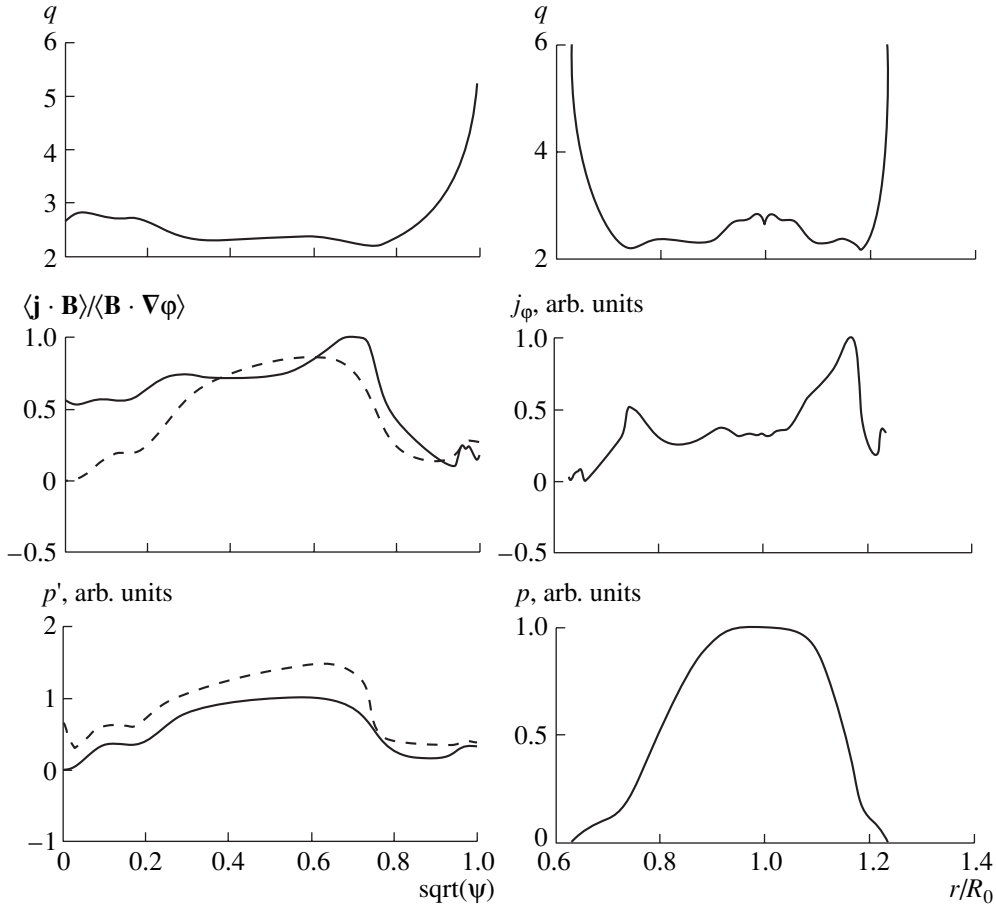
**Fig. 1.** Calculated profiles of the equilibrium plasma parameters for the main scenario with a pressure peaking factor of $p_0/\bar{p} = 2.55$. All the parameters, except for the safety factor $q$, are normalized to their maximum values. On the left, the profiles are shown as functions of the square root of the normalized poloidal flux of the magnetic field (zero at the magnetic axis and unity at the plasma boundary). On the right, the profiles are shown in the equatorial plane, which passes through the magnetic axis, as functions of the major radius normalized to the radius $R_0$ of the magnetic axis. In addition to the profile of $\langle \mathbf{j} \cdot \mathbf{B} \rangle / \langle \mathbf{B} \cdot \nabla\varphi \rangle$, the dashed line shows, in the same units, the profile of $\langle \mathbf{j}_{bs} \cdot \mathbf{B} \rangle / \langle \mathbf{B} \cdot \nabla\varphi \rangle$, where $\mathbf{j}_{bs}$ is the bootstrap current density calculated in the low-collisional approximation (the "banana" regime) [23] at similar profiles of the density and temperature. In addition to the profile of $p' = dp/d\psi$, the dashed line shows the limit of $p'$ set by ballooning instability. Here, $p_0 = 2.5 \times 10^5$ Pa, $j_{max} = 2.9 \times 10^6$ A/m$^2$, $R_0 = 1.66$ m, $\beta = 0.039884$, $I_N = 1.13$, and $\beta_N = 3.5296$.

rium characteristics, comparing Eq. (5) with a consequence of Eq. (4),

$$j_\varphi = 2\pi R\left\{\frac{r}{R}p'(\psi) + \frac{R}{r}\left\langle \frac{R^2}{r^2}\right\rangle^{-1}\left[\frac{dJ}{dV} - p'(\psi)\right]\right\}, \quad (6)$$

where

$$J = \frac{1}{2\pi}\int_V \mathbf{j} \cdot \nabla\varphi \, dV \qquad (7)$$

is the longitudinal current flowing inside a magnetic surface; $V$ is the volume enclosed by this surface; and the angular brackets stand for the canonical averaging

over the volume between the neighboring magnetic surfaces,

$$\langle X \rangle = \frac{d}{dV}\int_V X \, dV. \qquad (8)$$

In a general case, we have

$$j_n \alpha G(\psi) = 2\pi R p'(\psi), \qquad (9)$$

$$j_n H(\psi)$$
$$= 2\pi R\left\langle \frac{R^2}{r^2}\right\rangle^{-1}\frac{dJ}{dV} + 2\pi R p'(\psi)\left[1 - \left\langle \frac{R^2}{r^2}\right\rangle^{-1}\right]. \qquad (10)$$

At any $R$, the function $G$ is determined by the plasma pressure profile only. The function $H$ can be made
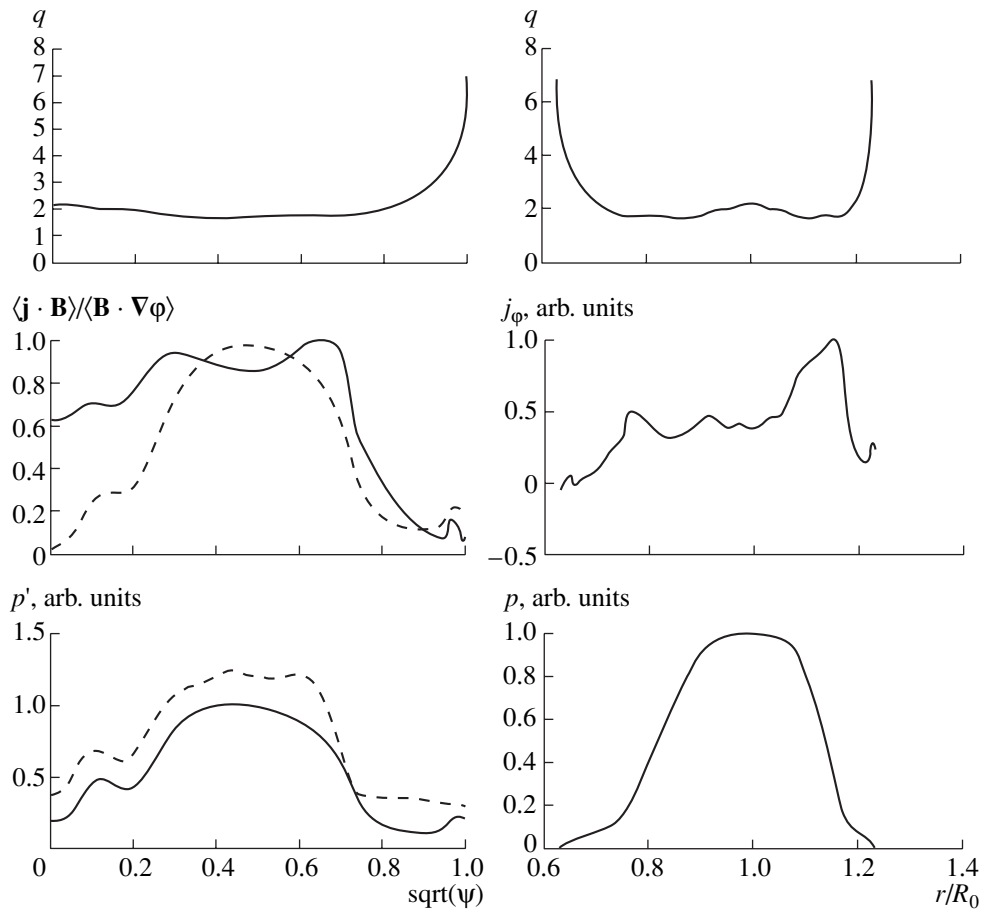
**Fig. 2.** Calculated profiles of the same equilibrium parameters as those in Fig. 1, but for a scenario with an increased pressure peaking factor, $p_0/\bar{p} = 3.1$. Here, $p_0 = 3.2 \times 10^5$ Pa, $j_{max} = 3.1 \times 10^6$ A/m$^2$, $R_0 = 1.66$ m, $\beta = 0.0422$, $I_N = 1.13$, and $\beta_N = 3.7377$.
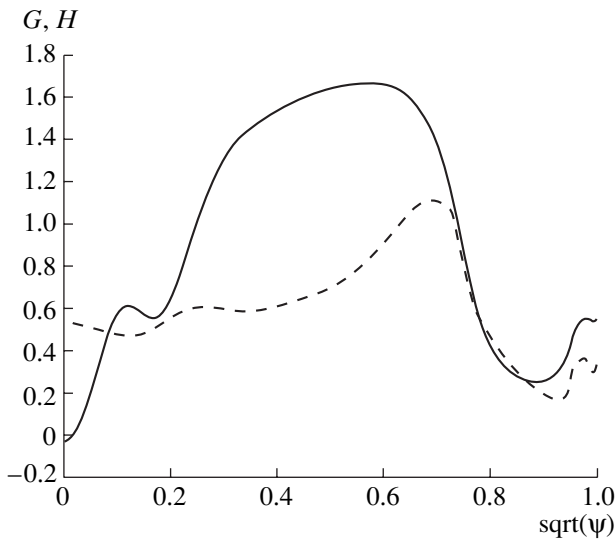


**Fig. 3.** Functions $G$ (solid line) and $H$ (dashed line) for series of equilibrium configurations with $p_0/\bar{p} = 2.55$, illustrated by Fig. 1.

dependent only on the current profile by choosing $R$ satisfying the condition $\langle R^2/r^2 \rangle = 1$. It is clear that the dependence of $H$ on $J$ also remains dominant at other $R$ close to this value. For example, one can take $R$ to be equal to the radius of the plasma column axis. With such a choice, by varying $\alpha$, we obtain a series of equilibrium configurations with almost the same profile of $q$.

The functions $G$ and $H$, which are used here to specify the current density, are shown in Figs. 3 and 4. These functions were obtained in a series of self-consistent transport calculations [21] with the use of the ASTRA code [24]. The purpose of these calculations was the optimization of the ITER discharge scenarios over a number of parameters. With given sources of plasma heating (neutral beams) and with lower hybrid current drive at the plasma periphery, it was required to obtain a steady-state scenario with an internal transport barrier, reversed shear in the central region, a given peakedness of the pressure profile, a large fraction of the bootstrap current, and an acceptable level of convective and diffusive losses through the separatrix. Accordingly, realistic self-consistent boundary condi-

tions for the ion and electron densities and temperatures were set at the separatrix, and moderate absolute values of the transport coefficients were used in calculations.

In both experiment and theory, a combination of necessary tokamak characteristics can only be obtained by carefully balancing mutually exclusive requirements. Whether or not it will be possible to realize them in T-15M depends on the device instrumentation. Here, we use the ITER functions $G$ and $H$ for the purpose of easy comparison of the results obtained for T-15M with those for ITER. For an ITER-like device, such an approach is quite logical (especially as a first step), taking into account that the possible scenarios of T-15M operation are not yet finally determined.

## 3. STABILITY LIMITS FOR IDEAL EXTERNAL KINK MODES

It is known that the ideal MHD stability theory gives reliable predictions of the $\beta$ limits, which indeed manifest themselves as real restrictions in tokamak experiments [1, 19]. The most dangerous of these are the large-scale modes seizing the greater part of the plasma column. Here, we study the stability of plasma equilibrium in the T-15M tokamak against external kink modes with the toroidal wavenumbers $n = 1$, 2, and 3. The calculations show that, for the configurations under study, the lowest level of the $\beta$ limit is set by the $n = 1$ mode. It is these limits that are discussed below.

The plasma stability in T-15M was simulated with the help of the KINX code [25]. This code allows one to investigate the stability of equilibrium in axially symmetric systems (including configurations with a separatrix) within the linear ideal magnetohydrodynamics. The KINX code was successfully applied to studying the global kink mode stability in various equilibrium configurations, such as conventional tokamaks [21], configurations with several magnetic axes and internal separatrix ("doublets") [25], and tokamaks with a small aspect ratio [26]. The code was also used to calculate the stability of MHD modes that have large toroidal wavenumbers and are localized near the plasma boundary [27], i.e., modes that can be responsible for so-called ELMs.

We obtained a series of equilibrium configurations with various values of the normalized $\beta_N = 100\beta/I_N$ by varying the parameter $\alpha$ in Eq. (5) while keeping fixed the normalized current

$$I_N \equiv \frac{I \text{ [MA]}}{a \text{ [m] } B_0 \text{ [T]}}, \qquad (11)$$

where $I$ is the net plasma current, $a$ is the minor plasma radius, and $B_0$ is the vacuum magnetic field at the plasma center. Here, $\beta$ is defined by the equality $\beta = 2\mu_0\bar{p}/B_0^2$. The value of $I_N$ is controlled by changing $j_n$ in Eq. (5).
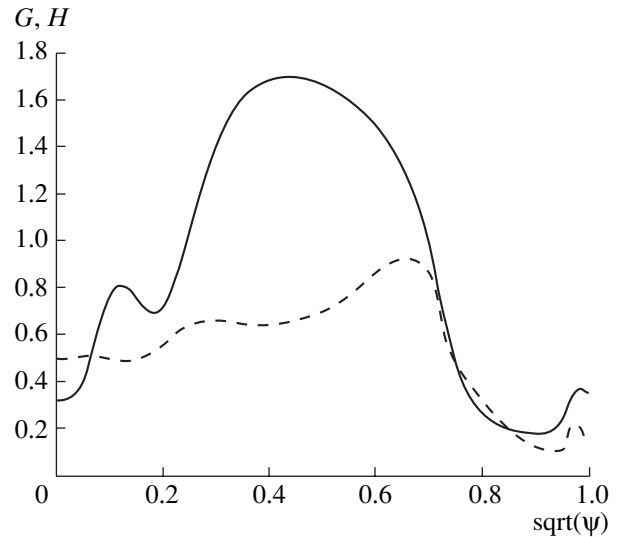


**Fig. 4.** Functions $G$ (solid line) and $H$ (dashed line) for a series of equilibrium configurations with $p_0/\bar{p} = 3.1$, illustrated by Fig. 2.

In a tokamak, the stability of ideal kink modes essentially depends on the boundary conditions, in particular, on the position of the conducting wall with respect to the plasma [1, 28]. This was always known in theory and quite recently this was convincingly confirmed by the experiments carried out in the DIII-D tokamak [29, 30]. It is now an established fact that, in a tokamak with low or reversed shear and a large fraction of the bootstrap current (the so-called "advanced operation" regime [31–33]) large $\beta$ could be obtained if the kink modes with low $n$ were stabilized by a conducting wall [34].

A real wall with finite conductivity can stabilize external kink modes only during a finite time interval of about the diffusion time of the magnetic field through the wall, $\tau_w$, which, in the cylindrical approximation, is defined by the formula $\tau_w = \mu_0\sigma_w d_w r_w$, where $\sigma_w$, $r_w$, and $d_w$ are the conductivity, minor radius, and thickness of the wall, respectively (estimates for T-15M yield $\tau_w = 6.35 \times 10^{-3}$ s). The wall reacts as an ideal conductor to fast perturbations with a characteristic time smaller than $\tau_w$, whereas for very slow perturbations, the influence of the wall on the perturbation structure can be completely ignored. Thus, two representative parameters naturally appear in the problem:

(i) the parameter $\beta_N^{\text{wall}}$, which is the stability limit for ideal MHD modes with account taken of the wall as an ideal conductor, and

(ii) the parameter $\beta_N^{\text{no wall}}$, which is the MHD limit calculated for the same configuration, but without a conducting wall.

These values can be precisely determined only with the help of MHD codes. Here, they are calculated for
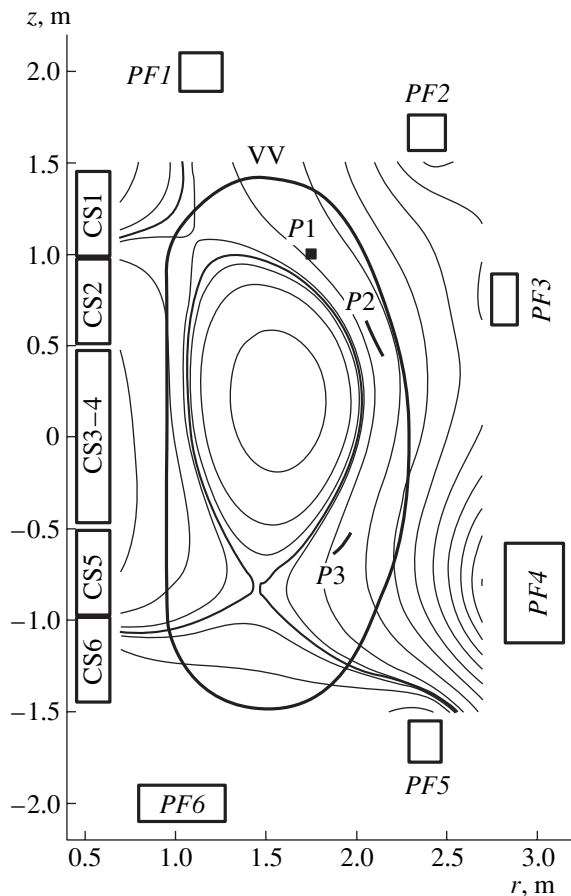
**Fig. 5.** Poloidal cross-section of the T-15M tokamak [35]: (CS1–CS6) sections of the central solenoid, (PF1–PF6) windings of the poloidal magnetic field, (VV) vacuum vessel, and (P1–P3) windings of the passive stabilization system. The $\psi$ = const contours are shown for the stationary phase of the Ohmic discharge scenario.



**Fig. 6.** Dependence of the $n = 1$ mode stability limit $\beta_N$ on the normalized current $I_N$ for scenarios with reversed shear in the T-15M tokamak. The circles show the results of calculations for $p_0/\bar{p} = 2.55$, and the squares are for $p_0/\bar{p} = 3.1$. The open symbols correspond to $\beta$ limits without wall stabilization ($\beta_N^{\text{no wall}}$), and the closed symbols show the $\beta_N^{\text{wall}}$ limit for the case in which the T-15M wall is considered ideal. The dashed line shows $q_{\min}$ for a configuration with $p_0/\bar{p} = 2.55$ and $\alpha = 1$.

the T-15M tokamak with the use of the KINX code [25]. The geometry of the tokamak, the shape of the vacuum chamber, and its parameters (the thickness and conductivity of the wall) are taken from the technical project of the T-15M tokamak [18]. The geometry of the problem is illustrated by Fig. 5 [35].

Numerous computational and experimental data [1, 36] show that

$$\beta_N^{\text{no wall}} \approx 4l_i, \qquad (12)$$

where $l_i$ is the internal inductance of the plasma column per unit length. The value defined by formula (12) is called an empirical scaling or a rigid limit on $\beta$. The approximate equality in formula (12) reflects rather substantial scatter in the data. More precisely, the quantity $4l_i$ should be regarded as an estimate of the upper limit, since a resistive wall mode (RWM) can become unstable even at an appreciably smaller $\beta_N$, e.g., at $\beta_N = 2.5l_i$ [19]. It was stated in [19] that the dependences observed in the DIII-D tokamak can be described by a
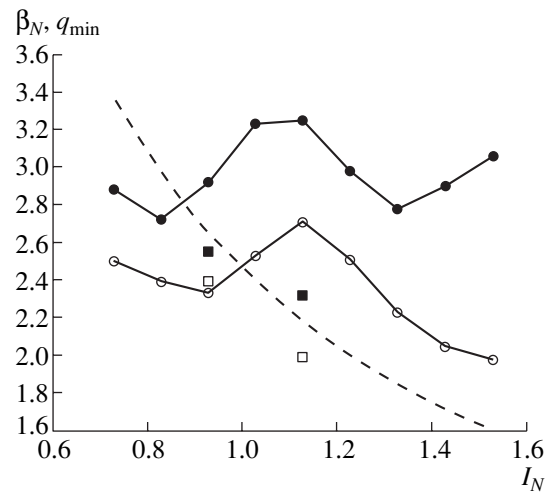
scaling $\beta_N^{\text{no wall}} = kl_i$ with $k \le 4$, where $k$ is constant for a given discharge. In any case, these scalings emphasize the dependence of $\beta_N^{\text{no wall}}$ on $l_i$.

The internal inductance $l_i$ is an integral characteristic of the current profile. Here, it is defined as

$$l_i = 2\overline{B_\theta^2}V/(\mu_0^2 I^2 R), \qquad (13)$$

where $B_\theta$ is the poloidal field and $V$ is the plasma volume. For a circular plasma, this definition reduces to

$$l_i = \overline{B_\theta^2}/B_J^2, \qquad (14)$$

where $B_J = B_\theta(b)$ is the poloidal field at the plasma boundary. Large $l_i$ can be obtained only for peaked distributions of $j_\varphi$. However, an advanced operation regime with low or negative shear requires wide current distributions that yield small $l_i$ and, accordingly, the low $\beta_N^{\text{no wall}}$ limit.

The results of numerical calculations of the limits $\beta_N^{\text{wall}}$ and $\beta_N^{\text{no wall}}$ in the T-15M tokamak for the $n = 1$ mode at different values of the normalized current are shown in Fig. 6. The calculations were performed for an ITER-like configuration with parameters given in the table. Therefore, the $\beta_N^{\text{no wall}}$ values shown in Fig. 6 equally represent both T-15M and ITER. However, the
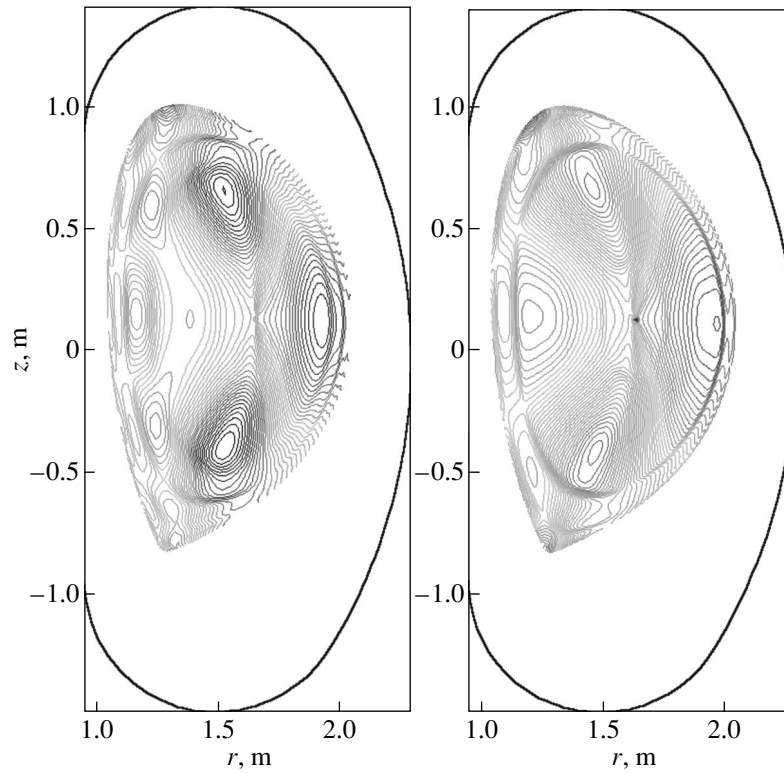
**Fig. 7.** Structure of the $n = 1$ mode for a plasma with different values of the normalized current: $I_N = 1.13$ (on the left) and $I_N = 1.53$ (on the right). In both cases, $\beta_N = 3.5$ and $p_0/\bar{p} = 2.55$. The instability growth rates calculated with account taken of the stabilizing influence of the T-15M wall, which are shown by the bold contour, satisfy $\gamma\tau_A = 0.02$ and $0.01$, respectively, where $\tau_A$ is the Alfvén time. The calculated structure of the modes is shown by the contour lines of $\xi_n$, which is the component of the plasma displacement normal to the magnetic surfaces.

values of $\beta_N^{\text{wall}}$ in T-15M and ITER should certainly be different because the shape and position of the vacuum vessel with respect to the plasma is different in these devices. This point will be discussed in more detail below.

The calculated $\beta_N^{\text{no wall}}$ limits shown by the open symbols in Fig. 6 are, on average, close to scaling (12), which yields $\beta_N \approx 2.4$ for an ITER-like configuration (the first equilibrium). At the same time, for the second equilibrium with a larger pressure peakedness, we have obtained (in the obvious contradiction with formula (12)) a lower $\beta_N^{\text{no wall}}$ limit at a larger internal inductance (the open squares in Fig. 6). Thus, as well as in the above case with DIII-D [19], the dependence $\beta_N^{\text{no wall}} = kl_i$ should be regarded as more correct. For all the cases considered here, the $\beta_N^{\text{no wall}}/l_i$ variation covers a range from 2.7 to 4.5 (the value 2.7 is obtained for $p_0/\bar{p} = 3.1$ and $q_{\text{min}} = 1.8$). In particular, for the maximum values of $\beta_N^{\text{no wall}}$ in Fig. 6, in both cases corresponding to the same values of $q_{\text{min}}$ but different values

of $p_0/\bar{p}$, the simulations give $k \equiv \beta_N^{\text{no wall}}/l_i = 4.5$ for a maximum $\beta_N^{\text{no wall}} = 2.7$ on the lower curve and $k = 3.2$ for $\beta_N^{\text{no wall}} = 2.4$ (the upper open square). Note that, in addition to the pressure peakedness, the second important factor determining the value of $\beta_N^{\text{no wall}}$ in configurations with reversed shear is the position of $q_{\text{min}}$ with respect to the surfaces with resonant $q$ values of 2 and 3. The maximum value of $\beta_N^{\text{no wall}}$ ($\beta_N^{\text{no wall}} = 2.7$) on the lower curve is achieved at an intermediate value of $q_{\text{min}}$.

The calculated values of $\beta_N^{\text{no wall}}$ for the $n = 2$ and $n = 3$ modes are much larger than those for the most unstable $n = 1$ mode. For example, for the first equilibrium, the $\beta_N^{\text{no wall}}$ stability limits for these higher modes are 3.7 and 4.3, respectively.

The quantity $\beta_N^{\text{wall}}$ is the ideal limit, so that it is impossible to achieve higher $\beta_N$ in a tokamak under any conditions. The higher the value of $\beta_N^{\text{wall}}$ with respect to $\beta_N^{\text{no wall}}$, the stronger the stabilizing influence of the
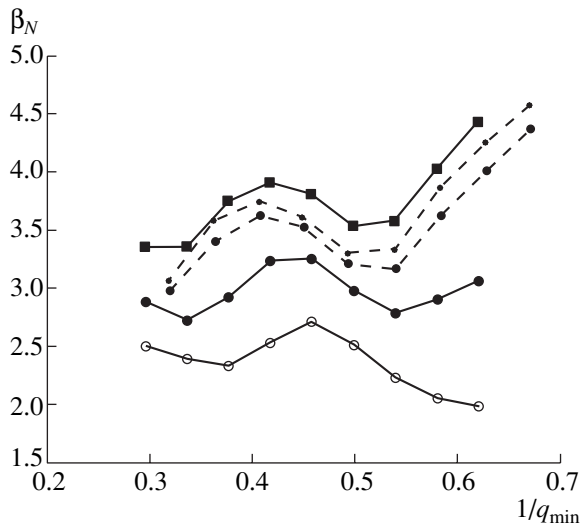
**Fig. 8.** Dependence of the $\beta_N$ limits on $q_{\min}$ in the T-15M tokamak plasma for different positions of the conducting wall. In all cases, $p_0/\bar{p} = 2.55$. In addition to the two curves presented in Fig. 6 (open circles for $\beta_N^{\text{no wall}}$ and closed circles for $\beta_N^{\text{wall}}$), the $\beta_N^{\text{wall}}$ limits are shown by squares for a configuration with an ITER-like wall and by dashed lines for a T-15M configuration with a plasma shifted by 10 cm along the $R$ axis (small circles) and along both axes (dots).



**Fig. 9.** Plasma boundary (light solid line) and the position of the T-15M wall (heavy line). The dashed and dotted lines show the plasma boundary shifted outward by 10 cm and the rescaled ITER wall, respectively.

wall. Figure 6 shows that, in the T-15M tokamak, the gap between these limits is not large. This actually means that the wall is far from the plasma. To increase $\beta_N^{\text{wall}}$ in T-15M, it is necessary to place the vacuum chamber closer to the plasma.

The main scenario, the parameters of which are given in the table, corresponds to $I_N = 1.3$. Varying $j_n$ at given $G$, $H$, and $\alpha$ in Eq. (5) and at a given vacuum magnetic field, we obtain a series of equilibrium configurations with different $I_N$. The calculations show that, for the main equilibrium, the difference $\beta_N^{\text{wall}} - \beta_N^{\text{no wall}}$ starts to increase with increasing $I_N$ in the range $I_N > 1.3$ (see Fig. 6). In other words, in this range of $I_N$, the stabilizing influence of the wall becomes stronger. This can be explained by the fact that the mode structure changes with changing $I_N$; i.e., the mode becomes more extended in the external region (which is illustrated in Fig. 7) and, therefore, reacts more strongly to the wall. Let us note that the zone between the two discussed MHD limits widens due to the two effects: the increase in $\beta_N^{\text{wall}}$ and the reduction in $\beta_N^{\text{no wall}}$. Operating in this parameter range would be very interesting from the standpoint of verifying the MHD theory predictions in T-15M experiments.

MHD limits depend substantially on the plasma pressure profile. As the pressure peakedness increases,
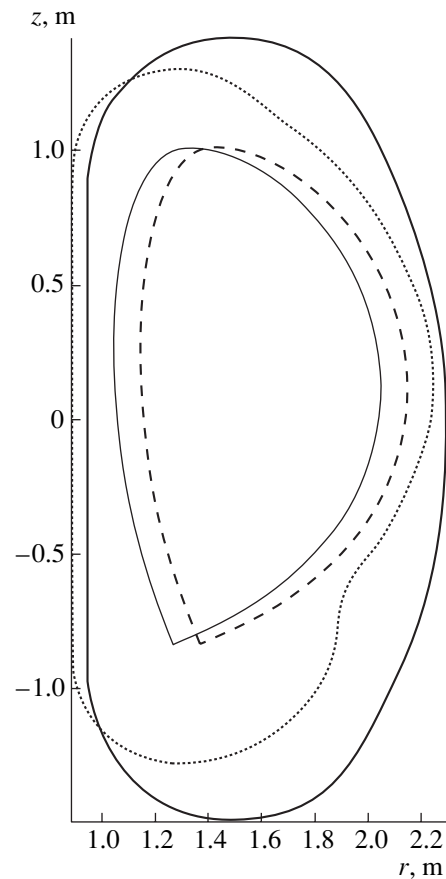
the value of $\beta_N^{\text{wall}}$ becomes smaller and, at $I_N > 1$, the $\beta_N^{\text{no wall}}$ limit also goes down, as is shown in Fig. 6 by squares for a configuration with $p_0/\bar{p} = 3.1$. Then, for the considered equilibrium T-15M tokamak configurations, the gap between these limits appreciably decreases.

In Fig. 8, results for the first equilibrium ($p_0/\bar{p} = 2.55$) identical to those in Fig. 6 are shown as dependences of the $\beta_N$ limits on the value of $1/q_{\min}$ (the maximum rotational transformation) in the plasma. The quantity $1/q_{\min}$ is plotted as an abscissa in Fig. 8 to facilitate the comparison of the results for series of equilibrium configurations with different plasma boundaries (corresponding to different shifts of the boundary along the $R$ axis), since the local minima of the $\beta_N$ limit are associated with the approaching of $q_{\min}$ to resonant surfaces. At the same plasma boundary and fixed $G$ and $H$, the $q_{\min}$ value is, with good accuracy, inversely proportional to the normalized current $I_N$. In particular, $q_{\min}I_N \approx 2.5$ for the initial plasma boundary. For defi-

niteness, the correspondence between the normalized current $I_N$ (which is prescribed in our calculations) and the $q_{min}$ value is specified for equilibrium configurations with $\alpha = 1$ in Eq. (5).

For the sake of comparison, in Fig. 8 we also display the results of calculations of $\beta_N^{wall}$ for the same plasma configuration, but with an ITER-like wall shown by the dotted line in Fig. 9. One can see that the $\beta_N^{wall}$ limit in T-15M is noticeably lower than the same limit in ITER. In this sense, T-15M lags substantially behind the ITER.

Figure 8 is a quantitative illustration of the above statement that the wall in T-15M is far from the plasma. It is also shown there what would happen if the wall were closer to the plasma. The dashed lines show the calculated $\beta_N^{wall}$ limit in T-15M, but with a plasma shifted by 10 cm toward the wall along either one or two axes simultaneously. The effect of such a shift is rather strong: the difference $\beta^{wall} - \beta^{no\,wall}$ is almost twice as large as that calculated for the initial configuration and is closer to the ITER values. The position of the plasma with respect to the wall for the shifted configuration is shown by the dashed curve in Fig. 9.

The $\beta_N^{no\,wall}$ value can be called the RWM limit because it manifests itself as a stability limit for the RWMs, whose growth rate is on the order of $1/\tau_w$ [34, 36–41]. This limit can be exceeded and $\beta$ can be increased to $\beta_N^{wall}$ either in short pulses or at completely stabilized RWMs. Physically, this stabilization reduces to compensating for the resistive losses in the wall and the maintenance of the currents induced in the wall by the plasma-produced perturbation, at the level at which they would be for an ideal wall.

An analysis of the RWM stabilization requires a detailed description of the stabilizing system and possible algorithms of its operation. This brings to the problem a distinctly applied aspect with strict engineering restrictions. For T-15M, they are not yet formulated, therefore the question of the possibility of stabilizing RWMs in T-15M still remains open. The results shown in Fig. 6 prove that RWM stabilization in T-15M could be useful for extending the operational $\beta$ limits, especially at $I_N > 1.3$.

## 4. CONCLUSIONS

The results of the calculations presented in Fig. 6 show that $\beta_N = 3.2$ can be regarded as the stability limit of the ideal kink modes for the steady-state operation of T-15M. This value is obtained for an equilibrium configuration with $p_0/\bar{p} = 2.55$ and parameters corresponding to the ITER scenario 4A [21]. Figure 6 also shows that even a small increase in the pressure peaking factor can result in a substantial reduction of this limit:

$\beta_N^{wall} < 2.6$ at $p_0/\bar{p} = 3.1$. Earlier, the same strong dependence of the $\beta$ stability limit on the plasma pressure peaking factor was found in calculations for ITER [21].

The $\beta_N = 3.2$ limit for a scenario with $p_0/\bar{p} = 2.55$ is obtained with account taken of the stabilizing influence of the first wall (vacuum vessel) in T-15M. Without wall stabilization, the limit drops to $\beta_N = 2.6$–2.7. These are rather low values. If one of the main objectives of the T-15M experimental program will be, as is presumed in the technical project [18], to study the possibility of operating at high $\beta_N$, it is necessary to take special measures in order to increase the $\beta$ limit in T-15M above the calculated $\beta_N^{no\,wall}$ value.

The most simple means could be the equipment of T-15M by a system of active stabilization of kink modes. A similar system, known as a system for RWM stabilization, is already in successful operation in the DIII-D tokamak [34, 36–41].

Generally speaking, RWM stabilization in T-15M could allow steady-state operation in the entire area (in an ideal case) or in a part of the area between the curves passing through the calculated points (circles) in Fig. 6. It would yield a gain in $\beta$. However, even in this case, the upper limit on $\beta$ in T-15M would be low. This is clearly seen when comparing T-15M with ITER in Fig. 8. Let us also recall the JT-60SC project, in which steady-state operation with $\beta_N = 3.5$–5.5 [17] is considered, whereas in T-15M (even in the best case), RWM stabilization would allow one to increase the limit to not higher than $\beta_N^{wall}$, i.e., only to $\beta_N = 3.2$ at $p_0/\bar{p} = 2.55$.

It is also expedient to compare the calculated ideal limits with the $\beta_N$ values already achieved in tokamaks. Let us mention two examples of successful operation at $\beta_N$ above the calculated $\beta_N^{no\,wall}$ limit for T-15M. In JT-60U, plasma with $\beta_N > 2.7$ was sustained for more than seven seconds [42]. In the ASDEX Upgrade tokamak, steady-state operation was demonstrated with $\beta_N > 3$ (up to $\beta_N = 3.5$) [43].

A relatively low $\beta$ limit in T-15M is a consequence of a too large distance between the plasma and the first wall and, accordingly, the weak stabilizing effect of the wall. The dashed curves in Fig. 8 show how strong an effect would result from the reduction of this distance. Placing the wall closer to the plasma in T-15M should be considered inevitable if the objective of T-15M is to operate with $\beta_N$ above the upper limit shown in Fig. 6.

RWM stabilization in the T-15M tokamak and the possibility of operating at $\beta_N > \beta_N^{no\,wall}$ will be investigated in a separate paper. However, the problem of positioning the first wall closer to the plasma goes beyond the scope of formal theory.

## REFERENCES

1. ITER Physics Basis, Nucl. Fusion **39**, 2137 (1999).
2. K. Nishimura, K. Matsuoka, M. Fujiwara, *et al.*, Fusion Technol. **17**, 86 (1990).
3. C. Alejaldre, J. Javier, A. Gozalo, *et al.*, Fusion Technol. **17**, 131 (1990).
4. A. Iiyoshi, M. Fujiwara, O. Motojima, *et al.*, Fusion Technology **17**, 169 (1990).
5. C. Beidler, G. Grieger, F. Herrnegger, *et al.*, Fusion Technol. **17**, 148 (1990).
6. G. Grieger, W. Lotz, P. Merkel, *et al.*, Phys. Fluids B **4**, 2081 (1992).
7. S. C. Jardin, A. Bhattacharjee, A. Bondeson, *et al.*, in *Proceedings of the 14th International Conference on Plasma Physics and Controlled Nuclear Fusion Research, Würzburg, 1992* (IAEA, Vienna, 1993), Vol. 2, p. 285.
8. S. Gori, C. Nührenberg, J. Nührenberg, and R. Zille, J. Plasma Fusion Res. **1**, 62 (1998).
9. P. R. Garabedian, J. Plasma Fusion Res. **1**, 148 (1998).
10. S. M. Kaye, M. Ono, Y.-K. M. Peng, *et al.*, Fusion Technol. **36**, 16 (1999).
11. G. S. Lee and the KSTAR Team, in *Proceedings of the 18th IAEA Fusion Energy Conference, Sorrento, 2000*, Paper IAEA-CN-77/OV7/1.
12. M. Wakatani, Y. Nakamura, K. Kondo, *et al.*, Nucl. Fusion **40**, 569 (2000).
13. S. Okamura, S. Murakami, S. Shimizu, *et al.*, J. Plasma Fusion Res. **3**, 73 (2000).
14. S. Okamura, K. Matsuoka, S. Nishimura, *et al.*, Nucl. Fusion **41**, 1865 (2001).
15. M. C. Zarnstorff, L. A. Berry, A. Brooks, *et al.*, Plasma Phys. Controlled Fusion **43**, A237 (2001).
16. F. Paoletti, S. A. Sabbagh, J. Manickam, *et al.*, Nucl. Fusion **42**, 418 (2002).
17. S. Ishida, K. Abe, A. Ando, *et al.*, in *Proceedings of the 19th IAEA Fusion Energy Conference, Lyon, 2002*, Paper IAEA-CN-94/FT/2-5.
18. *Technical Project of the T-15M Device* (Efremov Institute of Electrophysical Apparatus, St.-Petersburg, 2002).
19. A. D. Turnbull, D. P. Brennan, M. S. Chu, *et al.*, Nucl. Fusion **42**, 917 (2002).
20. Y. Shimomura, Y. Murakami, A. R. Polevoi, *et al.*, Plasma Phys. Controlled Fusion **43**, A385 (2001).
21. A. R. Polevoi, S. Yu. Medvedev, V. D. Pustovitov, *et al.*, in *Proceedings of the 19th IAEA Fusion Energy Conference, Lyon, 2002*, Paper IAEA-CN-94/CT/P-08.
22. L. E. Zakharov and V. D. Shafranov, in *Reviews of Plasma Physics*, Ed. by M. A. Leontovich and B. B. Kadomtsev (Énergoizdat, Moscow, 1982; Consultants Bureau, New York, 1986), Vol. 11.
23. S. P. Hirshman, Phys. Fluids **31**, 3150 (1988).
24. G. V. Pereverzev, P. N. Yushmanov, A. Yu. Dnestrovskij, *et al.*, Preprint No. IPP5/42 (Max-Planck-Institut für Plasmaphysik, Garching, 1991).
25. L. Degtyarev, A. Martynov, S. Medvedev, *et al.*, Comput. Phys. Commun. **103**, 10 (1997).
26. A. W. Morris, R. J. Akers, J. W. Connor, *et al.*, Plasma Phys. Controlled Fusion **41**, B191 (1999).
27. D. A. Mossessian, P. B. Snyder, M. Greenwald, *et al.*, Plasma Phys. Controlled Fusion **44**, 423 (2002).
28. J. A. Wesson, Nucl. Fusion **18**, 87 (1978).
29. E. J. Strait, T. S. Taylor, A. D. Turnbull, *et al.*, Phys. Rev. Lett. **74**, 2483 (1995).
30. T. Taylor, E. J. Strait, L. L. Lao, *et al.*, Phys. Plasmas **2**, 2390 (1995).
31. T. S. Taylor, H. St. John, A. D. Turnbull, *et al.*, Plasma Phys. Controlled Fusion **36**, B229 (1994).
32. C. Gormezano, Plasma Phys. Controlled Fusion **41**, B367 (1999).
33. T. Fujita, Y. Kamada, S. Ishida, *et al.*, Nucl. Fusion **39**, 1627 (1999).
34. T. C. Luce, M. R. Wade, P. A. Politzer, *et al.*, Nucl. Fusion **41**, 1585 (2001).
35. E. N. Bondarchuk, Yu. N. Dnestrovskij, V. M. Leonov, *et al.*, Plasma Devices Oper. (2003) (in press).
36. A. M. Garofalo, E. J. Strait, J. M. Bialek, *et al.*, Nucl. Fusion **40,** 1491 (2000).
37. A. M. Garofalo, M. S. Chu, E. D. Fredrickson, *et al.*, Nucl. Fusion **41**, 1171 (2001).
38. M. Okabayashi, J. Bialek, M. S. Chance, *et al.*, Phys. Plasmas **8**, 2071 (2001).
39. L. C. Johnson, M. Okabayashi, A. M. Garofalo, *et al.*, in *Proceedings of the 28th EPS Conference on Controlled Fusion and Plasma Physics, Funchal, 2001*; ECA **25A**, 1361 (2001); http://www.cfn.ist.utl.pt/EPS2001/fin/pdf/P4.008.pdf.
40. M. Okabayashi, J. Bialek, M. S. Chance, *et al.*, Plasma Phys. Controlled Fusion **44**, B339 (2002).
41. E. J. Strait, J. Bialek, N. Bogatu, *et al.*, in *Proceedings of the 19th IAEA Fusion Energy Conference, Lyon, 2002*, Paper IAEA-CN-94/EX/S2-1.
42. T. Fukuda and JT-60 Team, Plasma Phys. Controlled Fusion **44**, B39 (2002).
43. A. C. C. Sips, R. Arslanbekov, C. Atanasiu, *et al.*, Plasma Phys. Controlled Fusion **44**, B69 (2002).

*Translated by V.D. Pustovitov*

# Second Harmonic of Gyrotron Radiation: New Potentialities of Plasma Diagnostics

**G. M. Batanov\*, L. V. Kolik\*, M. I. Petelin\*\*, A. E. Petrov\*, A. A. Pshenichnikov\*,
K. A. Sarksyan\*, N. N. Skvortsova\*, and N. K. Kharchev\***

*\*Prokhorov Institute of General Physics, Russian Academy of Sciences, ul. Vavilova 38, Moscow, 119991 Russia*
*\*\*Institute of Applied Physics, Russian Academy of Sciences, ul. Ulyanova 46, Nizhni Novgorod, 603600 Russia*
Received March 20, 2003

**Abstract**—It is shown that the relative intensity of the second harmonic of gyrotron radiation on the axis of a microwave beam after quasi-optical filtering in a four-mirror quasi-optical transmission line is about –50 dB of the total radiation intensity. The second-harmonic radiation is used in collective-scattering diagnostics of turbulent density fluctuations in the plasma column of the L-2M stellarator. At an electron temperature of 0.8–1.0 keV and average plasma density of $2.0$–$2.5 \times 10^{13}$ cm$^{-3}$ (a plasma energy of about 0.6 kJ), which was achieved after the boronization of the vacuum chamber, spatiotemporal structures in plasma density fluctuations were observed in the central region of the plasma column. The correlation time between the structures was found to be on the order of 1 ms. It is shown that the spectrum of the signal from the second-harmonic scattering extends to higher frequencies compared to that from the fundamental-harmonic scattering. © 2003 MAIK "Nauka/Interperiodica".

1. Millimeter and submillimeter microwaves are widely used in plasma diagnostics. The oscillator power in this wavelength range is usually around several dozen milliwatts and rarely attains that of a few watts. This requires very high sensitivity and noise immunity of the receiving facility, especially when radiation scattering by plasma density fluctuations is used to diagnose plasma oscillations. On the other hand, microwave oscillators with powers of several hundred kilowatts are used in most experiments on plasma production and heating in magnetic confinement systems. Due to nonlinear effects, the output radiation of these oscillators contains harmonics of the fundamental frequency. The power of these harmonics, even though they are –40 to −50 dB of the output power, substantially exceeds the power of the conventional oscillators used in plasma diagnostics. Our experiments on electron-cyclotron resonance (ECR) plasma heating and microwave discharges in gases have shown that the second-harmonic component with a fairly high power is certainly present in the gyrotron radiation.

This is why, in the L-2M experiments, we decided to measure the intensity of the second harmonic of gyrotron radiation after quasi-optical filtering at the exit from a four-mirror quasi-optical transmission line, and to study plasma density fluctuations in the central region of the plasma column by using collective scattering of the second-harmonic radiation.

2. The parameters of the L-2M stellarator and its gyrotron complex were described in our previous papers (see, e.g., [1, 2]). The plasma was produced and heated by microwave radiation at the second harmonic

of the electron gyrofrequency. The magnetic field at the axis of the vacuum chamber was 1.35 T.

In our experiments, we used two GYCOM gyrotrons of the Brider-1 type with an operating frequency of 75.3 GHz and a pulse duration of 1–12 ms.

The signals at the second harmonic of the gyrotron frequency (at 150 GHz) were measured with the help of a collimator that was a cylinder made of an absorbent rubber placed in a plexiglass shell. The cones of the absorbent rubber protruded into the cylinder interior so as to form a corrugated waveguide with absorbent walls. A waveguide transition from the $7.2 \times 3.4$- to $1.6 \times 0.8$-mm section was attached to the bottom of the plexiglass shell at its axis. The waveguide transition was connected to a $1.6 \times 0.8$-mm rectangular waveguide section (or two sections placed one after another), which ended with a detector unit sensitive to the 150-GHz radiation.

Thus, the gyrotron radiation at a frequency of 75 GHz was attenuated by a below-cutoff waveguide of length 25 or 50 mm. The absorbent rubber cylinder served as a beam collimator. All the waveguide junctions and the detector unit were shielded by the absorbent rubber. The entire assembly was placed inside an absorbent rubber cylinder.

The gyrotron second harmonic was separated out with the help of a filter made of two plane-parallel mica plates placed between the last mirror of the quasi-optical transmission line and the window of the stellarator vacuum chamber. The filter plates were oriented at an angle of $\pi/4$ to the beam axis. The filter was tuned so that it was almost transparent (the transmission coeffi-
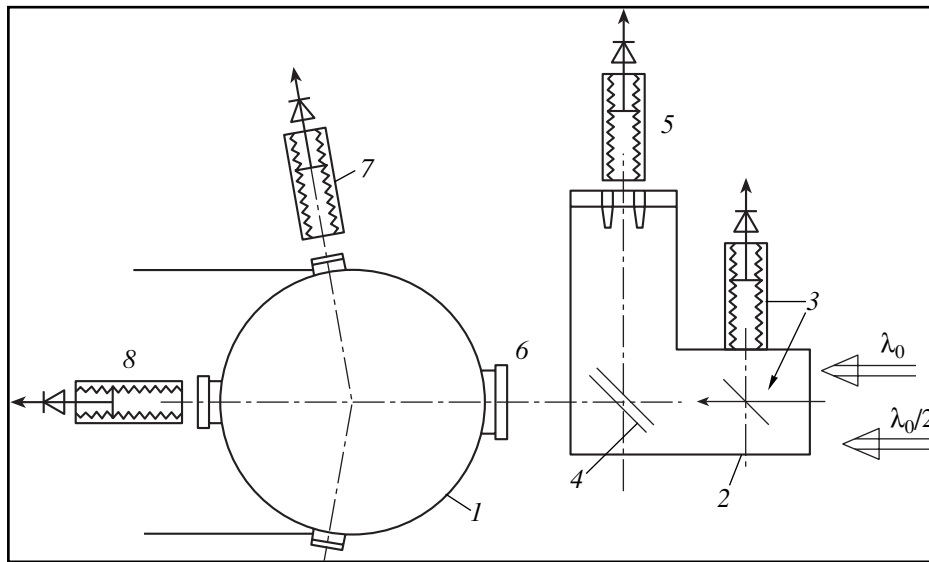
**Fig. 1.** Experimental arrangement: (*1*) vacuum chamber of L-2M, (*2*) quasi-optical detector unit, (*3*) quasi-optical coupler with a detector unit for monitoring the gyrotron incident power, (*4*) quasi-optical filter, (*5*) detector unit for measuring the second-harmonic power, (*6*) stellarator input window, (*7*) detector unit for measuring the scattered signal at the fundamental or second harmonic, and (*8*) detector unit for measuring the passed fundamental-harmonic power.

cient was no less than 0.9) at a wavelength of 4 mm (the fundamental harmonic) and, at the same time, reflected up to 80% of radiation at a wavelength of 2 mm (the second harmonic). After leaving the quasi-optical transmission line, the second-harmonic beam was deflected by the filter placed at an angle of $\pi/2$ toward the detector unit positioned at a distance of 67 cm from the center of the filter, i.e., at the same distance as the inner wall of the stellarator vacuum chamber. The detector unit was calibrated in a microwave beam from a standard-signal generator, whose output power was measured with the help of a calorimeter. The experimental arrangement is shown in Fig. 1. Figure 2 shows examples of the detected signals. The signal at the fundamental harmonic of the gyrotron radiation, having passed through the filter, was measured by a detector installed behind the inner port of the stellarator. Measurements showed that, within the measurement error (~10%) of the microwave pulse amplitude, there was no difference between the signals in the presence and in the absence of the resonance filter. Hence, we can conclude that no more than 10% of the fundamental-harmonic power was directed by the filter into the detector unit measuring the second-harmonic radiation.

The second-harmonic signal was at maximum when the filter was tuned to the resonance frequency. If the filter was out of the resonance, the signal was almost one order of magnitude lower. The maximum second-harmonic power measured by the detector unit was about 10 mW, which corresponded to an intensity of 40 W/cm² at the beam axis. On the other hand, the calculated intensity of the gyrotron beam at the same distance from the focal plane is about $4 \times 10^3$ W/cm². Hence, the second-harmonic intensity in the gyrotron

beam after filtration in the quasi-optical transmission line is $10^{-5}$ of the fundamental-harmonic intensity. To determine the total second-harmonic power, it is necessary to know the field distribution across the beam. Unfortunately, we could not perform such measurements. To estimate this power, we calculated the parameters of the second-harmonic radiation after the focusing by the mirrors of the quasi-optical transmission line, assuming the beam to be Gaussian at the gyrotron output window. In calculations, the characteristic radius of the Gaussian beam was varied from 5 to 40 mm. The calculations showed that the second-harmonic beam should have a smaller divergence as compared to the fundamental-harmonic beam, and its radius at the focal plane should also be smaller. Based on the calculated beam radius, we can conclude that the total second-harmonic power is no less than 0.3 W. Such a power at the input window of the stellarator is sufficient for the diagnostics of plasma density fluctuations and exceeds the output power of the conventional oscillators used in plasma diagnostics. We also measured the degree of polarization of the second-harmonic radiation. For this purpose, we measured the signals at two orientations of the receiving waveguide: its wide wall was oriented perpendicular or parallel to the plane of incidence of the gyrotron radiation onto the mica plates of the filter. The measurements showed that the polarization was the same for the second and fundamental harmonics: the electric field vector lay in the plane of incidence, the ratio of the signals measured at two mutually orthogonal orientations being no less than 10 dB.

We measured the dependence of the second-harmonic intensity on the gyrotron power at different cath-
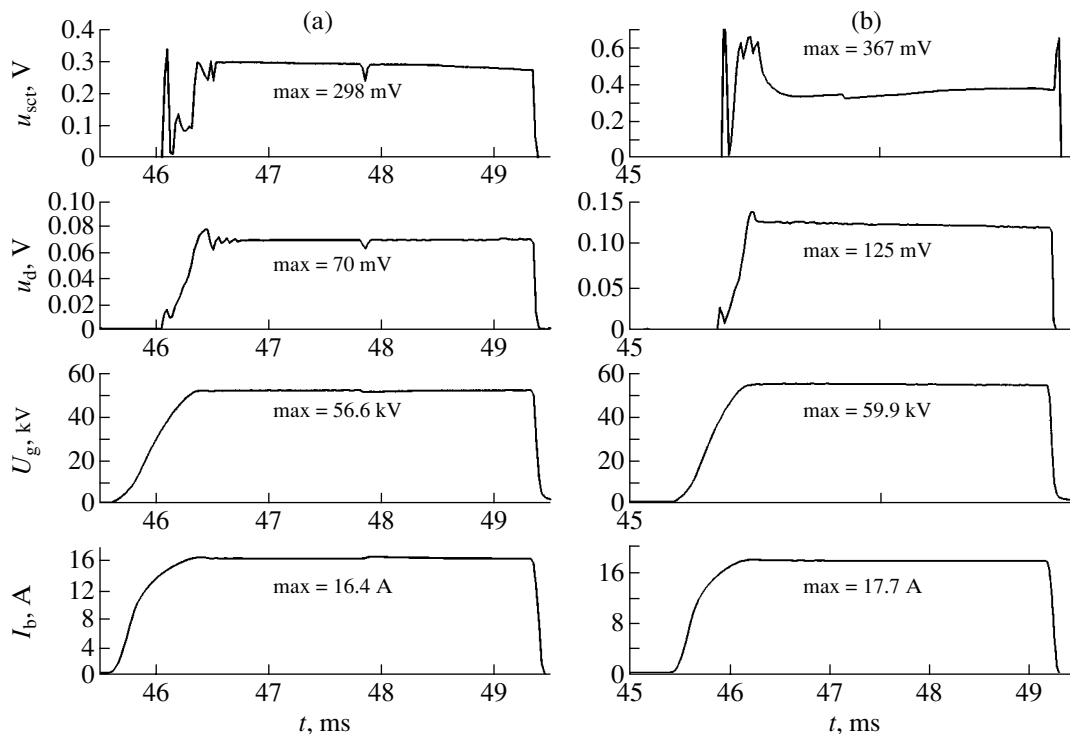
**Fig. 2.** Examples of signals recorded in studying the second harmonic of the gyrotron radiation at a gyrotron output power of (a) 89 and (b) 150 kW. From top to bottom: the second-harmonic signal reflected from the quasi-optical filter, the incident-radiation signal, gyrotron voltage, and gyrotron-beam current.

ode voltages and beam currents. It turned out that, as the gyrotron output power varied from 84 to 155 kW, the amplitude of the second-harmonic signal varied only slightly. The variations in the second-harmonic signal were more pronounced when we varied the beam current: an increase in the current by 10% at $\pm 1\%$ variations in the cathode voltage resulted in a tenfold increase in the signal amplitude. A four- to fivefold increase in the second-harmonic signal was observed when the cathode voltage was decreased by 2.5%, while the current was decreased only slightly (by 0.6%) and the fundamental-harmonic power also changed insignificantly.

In a gyrotron, as in any self-oscillator, the active medium (in our case, a nonequilibrium electron beam) is nonlinear. This is the main cause of the saturation of the medium conductivity, which results in steady self-oscillations. Along with this, the action of an alternating electromagnetic field on the nonlinear active medium produces the current harmonics (which are multiples of the fundamental frequency), which, in turn, produce the harmonics of the output radiation.

Specifically, in a gyrotron, the current harmonics are generated due to the orbital bunching of electrons due to relativistic effects. Note that the relativistic dependence of the gyrofrequency of electrons on their energy leads to the anomalous (in comparison with a traveling-wave tube, klystron, and other conventional devices)

effect of a negative mass, resulting in a Coulomb attraction between electrons, which favors bunching [3].

The larger the excess of the electron current over the start value, the higher the amplitude of the self-oscillations and the higher the intensity of harmonics in the electron current spectrum. In a steady-state operating mode with a high gyrotron efficiency, the second and third harmonics of the electron current can be comparable in amplitude with the fundamental harmonic. Nevertheless, the fundamental mode is dominant in the spectrum of the generated electromagnetic field because it is excited in a resonant fashion. Except for certain special cases,[1] the second harmonic of the current excites only travelling waves in the gyrotron electrodynamic system. The coupling between the second harmonic and these waves is a factor of $\sim 1/Q$ lesser than that of the gyrotron fundamental mode (here, $Q$ is the quality factor of the fundamental mode, which is usually on the order of $10^3$).

Another important factor is that modern high-power gyrotrons include a built-in mirror converter that transforms the generated mode into a Gaussian beam,

---

[1] The efficiency of an $n$-fold frequency multiplication can be higher when the $n$th harmonic of the electron current is in resonance with a gyrotron cavity eigenmode, providing that the latter possesses an adequate symmetry. Such a situation can occur, e.g., in a quasi-axisymmetric gyrotron if the secondary mode has an azimuthal index that is $n$ times the azimuthal index of the primary mode excited at the fundamental cyclotron resonance [3].
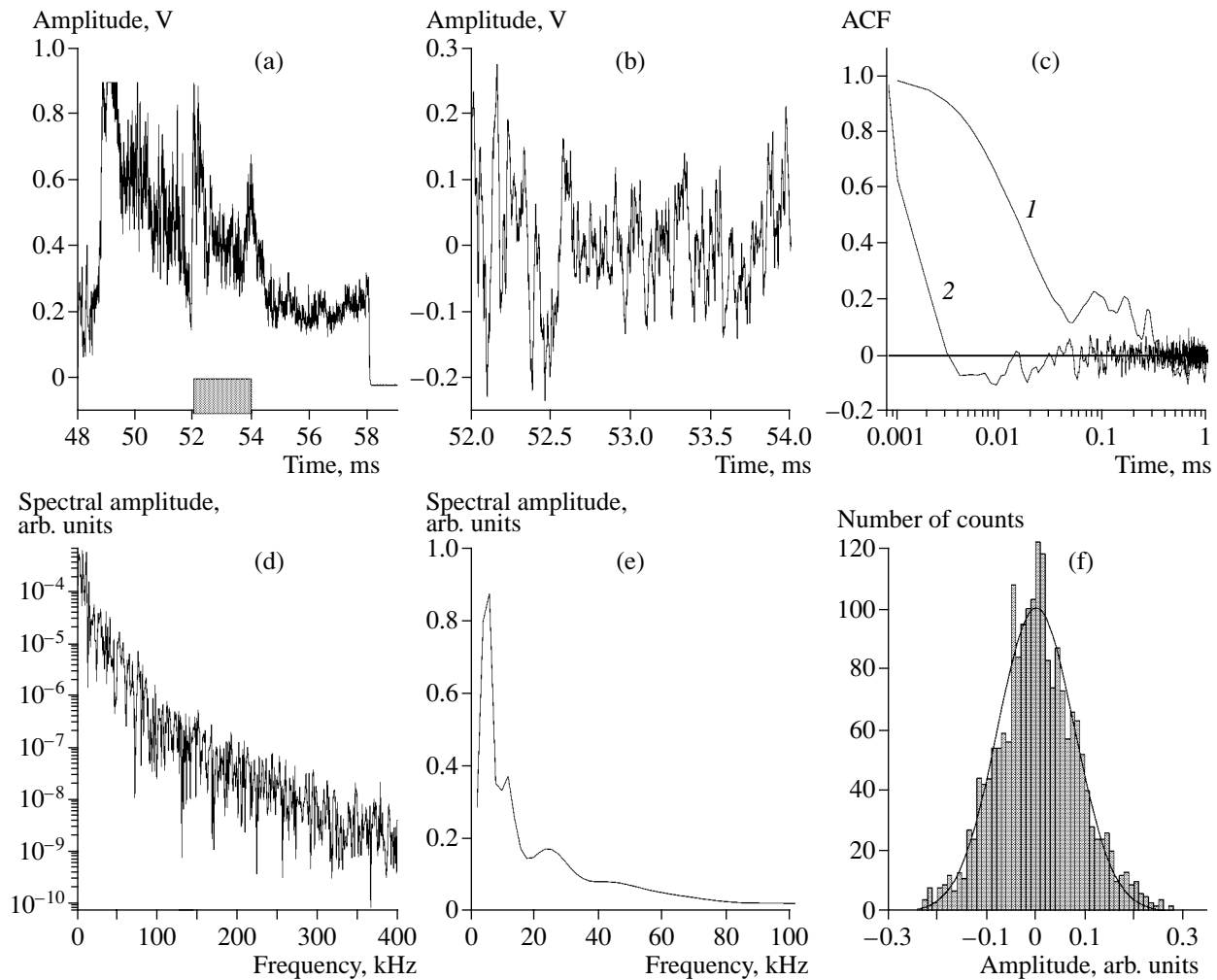
**Fig. 3.** (a) Signal from the second-harmonic ($\lambda$ = 2 mm) scattering in shot no. 54 215 and the results of processing the detector signal over the time interval 52–54 ms: (b) detector signal after the HF filter, (c) ACFs of the (*1*) detector signal and (*2*) signal increments, (d) Fourier spectrum, (e) wavelet spectrum, and (f) PDF of the amplitudes of the scattered signal. The solid line corresponds to a Gaussian distribution.

which, in turn, feeds an external overmoded filtering waveguide (e.g., a mirror line) transmitting the microwave power to the load. For modes other than fundamental, the power-transfer coefficient from the output of the gyrotron cavity to the output of the transmission line can be estimated at $10^{-2}$–$10^{-4}$. It can then be expected that, at the output of the system, the second-harmonic power will be $10^{-5}$–$10^{-7}$ of the fundamental-harmonic power.

3. The second-harmonic beam, as well as the main gyrotron beam, was used to study the collective scattering of radiation by plasma density fluctuations in the heating region of the L-2M stellarator. By the main beam, we mean the beam at the fundamental frequency ($\omega_0$), which was used for the ECR heating of the plasma at the second harmonic of the electron gyrofrequency ($2\Omega_e$). The results of collective-scattering measurements at two probing frequencies were then compared with each other.

As was mentioned above, the parameters of the L-2M stellarator are described in [1, 2]. The plasma column was heated with two Brider-1 gyrotrons, operating at a frequency of 75.3 GHz. The distance between the heating regions of these gyrotrons along the stellarator axis was 1/14 of the axis length ($\approx$6 m). The experiments were conducted after the boronization of the vacuum chamber, which resulted in the reduction of the radiation power to 40–55 kW at a total heating microwave power of 250–350 kW. The line-averaged electron density, which was measured by a microwave interferometer, amounted to $2.0$–$2.5 \times 10^{13}$ cm$^{-3}$. The central electron temperature, measured from the soft X-ray spectra and from the spectra of thermal microwave plasma emission at the second harmonic of the electron gyrofrequency (76 GHz), was 0.8–1.0 keV. The plasma energy, measured from the plasma diamagnetism, was about 0.5–0.6 kJ. The experimental arrangement for the scattering diagnostics is shown in
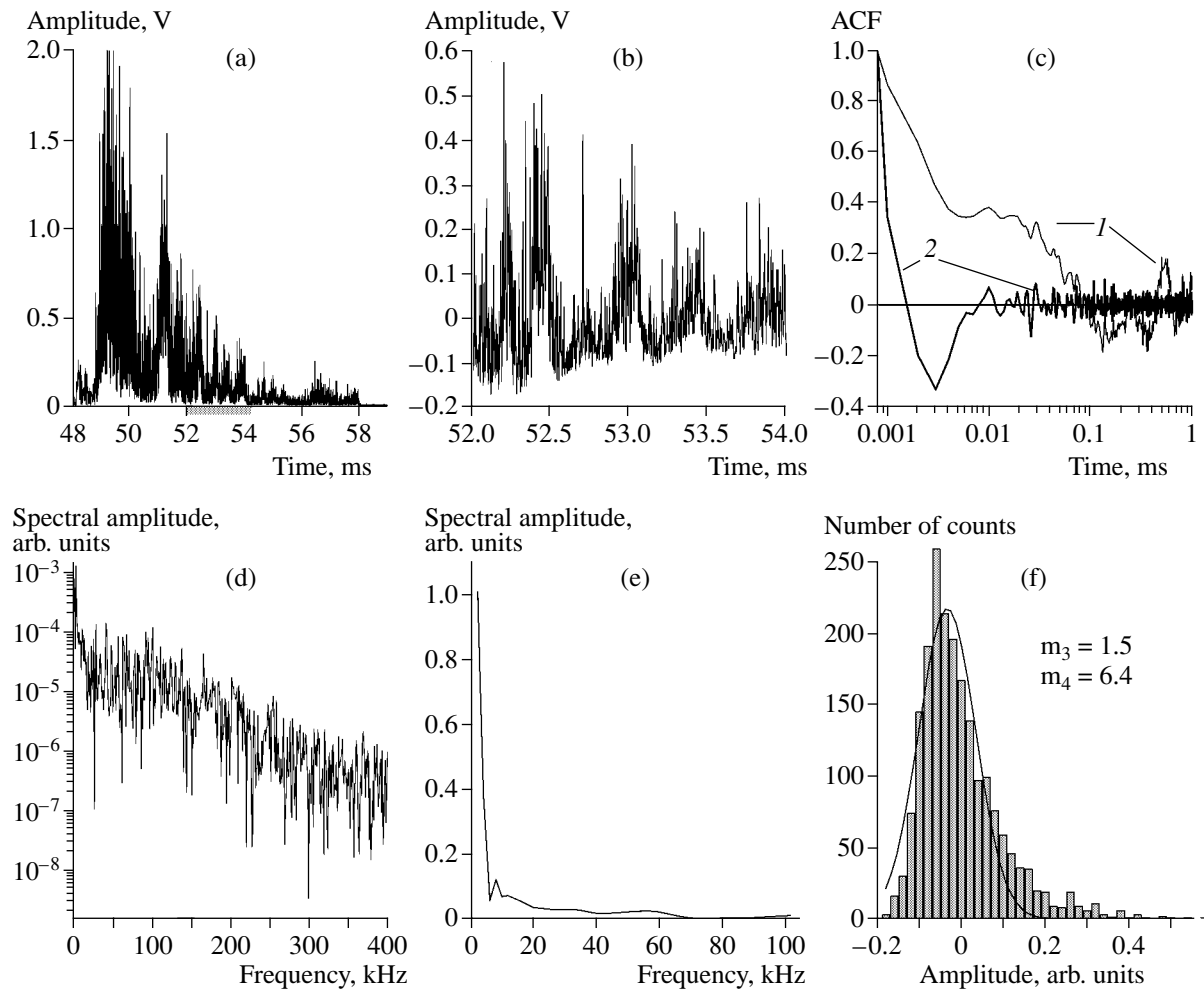
**Fig. 4.** (a) Signal from the fundamental-harmonic ($\lambda = 4$ mm) scattering in shot no. 54482 and the results of processing the detector signal over the time interval 52–54 ms: (b) detector signal after the HF filter, (c) ACFs of the (*1*) detector signal and (*2*) signal increments, (d) Fourier spectrum, (e) wavelet spectrum, and (f) PDF of the amplitudes of the scattered signal. The solid line corresponds to a Gaussian distribution.

Fig. 1. It can be seen from Fig. 1 that the radiation scattered by plasma density fluctuations is measured at an angle of nearly $\pi/2$ to the axis of the probing beam. As detectors, we used a detector unit identical to that for measuring the gyrotron radiation. The collimator of the detector unit allowed the reception of the scattered signals within the angle $\Delta\theta = \pm 0.1$ rad. Direct detection of the scattered signals was used for probing at both the fundamental and second harmonics of the gyrotron radiation. The amplitude of the scattered signal at the fundamental harmonic was chosen such that the detector operated in the linear range of its characteristic, so that we had $U_\omega \propto P_{\text{sct}}$. The amplitude of the second-harmonic signal was about 1 mV. At such small amplitudes, we had $U_{2\omega} \propto P_{\text{sct}}^3$. The measuring circuit for the second-harmonic signal included an amplifier with a gain factor of $10^2$. The scattered signals were digitized with a sampling rate of 1 MHz.

When measuring the second-harmonic scattering, we detected only radiation with the electric field vector lying in a plane orthogonal to the axis of the vacuum chamber (the wide wall of the receiving waveguide was parallel to the axis of the vacuum chamber).

The signal from stray radiation produced by multiple scattering by the vacuum chamber wall and falling into the detector unit was at a level of 0.016 of the second-harmonic signal. Such a value of the stray signal is quite acceptable in measurements of the collective scattering by plasma fluctuations. The stray signal was observed at the leading edge of the scattered signal for 1.0–1.5 ms, which corresponds to the time interval during which the electron density in the plasma column rapidly grows. It can be seen from Fig. 3a that the amplitude of the scattered signal is several times the amplitude of the stray signal. This means that the power of the scattered signal is comparable to the power of the stray signal. The stray signal can be regarded as a reference signal in the homodyne detector circuit. The inter-
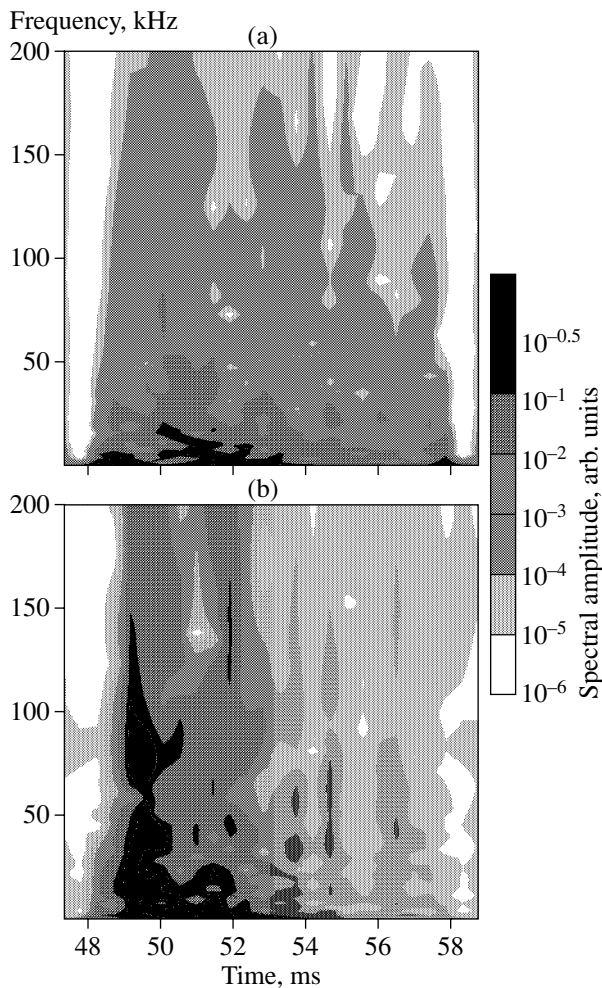
Frequency, kHz



**Fig. 5.** Temporal wavelet spectra of the detector signals from the scattering at the (a) second (shot no. 54215) and (b) fundamental harmonic (shot no. 54482) of the gyrotron radiation.

ferometric data show that the electron density varies only slightly during the discharge, so that the phase of the reference signal can be assumed constant when measuring oscillations with frequencies above 3 kHz. Higher frequency fluctuations of the reference-radiation power that are caused by the effect of small-angle scattering are estimated to be about 0.01 of the power of the reference signal.

A similar situation occurred when we measured the scattering of the fundamental-harmonic radiation (Fig. 4a). In this case, we only detected the scattered radiation with the electric field vector parallel to the axis of the vacuum chamber (the wide wall of the receiving waveguide was perpendicular to the chamber axis), which corresponded to the scattering of the ordinary wave that arose due to the splitting of the linearly polarized gyrotron radiation in the plasma of the L-2M stellarator [4, 5].

It can be seen from Figs. 3a and 4a that the scattered signals of both harmonics show a similar behavior. The level of stray radiation can be judged from the time delay before breakdown. In the early stage of the discharge (1.0–1.5 ms), when the plasma density grows, we observe a sharp peak in the scattered radiation intensity. Then, as the electron temperature increases, the amplitude of the scattered signal decreases. A comparison of the scattered signals for different average densities shows that the amplitude of the scattered signal increases with increasing plasma density.

4. The results of the spectral and statistical analysis of the scattered signals are shown in Figs. 3 and 4.[2] The Fourier and wavelet spectra were computed with the use of a 2-kHz filter. Figures 3d, 3e, 4d, and 4e show such spectra averaged over a time interval of 2 ms (from 52 to 54 ms in a real time of the stellarator shot, as is indicated by a shaded rectangular in Figs. 3a and 4a). For the probing at both the fundamental and second-harmonic frequencies, the spectral density of the scattered signal falls by a factor of 10–100 at frequencies of 100–150 kHz. At the same time, for the second-harmonic scattering, the signal spectrum extends to higher frequencies compared to the fundamental-harmonic scattering.

The autocorrelation functions (ACFs) for both probing frequencies (Figs. 3c, 4c) demonstrate the presence of long-term correlation, which indicates the existence of spatiotemporal structures in the plasma density fluctuations. The formation and time evolution of such structures is seen in Fig. 5. This figure shows the wavelet spectra of the scattered signals at the (a) second and (b) fundamental harmonics of the gyrotron radiation. The temporal spectra are collected by interpolating 25 successive wavelet spectra constructed on equal time intervals of 0.5 ms. The time variations in the temporal wavelet spectrum can be related to the presence of stochastic plasma structures in the heating region. The presence of long-term correlation in the ACF implies that the density fluctuations cannot be regarded as statistically independent. In this case, the increments of the fluctuation amplitudes can be statistically independent, as is the case with local particle fluxes in probe measurements [7]. However, as can be seen from Figs. 3c and 4c, the magnitude of the ACF of the increments is much greater than the instrumentation noise, which is about 0.02. This clearly demonstrates the presence of long-term correlation in the processes of the growth and decay of plasma fluctuations.

The probability density function (PDF) of the amplitudes of the fluctuation signals in the case of the second-harmonic scattering is close to a Gaussian distribution and is slightly asymmetric (with a skewness of $m_3 = 0.1$), whereas a rather strong asymmetry with a heavy "tail" of large amplitudes (in comparison with a Gaussian distribution) is observed in the case of the
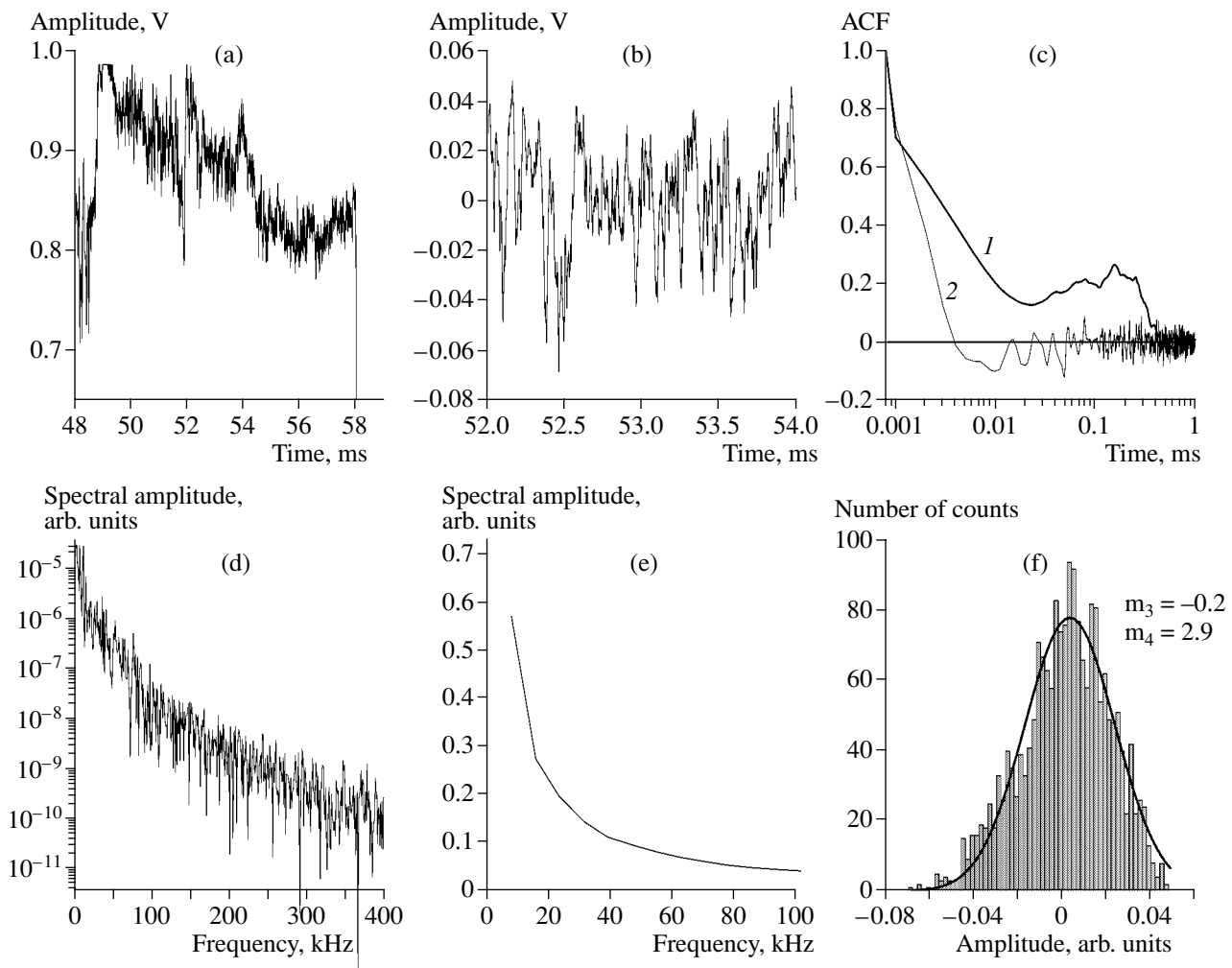
**Fig. 6.** (a) Time behavior of the $A^{1/6}$ signal (where $A$ is the amplitude of the detector signal from the second-harmonic scattering in shot no. 54215) and the results of its processing over the time interval 52–54 ms: (b) $A^{1/6}$ signal after the HF filter, (c) ACFs of the (1) $A^{1/6}$ signal and (2) its increments, (d) Fourier spectrum of the $A^{1/6}$ signal, (e) wavelet spectrum of the $A^{1/6}$ signal, and (f) PDF of the amplitudes of the $A^{1/6}$ signal. The solid line corresponds to a Gaussian distribution.

fundamental-harmonic scattering. This difference may be attributed to the different scales of scattering fluctuations for the second and fundamental harmonics (3 and 6 mm, respectively). On the other hand, we may suppose that the PDF is less sensitive to the spatiotemporal coupling of fluctuations than the ACF.

Up to this point, we have analyzed the signals from the detectors of scattered radiation. However, the amplitude of plasma density fluctuations in the case of second-harmonic scattering is proportional to the sixth root of the signal amplitude, whereas it is proportional to the square root in the case of fundamental-harmonic scattering. In our case, the amplitude resolution was sufficient to perform the corresponding processing of the scattered signals (the amplitude resolution of the detector signals was 1 mV, whereas the fluctuation amplitude was $10^2$–$10^3$ mV). Figures 6 and 7 show the results of such a processing. We can see that all the

characteristic features of the ACFs, Fourier spectra, and PDFs persist in this case too. Therefore, we can conclude that the formation of spatiotemporal structures and the correlation between them are also typical for the density fluctuations of charged particles in the region of ECR plasma heating at the second harmonic of the electron gyrofrequency.

5. The measurements of the second-harmonic radiation intensity of the Brider-1 gyrotron at the output from the quasi-optical line, which is used to transport and focus the gyrotron radiation, have shown the presence of a second-harmonic component with an intensity on the order of $10^{-5}$ of the total radiation intensity. The power of the second-harmonic radiation inside the plasma column has been found to be much higher than the power of microwave beams produced by conventional diagnostic oscillators. It is shown that the sec-
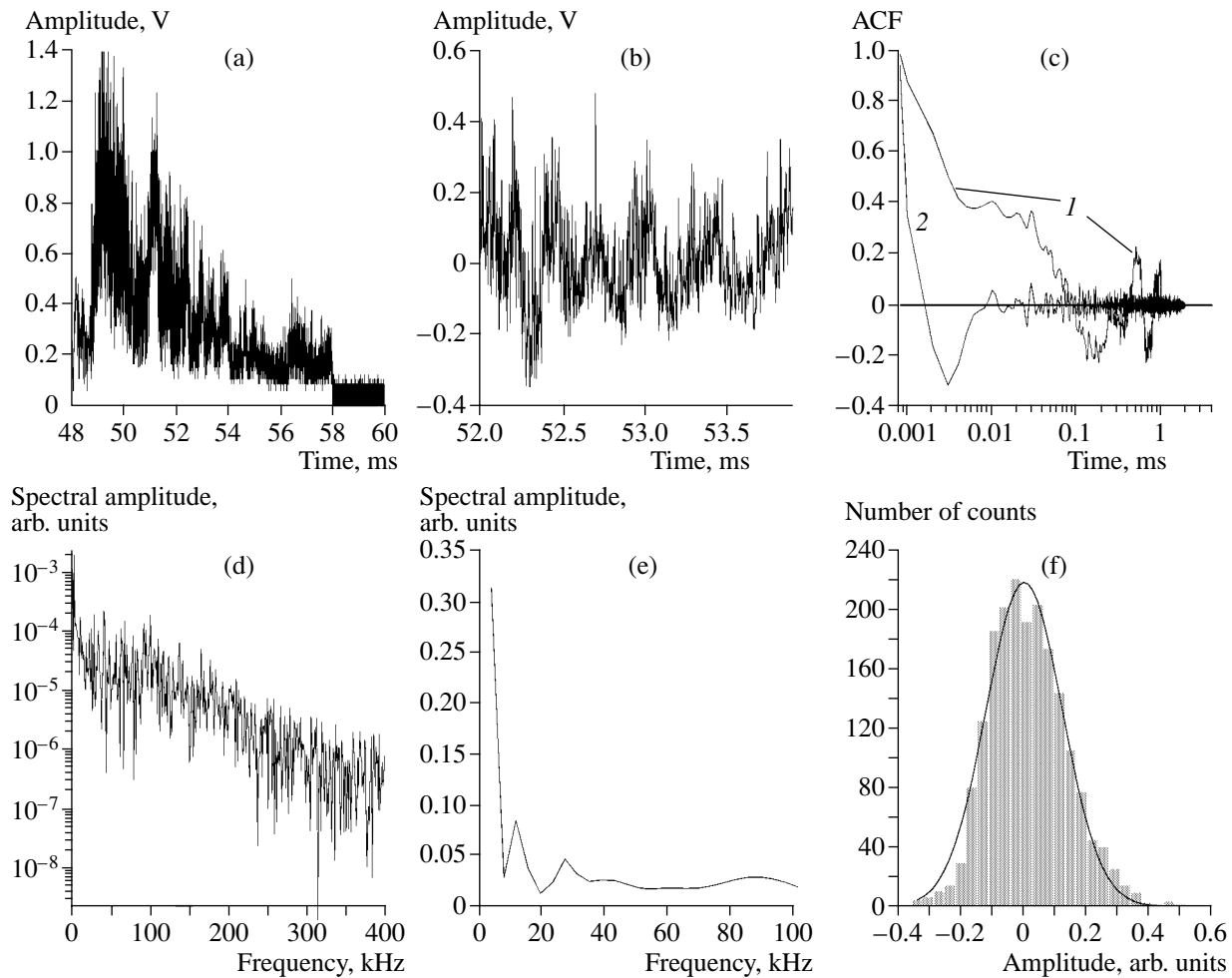
**Fig. 7.** (a) Time behavior of the $A^{1/2}$ signal (where $A$ is the amplitude of the detector signal from the fundamental-harmonic scattering in shot no. 54482) and the results of its processing over the time interval 58–60 ms: (b) $A^{1/2}$ signal after the HF filter, (c) ACFs of the (*1*) $A^{1/2}$ signal and (*2*) its increments, (d) Fourier spectrum of the $A^{1/2}$ signal, (e) wavelet spectrum of the $A^{1/2}$ signal, and (f) PDF of the amplitudes of the $A^{1/2}$ signal. The solid line corresponds to a Gaussian distribution.

ond-harmonic radiation has the same polarization as the fundamental-frequency radiation.

The possibility has been demonstrated of using the second-harmonic radiation for collective-scattering diagnostics of the plasma density fluctuations. It is shown that, in the plasma column of the L-2M stellarator with an electron temperature of 0.8–1.0 keV and average electron density of $2.0$–$2.5 \times 10^{13}$ cm$^{-3}$ (a plasma energy of about 0.6 kJ), which were achieved after the boronization of the vacuum chamber, the fluctuation behavior derived from the measurements of the second-harmonic scattering is consistent with the previous observations. In particular, the formation of spatiotemporal structures and a long-term correlation between them have been observed. The fluctuation spectra corresponding to different spatial scales show different behaviors: the spectrum of the signal from the second-harmonic scattering decays with increasing fre-

quency more slowly than that from the fundamental-harmonic scattering.

Note that the second-harmonic gyrotron radiation can also be used in other plasma diagnostics, e.g., in plasma interferometry.

## ACKNOWLEDGMENTS

## REFERENCES

1. V. V. Abrakov, D. K. Akulina, E. D. Andryuhina, *et al.*, Nucl. Fusion **37**, 233 (1997).
2. S. E. Grebenshcikov, V. V. Abrakov, D. K. Akulina, *et al.*, Plasma Phys. Controlled Nucl. Fusion Res. **2**, 327 (1994).
3. A. V. Gaponov, M. I. Petelin, and V. K. Yulpatov, Izv. Vyssh. Uchebn. Zaved., Radiofiz. **10**, 1414 (1967).
4. E. V. Suvorov and A. A. Fraĭman, Fiz. Plazmy **6**, 1161 (1980) [Sov. J. Plasma Phys. **6**, 639 (1980)].
5. O. B. Smolyakova, E. V. Suvorov, A. A. Fraĭman, and Yu. V. Khol'nov, Fiz. Plazmy **9**, 1194 (1983) [Sov. J. Plasma Phys. **9**, 688 (1983)].
6. B. Ph. Van Milligen, E. Sanchez, T. Estrada, *et al.*, Phys. Plasmas **2**, 3017 (1995).
7. G. M. Batanov, V. E. Bening, V. Yu. Korolev, *et al.*, Pis'ma Zh. Éksp. Teor. Fiz. **73**, 143 (2001) [JETP Lett. **73**, 126 (2001)].

*Translated by N.F. Larionova*

===================== **STELLARATORS** =====================

# Influence of the Plasma Density and Heating Power on the Intensity of Electron Cyclotron Emission in the L-2M Stellarator

**D. K. Akulina, G. M. Batanov, M. S. Berezhetskiǐ, G. S. Voronov, G. A. Gladkov, S. E. Grebenshchikov, I. S. Danilkin, N. F. Larionova, A. I. Meshcheryakov, K. A. Sarksyan, O. I. Fedyanin, N. K. Kharchev, Yu. V. Khol'nov, and S. V. Shchepetov**

*Prokhorov Institute of General Physics, Russian Academy of Sciences, ul. Vavilova 38, Moscow, 119991 Russia*
Received April 17, 2003; in final form, June 3, 2003

**Abstract**—Results are presented from experiments on studying the plasma behavior in the L-2M stellarator in regimes with a high power deposition in electrons during electron cyclotron heating at the second harmonic of the electron gyrofrequency (X mode) at heating powers of $P_{in} = 120$–400 kW and average plasma densities from $n_e \leq 3 \times 10^{19}$ to $0.3 \times 10^{19}$ m$^{-3}$. It is shown that, as the plasma density decreases and the heating power increases, the electron cyclotron emission spectrum is modified; this may be attributed to a deviation of the electron energy distribution from a Maxwellian and the generation of suprathermal electrons. At low plasma densities, the emission intensity at the second harmonic of the electron gyrofrequency increases, whereas the plasma energy measured by diamagnetic diagnostics does not increase. This poses the question of the correctness of determining the plasma electron temperature by electron cyclotron emission diagnostics under these conditions. © *2003 MAIK "Nauka/Interperiodica".*

## 1. INTRODUCTION

In recent years, great attention has been devoted to the plasma behavior in both tokamaks and stellarators during electron cyclotron resonance heating (ECRH) at the fundamental and second harmonics of the electron gyrofrequency. To achieve high energy deposition and high electron temperature, the input microwave power $P_{in}$ generated by gyrotrons is increased or the average plasma density $n_e$ is decreased. An electron temperature as high as 10 keV was achieved in the T-10 tokamak [1] at $n_e = 1.5 \times 10^{19}$ m$^{-3}$ and an absorbed power of $P_{ab} = 2.2$ MW and in the LHD stellarator [2] at $n_e = 0.5 \times 10^{19}$ m$^{-3}$ and an input power of $P_{in} = 1$ MW. In both stellarators and tokamaks, a deviation of the electron energy distribution from a Maxwellian and the generation of suprathermal electrons were observed at a reduced plasma density and increased input power. This phenomenon is described in considerable detail in many papers (see, e.g., [3–13]).

At a reduced plasma density and a specific magnetic field structure (the presence of a local minimum or ripples of the magnetic field), a number of interesting effects have been observed in the power absorption region [14] of stellarators. These effects are related to a peculiar behavior of suprathermal electrons: their trapping in magnetic ripples and their fast escape from the plasma. As a result, a sheared radial electric field is generated and the plasma thermal conductivity changes, which gives rise to an internal transport barrier. In this case, the radial profile of the electron temperature $T_e(r)$ changes and the lifetime of the bulk electrons increases. This effect was described, e.g., in [14–18]. The effect of suprathermal electrons was also studied in the L-2M stellarator [19], which, however, possesses a different configuration of the magnetic field.

The main objective of the experiments described in the present paper was to study the characteristic features in the behavior of the plasma energy and electron cyclotron emission (ECE) in the L-2M stellarator at input powers of $P_{in} = 120$–400 kW and average electron densities within the range $n_e = (3$–$0.3) \times 10^{19}$ m$^{-3}$.

## 2. EXPERIMENTAL CONDITIONS

The L-2M stellarator has two-pole helical windings ($l = 2$) and 28 toroidal-field coils. The number of the helical-field periods is $M = 14$, the major radius of the torus is $R_0 = 1$ m, and the mean plasma radius is $a_p = 0.11$ m. The rotational transform at the axis of the plasma column is $\iota = 0.2$, and its equal to $\iota = 0.8$ at the plasma boundary. The plasma volume in the stellarator is about $2.6 \times 10^5$ cm$^3$.

The plasma cross section is elliptical. In the "standard" section, the ellipse is inclined to the major radius $R_0$ at an angle of $\alpha = 45°$, whereas in the "nonstandard" cross section, it is inclined at an angle of $\alpha = 90°$. The 75-GHz microwave radiation generated by gyrotrons with a total power of up to 400 kW was launched from the low-field side (LFS) in the standard section.

Receiving horns of superheterodyne receivers were placed both on the high-field side (HFS) and LFS of the torus. The ECE receiving system consisted of three double-conversion superheterodyne receivers (10 channels in total). Four channels ($f = 68$–74 GHz) were positioned on the LFS in the standard section. These channels received emission from the plasma regions corresponding to the flux surfaces with the normalized radii $r/a_p = 0.11$ (74 GHz), 0.29 (72 GHz), 0.46 (70 GHz), and 0.67 (68 GHz). The other four channels ($f = 76$–81 GHz) were positioned on the HFS: $r/a_p = -0.15$ (76 GHz), $-0.3$ (78 GHz), $-0.46$ (79.5 GHz), and $-0.6$ (81 GHz). In addition, two channels receiving signals from the HFS were placed in the nonstandard section: $r/a_p = 0.58$ (71 GHz) and 0.63 (77 GHz). To prevent gyrotron radiation from falling into the receiver mixers, we used band-pass and notch filters with a passwidth of $\Delta f = 75.3 \pm 1$ GHz. The intermediate frequency of the receivers was 200 MHz; for the magnetic-field gradient in L-2M, this corresponded to a spatial resolution on the order of 1 cm. The time resolution was limited to ~50 μs by the data acquisition system of L-2M.

The outward (Shafranov) shift of the center of the flux surfaces (the initial coordinate was $R_{\mathrm{ax}}(0) = 0.97$ m) during plasma heating amounted to $\Delta r = 1.8$–3.3 cm; i.e., the magnetic axis came close to the center of the vacuum chamber ($R_0 = 1$ m).

The magnetic system created a field configuration in which the absolute value of the magnetic field $|B|$ varied along the major circumference (see Fig. 1). The focused microwave beam entered the plasma at the slope of a local magnetic well produced by stellarator magnetic traps. The magnetic traps and the associated magnetic wells were located asymmetrically about the section in which the microwave beam was launched. The ripple depth (and, accordingly, the population of the trapped particles) increased toward the plasma boundary. For the magnetic field structure of L-2M, the depth of the local magnetic well at the center of the plasma column (in the microwave absorption region) is very small; accordingly, the population of the trapped particles is here also very small. It is well known that the number of trapped electrons in the microwave absorption region can affect the generation of the radial electric field, thereby changing the rate of plasma diffusion. Hence, the L-2M stellarator differs radically in this aspect from the devices mentioned above [14–18].

The plasma energy $W$ was measured from diamagnetic signals, using a technique described in detail in [20]. In that paper, the influence of the vacuum chamber on the results of diamagnetic measurements was assessed. It was shown that these results must be corrected when calculating the microwave power absorbed by the plasma. The value of the absorbed microwave power was calculated from the $dW/dt$ signal at the instant when the microwave power was switched off [21].
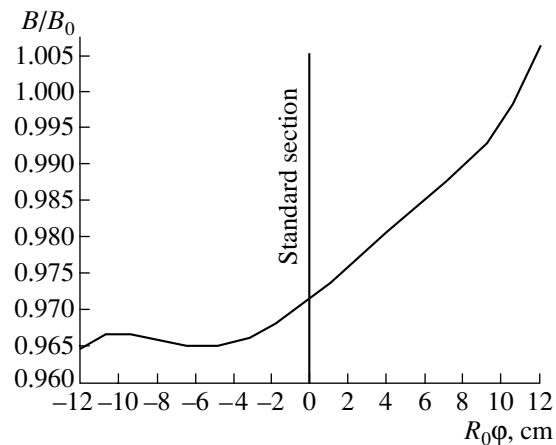
**Fig. 1.** Profile of the absolute value of the magnetic field along the magnetic axis of the L-2M stellarator ($\varphi$ is the toroidal angle in radians). The external vertical magnetic field is 0.5% of $B_0$.

In our experiments, the diamagnetic diagnostics was chosen as the "reference" diagnostics because it is reliable and efficient in operation. The plasma energy can be expressed in terms of the average density and the central temperature: $W \sim K n_e T(0)$, where $K$ is the form-factor, which depends only on the shape of the density and temperature profiles and which varied only slightly in the experiment. In addition, the plasma energy was estimated from the measurements of the Pfirsch–Schlüter field, which depends on the profile of the stellarator rotational transform and the pressure profile and anisotropy. A comparison of the results from both diagnostics for measuring the plasma energy provides information about possible changes in the shape of the pressure profile. The accuracy of the diamagnetic measurements was ~10%.

The plasma behavior at high power depositions per electron was studied in experiments in which the plasma density was reduced from $3 \times 10^{19}$ to $0.3 \times 10^{19}$ m$^{-3}$ and the microwave power was increased to 400 kW at a frequency of 75 GHz (the second harmonic, X mode). To provide the possibility of varying the plasma density in such a wide range, we took appropriate measures to reduce the plasma–wall interaction. As a result, radiative energy losses were considerably reduced. For this purpose, the vacuum chamber was repeatedly boronized in addition to the routine procedures of baking the chamber at temperatures of about 200°C and cleaning by a glow discharge. Due to these procedures, radiative losses measured by a bolometer were insignificant (no larger than 5–10 kW).

### 3. EXPERIMENTAL RESULTS

Figure 2 shows the radial profiles of the electron temperature determined from ECE measurements at different plasma densities $n_e$ and input powers of $P_{\mathrm{in}} =$
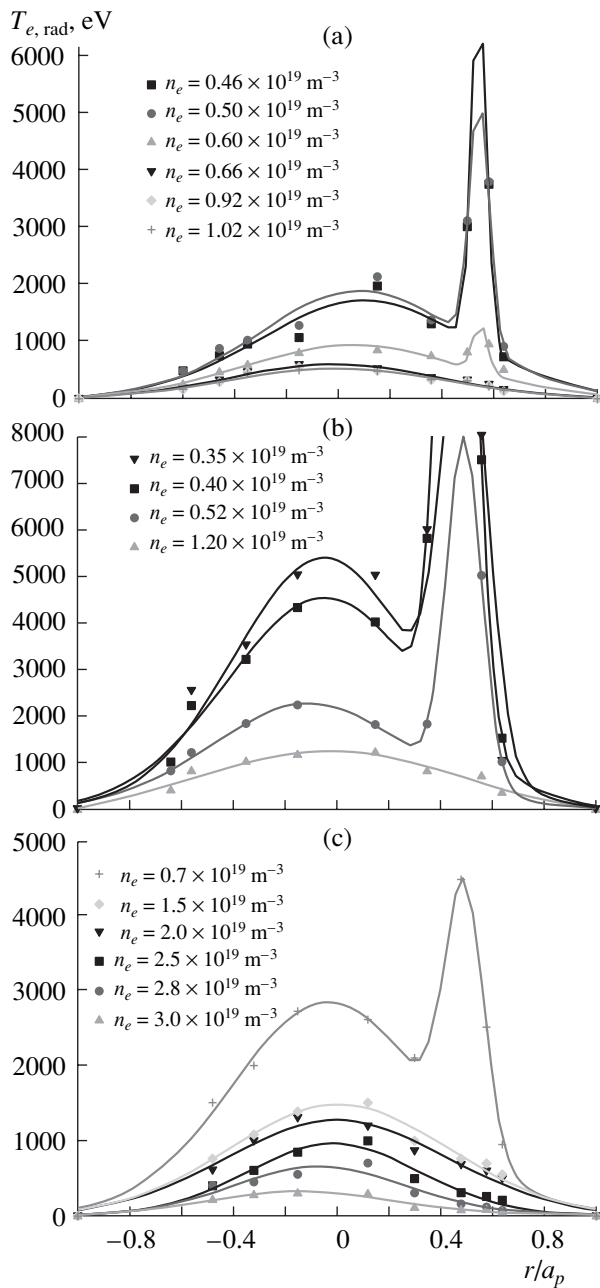
**Fig. 2.** Radial profile of $T_{e,\,\mathrm{rad}}$ for different plasma densities and heating power of (a) 120, (b) 170, and (c) 400 kW.



**Fig. 3.** $T_{e,\,\mathrm{rad}}$ vs. $P_{\mathrm{in}}/n_e$ for $P_{\mathrm{in}}$ = 120–400 kW.

120–400 kW. It can be seen from the figure that, even at densities of $n_e = 0.5 \times 10^{19}$ m$^{-3}$ ($P_{\mathrm{in}}$ = 120 kW), $n_e = 0.52 \times 10^{19}$ m$^{-3}$ ($P_{\mathrm{in}}$ = 170 kW), and $n_e = 0.7 \times 10^{19}$ m$^{-3}$ ($P_{\mathrm{in}}$ = 400 kW), the curves $T_e(r/a_p)$ become distorted and an enhanced emission appears at frequencies $f$ = 72–68 GHz. For a thermal (optically thick) plasma, these frequencies correspond to the plasma regions lying on the LFS from the magnetic axis at radii of $r/a_p$ = +0.4 to +0.7. Such an enhanced emission intensity may be related to a distortion of the Maxwellian electron energy distribution function and the appear-
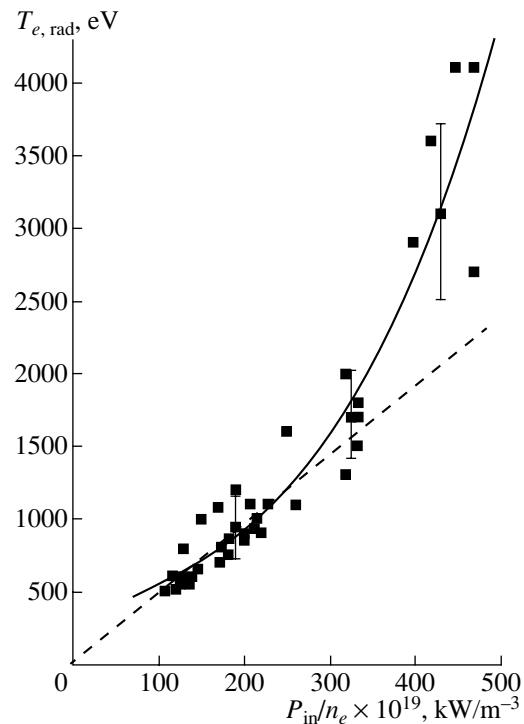
ance of suprathermal electrons. Note that, in this case, ECE emission was sensed by a receiver positioned on the LFS. Therefore, it may be suggested that the emission intensity ($T_{\mathrm{rad}}$) was actually even higher, since suprathermal electrons emit radiation with lower frequencies because of the relativistic shift of their gyrofrequency. Passing through the absorbent plasma layers, this radiation is additionally attenuated [6]. It can be seen from Fig. 2 that, even near the center of the plasma column, the radiation temperature at low plasma densities can be as high as several kiloelectronvolts. If the plasma optical depth is high ($\tau > 1$), then the radiation emitted by suprathermal electrons can remain undetected when measurements are performed from the LFS. However, the presence of these electrons in the plasma can manifest itself, e.g., as the abnormally fast ablation of a pellet injected into the plasma [22].

Analyzing the shapes of the curves in Fig. 2, we can conclude that, in the L-2M stellarator, we do not observe effects similar to those described, e.g., in [14–18], in which it was shown that, as the plasma density decreases, the curve $T_e(r/a_p)$ becomes peaked, the central temperature increases, and an internal transport barrier forms. This is probably due to the specific magnetic field structure of L-2M, which does not have substantial magnetic ripples in the central region of the plasma (in the microwave absorption region).

Figure 3 shows the generalized dependence of the electron temperature measured near the plasma center, $T_{e,\,\mathrm{rad}}(r/a_p = -0.15)$, on the parameter $P_{\mathrm{in}}/n_e$. It can be
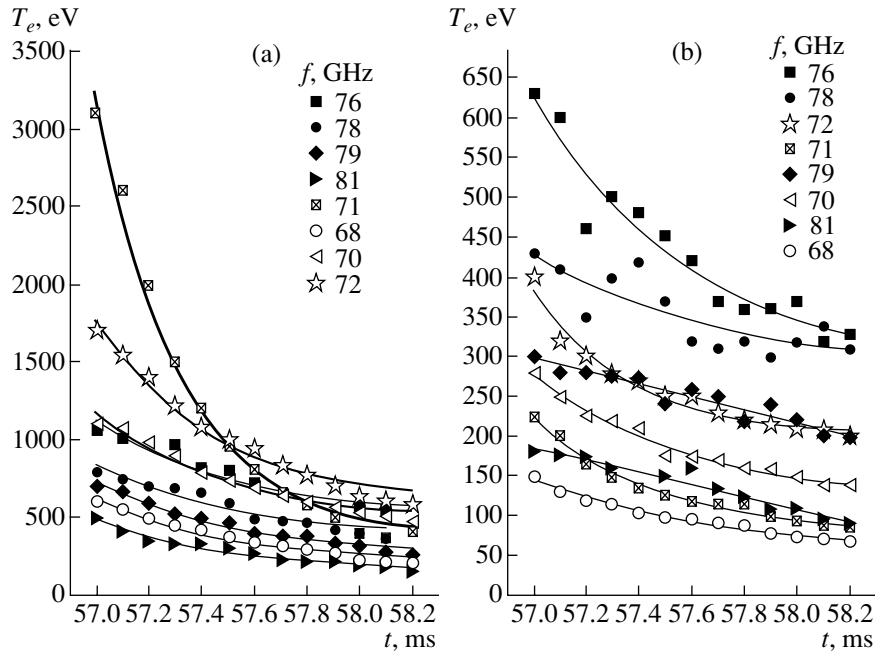
**Fig. 4.** Decay of the electron temperature determined from the ECE intensity at different frequencies after the microwave pulse is switched off ($t = 57$ ms) for (a) $n_e = 0.46 \times 10^{19}$ m$^{-3}$ and $P_{in} = 120$ kW and (b) $n_e = 0.91 \times 10^{19}$ m$^{-3}$ and $P_{in} = 120$ kW.

seen from the figure that this dependence is approximately linear only up to $P_{in}/n_e = 250$ kW/$10^{19}$ m$^{-3}$. As the parameter $P_{in}/n_e$ increases further, the curve departs strongly from the straight line, which indicates a deviation of the electron velocity distribution from a Maxwellian.

Figure 4 illustrates the temperature decay curves after the microwave pulse is switched off in experiments with two different plasma densities. At a lower plasma density (Fig. 4a), the radiative temperature determined from the emission intensity $T_{rad}$ at frequencies $f = 71$, 72, and 70 GHz, which reflects the behavior of suprathermal electrons, decays more rapidly compared to that at other frequencies (e.g., at a frequency of 71 GHz, it halves in 300 μs, whereas at a frequency of 76 GHz, it halves in 1200 μs). This means that the lifetime of suprathermal electrons is much shorter than that of bulk electrons. A qualitatively different behavior is seen in Fig. 4b, which shows the decay curves for a thermal plasma. In this case, the highest value of $T_e$ refers to the normalized radius $r/a_p = -0.15$ ($f = 76$ GHz) and the temperature determined from the ECE intensity at the other frequencies decays over longer times.

Comparing the results of measurements of the electron temperature from the ECE intensity with the data from diamagnetic measurements of the plasma energy, we can determine the experimental conditions (the range of the plasma densities and heating powers) in which ECE measurements provide the correct value for the temperature. In Fig. 5, the plasma energy $W$ derived

from diamagnetic measurements is plotted against the parameter $n_e T_{e, rad}$. Since the $T_e(r/a_p)$ profile at low plasma densities is substantially distorted in the region $r/a_p > 0$, we analyzed the temperature value at $r/a_p = -0.15$, which is close enough to the center of the plasma column. It can be seen from the figure that even such a simple analysis allows us to distinguish two regimes that differ in plasma density. In the "thermal" regime
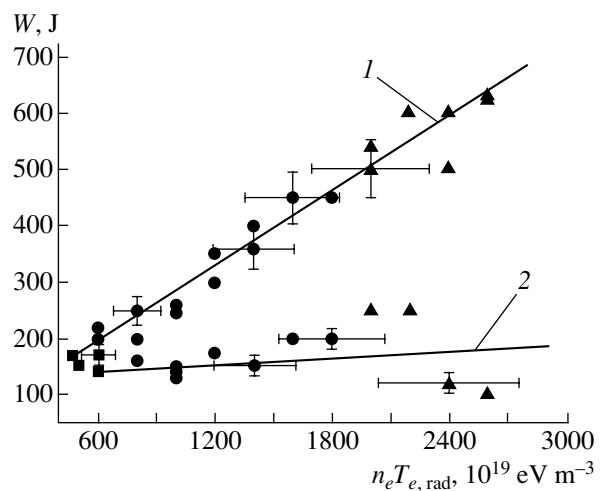


**Fig. 5.** Plasma energy $W$ as a function of the parameter $n_e T_{e, rad}$ for the (*1*) thermal regime ($n_e = (0.77–3) \times 10^{19}$ m$^{-3}$) and (*2*) nonthermal regime ($n_e = (0.3–0.75) \times 10^{19}$ m$^{-3}$).
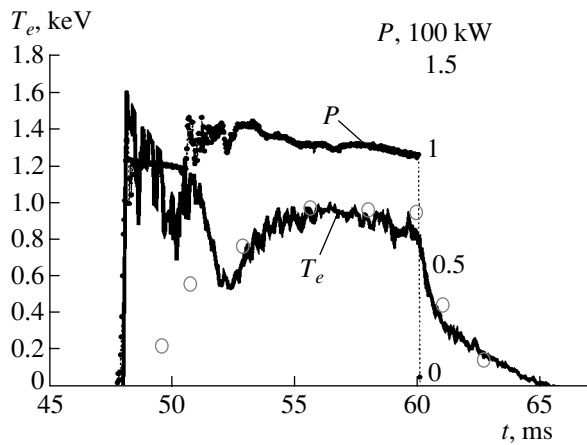
**Fig. 6.** Time behavior of the electron temperature $T_e$ and comparison with the TRANSZ code (circles) for the density $n_e = 0.8 \times 10^{19}$ m$^{-3}$ and heating power $P_{in} = 140$ kW.



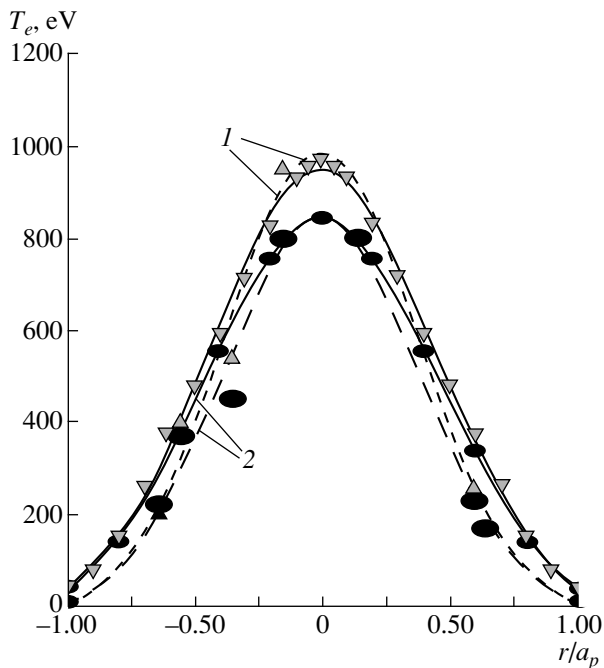**Fig. 7.** Radial profile of the electron temperature and comparison with the TRANSZ code for the densities $n_e =$ (*1*) $0.8 \times 10^{19}$ and (*2*) $1.3 \times 10^{19}$ m$^{-3}$. The solid line shows the results of calculations by the TRANSZ code, and the dashed line shows the experimental data.

(*1*), the plasma energy increases substantially with increasing density. However, one can see that, at low plasma densities, $n_e = (0.3–0.7) \times 10^{19}$ m$^{-3}$, a "nonthermal" regime (*2*) takes place, the Maxwellian velocity distribution function is distorted, and the radial profiles $T_e$ ($r/a_p$) are nonmonotonic (Fig. 2). Although the values of $n_e T_{rad}$ are fairly high in this case, the plasma energy is substantially lower than at the same values of

$n_e T_e$, but at higher densities. For example, we can compare two discharges presented in Fig. 2c. For $n_e = 1.5 \times 10^{19}$ m$^{-3}$ and $T_e$ ($r/a_p = -0.15$) = 1300 eV, we have $W = 530$ J, whereas for $n_e = 0.7 \times 10^{19}$ m$^{-3}$ and $T_{rad}$ ($r/a_p = -0.15$) = 2800 eV, we have $W = 250$ J. This fact allows us to conclude that, in the latter case, the temperature deduced from ECE measurements is not the true plasma temperature and can only be characterized as a radiative temperature $T_{rad}$. These specific features of the plasma behavior should be taken into consideration when determining the electron temperature by the ECE technique at low plasma densities and high input power.

The departure of the electron distribution function from a Maxwellian even for the bulk electrons at high input powers in large devices, such as JET and FTU, was discussed in [23, 24]. Note that, in those studies, the electron temperature was measured using both the ECE and Thomson scattering techniques. It should be remembered that, according to Kirchhoff's law, the idea of temperature refers to blackbody radiation from an optically thick plasma with a Maxwellian electron velocity distribution.

The reliability of ECE measurements of the temperature in a plasma with moderate and high densities was additionally confirmed by the results of calculations performed using the TRANSZ transport code, elaborated for the L-2M stellarator and described in [25]. Figures 6 and 7 compare the experimental dependences with calculations by the TRANSZ code. By slightly varying the gas-puffing parameter in the TRANSZ code, good agreement was achieved with the measured time dependence of the electron temperature $T_e(t)$ (Fig. 6) at a $T_e(r)$ profile close to the experimental one (Fig. 7). In particular, the simulation results agree with measurements of the plasma density profile, which yield a density distribution of the form $1 - x^n$, where $n = 4–6$ and $x = r/a_p$.

## 4. CONCLUSIONS

(i) ECRH experiments in regimes with high energy deposition in electrons have been carried out in the L-2M stellarator at heating powers of $P_{in} = 120–400$ kW and plasma densities of $(0.3–3.0) \times 10^{19}$ m$^{-3}$.

(ii) For the L-2M magnetic field structure, in which substantial magnetic ripples are absent in the power absorption region, no internal transport barriers similar to those observed at high input energies in CHS, W7-AS, TJ-II, LHD, etc., have been detected.

(iii) At plasma densities of $n_e > 10^{19}$ m$^{-3}$, the ECE spectrum is symmetric and the plasma energy is proportional to $n_e T_e$ (the thermal regime). A decrease in the plasma density or an increase in the heating power leads to a distortion of the radial plasma temperature profile. In this case, in spite of the increase in the emission intensity, the plasma energy measured by diagnostics does not increase (the nonthermal

regime). Hence, the results of temperature measurements by the ECE method should be interpreted with caution and additional experiments are required to determine the range of experimental conditions (the density, heating power, etc.) under which this method gives correct results.

(iv) The results of calculations of the discharge parameters by the TRANSZ transport code are in good agreement with the experimental data.

## ACKNOWLEDGMENTS

## REFERENCES

1. V. Alikaev, A. Bagdasarov, A. Berlizov, *et al.*, in *Proceedings of the 6th Joint Workshop on ECE and ECRH, Oxford, 1987*, p. 207.

2. S. Kubo, H. Idei, T. Shimozuma, *et al.*, in *Proceedings of the 19th IAEA Conference on Fusion Energy, Lyon, 2002*, Paper EX/C4-5Rb.

3. M. Bornatici, R. Cano, O. De Barbieri, and F. Engelmann, Nucl. Fusion **23**, 1153 (1983).

4. H. Piekaar and M. Rutgers, Rijnhuizen Report No. 80 (FOM Institute for Plasma Physics, Rijnhuizen, 1980).

5. TFR group and FOM ECRH team, Nucl. Fusion **28**, 1995 (1988).

6. M. Lontano, R. Pozzoli, and E. Suvorov, Nuovo Cimento **6313**, 529 (1981).

7. D. K. Akulina, Fiz. Plazmy **15**, 1386 (1989) [Sov. J. Plasma Phys. **15**, 806 (1989)].

8. H. Hartfuss, U. Gasparino, M. Tutter, *et al.*, in *Proceedings of the International Workshop on Collective Acceleration in Collisionless Plasma, Cargese, 1991* (Les Editions de Physique, Les Ulis-Cedex, 1991), p. 377.

9. J. Gelder, E. Westerhof, F. Schueller, and A. Donne, Plasma Phys. Controlled Fusion **40**, 1185 (1998).

10. D. K. Akulina, G. A. Gladkov, Yu. I. Nechaev, and O. I. Fedyanin, Fiz. Plazmy **23**, 32 (1997) [Plasma Phys. Rep. **23**, 28 (1997)].

11. G. Giruzzi, Nucl. Fusion **28**, 1413 (1988).

12. V. V. Alikaev and V. L. Vdovin, Fiz. Plazmy **9**, 928 (1983) [Sov. J. Plasma Phys. **9**, 538 (1983)].

13. A. S. Sakharov and M. A. Tereshchenko, Fiz. Plazmy **28**, 584 (2002) [Plasma Phys. Rep. **28**, 539 (2002)].

14. H. Maassberg, C. Beidler, V. Erckmann, *et al.*, J. Plasma Fusion Res. **1**, 103 (1998).

15. H. Maassberg, C. Beidler, and U. Gasparino, Phys. Plasmas **7**, 295 (2000).

16. A. Fujisawa, Plasma Phys. Controlled Fusion **44**, A1 (2002).

17. A. Fujisawa, H. Iguchi, T. Minami, *et al.*, Phys. Rev. Lett. **82**, 2669 (1999).

18. C. Alejaldre, L. Almoguera, J. Alonso, *et al.*, Nucl. Fusion **41**, 1449 (2001).

19. D. K. Akulina, G. M. Batanov, M. S. Berezhetskiĭ, *et al.*, Fiz. Plazmy **26**, 3 (2000) [Plasma Phys. Rep. **26**, 1 (2000)].

20. O. Fedyanin, D. Akulina, G. M. Batanov, *et al.*, J. Plasma Fusion Res. **1**, 235 (1998).

21. D. K. Akulina, G. M. Batanov, M. S. Berezhetskiĭ, *et al.*, Fiz. Plazmy **28**, 9 (2002) [Plasma Phys. Rep. **28**, 7 (2002)].

22. V. Timokhin, B. Kuteev, and V. Sergeev, in *Proceedings of the 29th EPS Conference on Plasma Physics and Controlled Fusion, 2002*; ECA **26B**, P-4.047 (2002).

23. V. Krivenski, in *Proceedings of the 26th EPS Conference on Plasma Physics and Controlled Fusion, Maastricht, 1999*; ECA **23J**, 385 (1999).

24. V. Krivenski, E. de la Luna, and G. Giruzzi, in *Proceedings of the 29th EPS Conference on Plasma Physics and Controlled Fusion, Montreux, 2002*; ECA **26B**, O-1.03 (2002).

25. S. E. Grebenshchikov, I. S. Danilkin, and A. B. Mineev, Fiz. Plazmy **22**, 609 (1996) [Plas. Phys. Rep. **22**, 551 (1996)].

*Translated by N.F. Larionova*

# Experimental and Numerical Studies of Plasma Production in the Initial Stage of Implosion of a Cylindrical Wire Array

**V. V. Aleksandrov\*, A. G. Alekseev\*, V. N. Amosov\*, M. M. Basko\*\*, G. S. Volkov\*,
E. V. Grabovskiĭ\*, A. V. Krasil'nikov\*, G. M. Oleĭnik\*, I. N. Rastyagaev\*,
P. V. Sasorov\*\*, A. A. Samokhin\*, V. P. Smirnov\*, and I. N. Frolov\***

*\*Troitsk Institute for Innovation and Fusion Research, Troitsk, Moscow oblast, 142190 Russia*
*\*\*Institute of Theoretical and Experimental Physics, Bol'shaya Cheremushkinskaya ul. 25, Moscow, 117259 Russia*
Received February 18, 2003; in final form, May 16, 2003

**Abstract**—The features are studied of plasma production in the initial stage of implosion of hollow cylindrical wire arrays at electric-field growth rates of $10^{12}$ V/(cm s). The results are presented from the analysis of both UV emission from the wire plasma and the discharge parameters in the initial stage of the formation of a Z-pinch discharge. It is found that, a few nanoseconds after applying voltage to a tungsten wire array, a plasma shell arises on the wire surface and the array becomes a heterogeneous system consisting of metal wire cores and a plasma surrounding each wire (a plasma corona). As a result, the current switches from the wires to the plasma. A further heating and ionization of the wire material are due primarily to heat transfer from the plasma corona. A model describing the primary breakdown along the wires is created with allowance for the presence of low-Z impurities on the wire surface. © 2003 MAIK "Nauka/Interperiodica".

## 1. INTRODUCTION

Implosion of cylindrical arrays (liners) made of micron tungsten or aluminum wires under the action of nanosecond current pulses has been studied since the late 1980s [1–4]. Due to the implosion of the wire array material, a Z-pinch discharge is formed near the array axis. In the final stage of the Z-pinch implosion, an intense soft X-ray pulse is generated that can be used in inertial confinement fusion (ICF) research, in studying fundamental physical problems (such as the equation of state of a substance with extreme parameters), and in certain practical applications.

In [1], it was shown that the main factor governing the implosion dynamics of a cylindrical wire array is the prolonged (up to the current maximum) production of the wire plasma. Recent studies [5–7] showed that the plasma on the wire surface is produced in the first few nanoseconds after the current starts to flow through the wire array. After the plasma is produced, the current switches from the wires to the plasma corona. In this case, the wire array becomes a heterogeneous system consisting of a cylindrical metal wire core and a plasma corona surrounding the wires. A further heating and ionization of the wire material is primarily due to heat transfer from the plasma corona. Plasma production from a single wire by microsecond current pulses was described in [8]. In the nanosecond range, plasma production was studied in detail in [9].

Important factors characterizing the initial state of the plasma-producing medium are the nonuniformity of the distribution of the plasma sources and the nonuniformity of the plasma production rate along the wires.

The nonuniformity of the distribution of the plasma sources can lead to the onset of various instabilities during plasma implosion, whereas the nonuniformity of the plasma production rate can result in a nonsimultaneous radial implosion of the plasma in different points along the array axis. Both these factors impede synchronous and compact implosion and, accordingly, decrease the emission power.

In this paper, we present the results of studying the initial stage of plasma production on the surfaces of tungsten wires during the implosion of a cylindrical wire array. By the initial stage of the formation of a Z-pinch discharge from a wire array, we mean the first 10–15 ns from the beginning of the current pulse, when the discharge current through a single wire is lower than 5 kA.

## 2. ARRANGEMENT OF THE EXPERIMENT

As wire liners, we used cylindrical hollow arrays assembled of eight or sixteen tungsten wires that were equally spaced along a cylindrical surface 8 or 20 mm in diameter. The array length was 10 mm. The diameter of the tungsten wires varied from 4 to 10 μm.

The scheme of connection of the wire array to the voltage source is shown in Fig. 1. The wire array was placed in the vacuum chamber of the ANGARA-5-1 facility [10]. The chamber was evacuated by oil-diffusion pumps. As a voltage source, we used one of the modules of the ANGARA-5-1. Because of this, the results obtained with arrays made of eight or sixteen wires in a single module could be compared with the

implosion of arrays assembled of much greater number of wires (64 or 128) in the full-scale experiments carried out in the ANGARA-5-1.

The microsecond prepulse of the voltage generator was suppressed by using a prepulse spark gap placed in front of the wire liner. The prepulse was suppressed to such extent that the electric field strength at the array was lower than 10 V/cm and the increase in the wire temperature during the prepulse was lower than 10°C.

To study the initial stage of plasma generation, the discharge current through the array was measured simultaneously with the voltage drop across the array. The current through the array was measured by a shunt with a time resolution of 5 ns.

A resistive divider for measuring the voltage on the axis of the wire array was connected coaxially to the anode and, with the help of a metal rod aligned with the array axis, to a cathode. The time resolution of the divider was 2 ns.

Since, in these experiments, we were dealing with rapidly varying currents, the voltage measured by the divider differed from the voltage across the wire by an inductive term proportional to the rate at which the magnetic flux in the circuit formed by the wire surface and divider connectors varied. In order to determine the voltage across the wire surface, this term should be subtracted from the divider readings. A specific feature of the voltage measurements on the array axis is that the contribution of the inductive term is very small and can be ignored. The reason for this is that the magnetic field produced by the current flowing through the array is mainly localized on the outside of the array and the interlinkage between the generator circuit and the divider circuit is weak.

Plasma generation on the wire surface was detected by the appearance of UV emission. As a UV detector, we used a diamond sensor made of natural Yakut diamond. The detector was devised and fabricated in the Troitsk Institute for Innovation and Fusion Research [11, 12].

The detector was placed at a distance of 3.6 m from the wire array. A 1-mm-thick quartz glass was placed in front of the detector. The relative spectral sensitivity of the detector with the quartz glass is shown in Fig. 2. The time resolution of the detector was 2 ns.

The time resolution of the optical frame system for recording the wire array images was 10 ns. The spatial resolution of the images was 40 μm, the depth resolution being about 2 mm. The dynamic range of the measurement system was about 20.
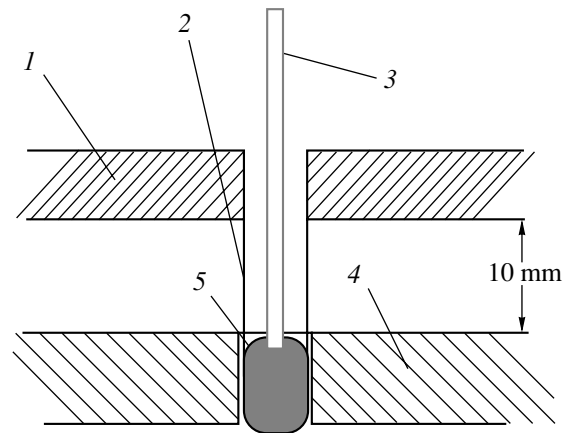
**Fig. 1.** Scheme of connection of the wire array and voltage divider to the voltage source: (*1*) anode of the ANGARA-5-1 facility, (*2*) wires, (*3*) metal rod connecting the voltage divider to the cathode, (*4*) cathode of the facility, and (*5*) cathode electrode of the wire array.
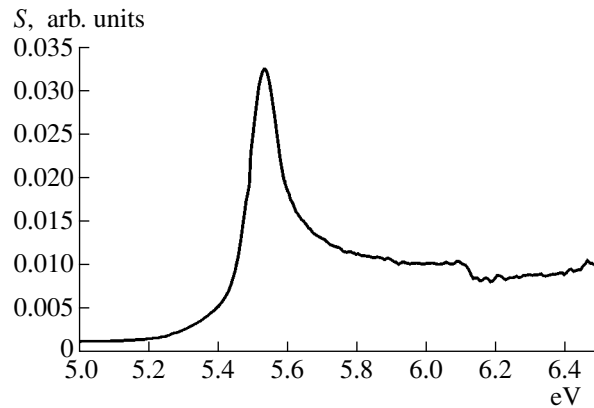


**Fig. 2.** Relative spectral sensitivity $S$ of a diamond detector with a quartz glass.

## 3. EXPERIMENTAL RESULTS AND THEIR COMPARISON WITH NUMERICAL SIMULATIONS

### *3.1. Breakdown along the Wire Surface*

The waveforms of the voltage on the axis of the system for several shots made with wire arrays and a single shot without wires (the no-load operating regime) are shown in Fig. 3. Without a wire array, the voltage on the axis during the first 50 ns was equal to the generator output voltage. During the first 20 ns, the maximum voltage drop across tungsten arrays with different outer diameters, different number of wires, and different wire diameters was in the range from 5 to 18 kV. The measured voltage pulses turned out to be substantially lower and shorter than the those measured in the no-load operating regime (without an array).
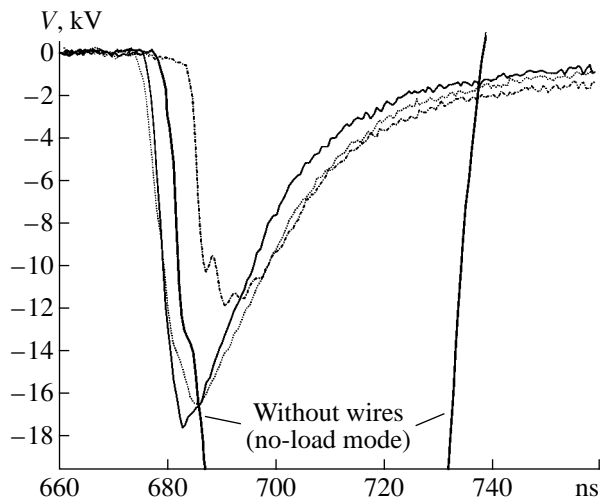
**Fig. 3.** Waveforms of the voltage on the axis for several shots with a wire array and a single shot without wires (the no-load operating mode).
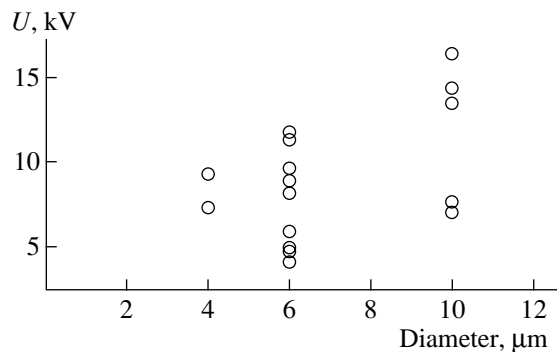


**Fig. 4.** Peak amplitude of the liner voltage $U$ as a function of the tungsten wire diameter.

Estimates of the wire resistance at the instant corresponding to the maximum voltage showed that it was lower than the initial resistance of the cold wires. Note that the decrease in the resistance of the heated current-carrying metal wires can only be explained by the production of a low-resistive plasma on the wire surface.

Figure 4 shows the maximum voltage at the array as a function of the diameter of tungsten wires. It can be seen that the maximum voltage at the array somewhat increases with increasing wire diameter.

Figure 5 shows the waveforms of the voltage on the wire array axis and the intensity of UV emission. The presence of UV emission means that a plasma is produced on the wire surface. The delay time of the UV pulse with respect to the voltage pulse varies from 6 to 10 ns in different shots.

Figure 6a shows typical waveforms of the voltage on the liner axis, $U(t)$, and the current per one wire, $J(t)$,

for a 8-mm-diameter wire array consisting of eight 10-$\mu$m tungsten wires. The results of processing of these signals are shown in Fig. 6b. These are three kinds of resistance per one wire: the total load resistance, $R_l(t)$; the wire resistance itself, $R_w(t)$; and the resistance of the plasma on the wire surface, $R_p(t)$. The total load resistance was calculated as the ratio $R_l(t) = U(t)/J(t)$. It can be seen that the ratio $U(t)/J(t)$ first increases due to the Joule heating of the wire and then decreases. The resistance $R_w(t)$ of a metal wire was calculated from the signal $U(t)$, taking into account the thermal resistivity coefficient, assuming that the entire electric power $U_2(t)/R_w(t)$ deposited in the wire is converted into heat, and ignoring energy losses by radiation and heat transfer. The plasma resistance $R_p(t)$ was calculated assuming that the plasma and metal wires are connected in-parallel and using the formula: $J(t)/U(t) = 1/R_w(t) + 1/R_p(t)$. A comparison of the time evolution of the plasma resistance with the recorded UV signal shows that the UV emission appears when the wire array resistance is already completely determined by the plasma resistance.

From the measurements of the load current and voltage in the initial stage of the process (before the plasma was produced on the wire surface), we could calculate the energy deposited in the wires due to ohmic heating. The calculations showed that, in most shots, the maximum temperature to which the tungsten wires were heated before the plasma was produced was lower than 2000°C. This temperature is substantially lower than the melting temperature of tungsten (3380°C).

The natural question arises as to why a plasma is produced on the wire surface.

The increase in the wire temperature during heating leads to the evaporation of low-$Z$ impurities from the wire surface. As a result, a thin gas shell is formed near the surface. This shell is then broken, which results in plasma production. Additional experiments in which a current of ~3 A per wire was passed through the wire array for a time longer than 5 $\mu$s showed that a temperature of 300–400°C was sufficient to evaporate the layer of a low-$Z$ coating material and produce plasma near the wire surface. Due to the rapid plasma expansion, the cross section of the current-carrying plasma channel increases, which leads to a sharp decrease in the channel resistance. The results of numerical simulations of the plasma production on the surface of a tungsten wire with a low-$Z$ impurity coating is presented in the next section.

As was shown in [13], the breakdown of the produced gas shell can be initiated by electron emission from the wire surface. The emission is enhanced by the strong radial electric field that appears at some segment of a small-diameter wire at a certain configuration of electrodes. This field can exceed the axial electric field at the wire by a factor of 10 to100. The dependence of this effect on the wire diameter will be discussed at the end of the present paper.

Due to the presence of plasma on the wire surface, the current switches from the wires to the plasma. The main current begins to flow through the plasma, thereby heating it. A further heating of the wires is mainly due to heat transfer from the hot plasma to the wire surface. In this case, the contribution of the current flowing directly through the wires is relatively small.

We note that the warming of wires in vacuum to redness before an experiment had little effect on both the production of the surface plasma and the time evolution of the array resistance.

### 3.2. Numerical Simulations of Plasma Production on the Surface of a Tungsten Wire with and without Coating

To gain a better insight into the above experiments on measuring the time evolution of the resistance of a wire array under the action of a high-power current pulse, we carried out numerical simulations of this process. The simulations were performed using the NPINCH one-dimensional (radius–time) magnetohydrodynamic code [14, 15]. This code was improved by introducing an equation of state for metals over a wide range of densities and temperatures [16]. The equation of state takes into account the phase transition from a condensed to a gaseous state, and then to plasma, but ignores the transitions between the solid and liquid states. To calculate the kinetic coefficients of a condensed substance (the electron thermal conductivity, electric conductivity, heat exchange rate between ions and electrons, etc.), we used the procedure described in [17]. For the gas–plasma domain, we used the procedure described in [18]. The latter procedure is based on the well-known formulas for a hot magnetized plasma [19]. We simulated the time evolution of a 6-μm tungsten wire under the action of a given current pulse with a maximum amplitude of about 1 kA and a rise time of 20 ns.

The simulations were performed for both uncoated tungsten wires and wires coated by a thin layer of a low-$Z$ material (carbon), which modeled a low-$Z$ impurity on the tungsten surface. The calculation results are shown in Fig. 7.

The given time dependence of the current through an uncoated wire and the calculated waveform of the electric field strength on the wire axis are shown in Fig. 7a. It can be seen that, in this case, the electric field reaches 120 kV/cm, which is several times higher than the experimental value. This result confirms our assumption that, in real experiments, wires can never be considered clean. The decrease in the amplitude of the liner voltage can be explained by the presence of a thin low-$Z$ coating on wires. Such a coating may be due to the deposition of vacuum oil vapor on a wire or the technology of wire fabrication.

To clarify the influence of the low-$Z$ impurity coating on the electric characteristics of a wire, we divided
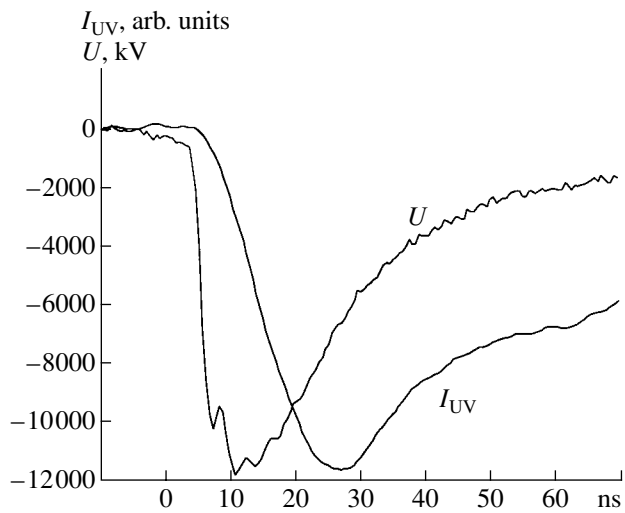


**Fig. 5.** Waveforms of the voltage on the array axis ($U$) and intensity of UV emission ($I_{UV}$) for an array consisting of eight 6-μm tungsten wires.
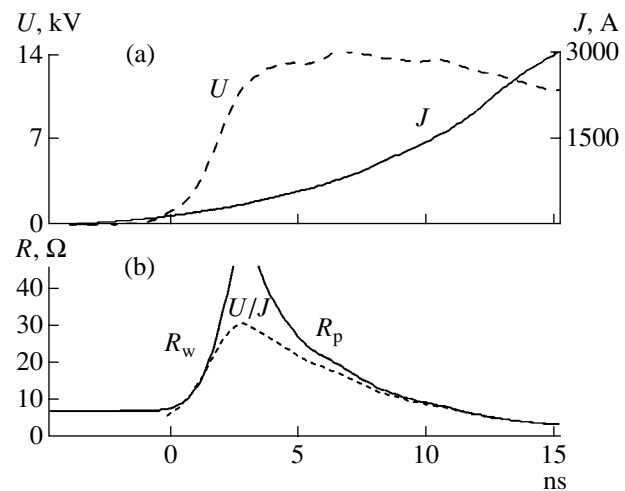


**Fig. 6.** (a) Waveforms of the voltage $U(t)$ across an 8-mm-diameter wire array consisting of eight 10-μm tungsten wires and the current through one wire $J(t)$. (b) Time evolution of the resistances (per one wire) calculated from the voltage and current waveforms: the total load resistance $U(t)/J(t)$, the wire resistance $R_w(t)$, and the resistance of the surface plasma $R_p(t)$.

a simulation into two stages. In the first stage (up to 6.75 ns), the heating of a clean wire was calculated. At the end of this stage, the temperature on the tungsten wire surface was 0.05 eV. The calculation was then continued assuming that the wire was coated with a 0.3-μm carbon layer in a gaseous state (with a mass per unit length of $1.8 \times 10^{-10}$ g/cm). Thus, we simulated the primary evaporation of the low-$Z$ coating. The calculated waveform of the voltage across a coated wire is shown in Fig. 7b. In this case, both the voltage amplitude and

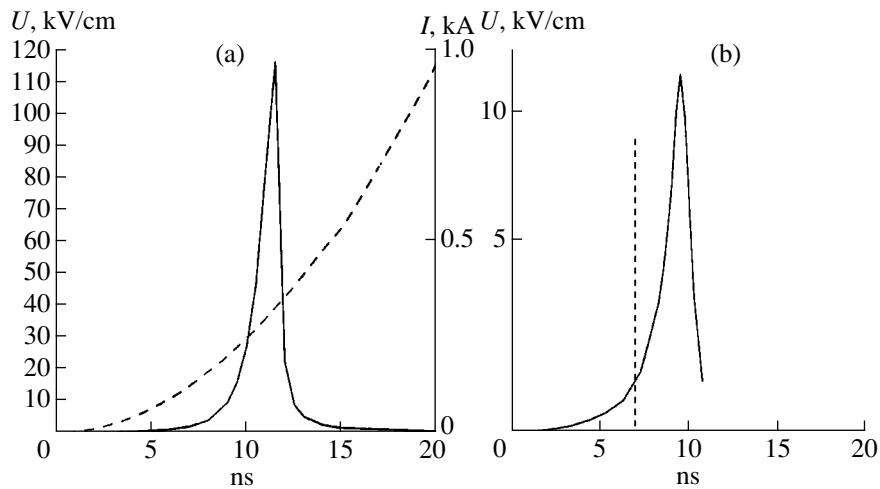**Fig. 7.** Calculated waveforms of the electric field at the axis of a 6-μm tungsten wire during the current pulse: (a) an uncoated wire (the solid and dotted curves show the electric field and current, respectively, and (b) a wire coated with a model gaseous carbon shell with a density per unit length of $1.8 \times 10^{-10}$ g/cm (the solid curve shows the electric field, and the vertical dotted line indicates the instant of evaporation of the coating).
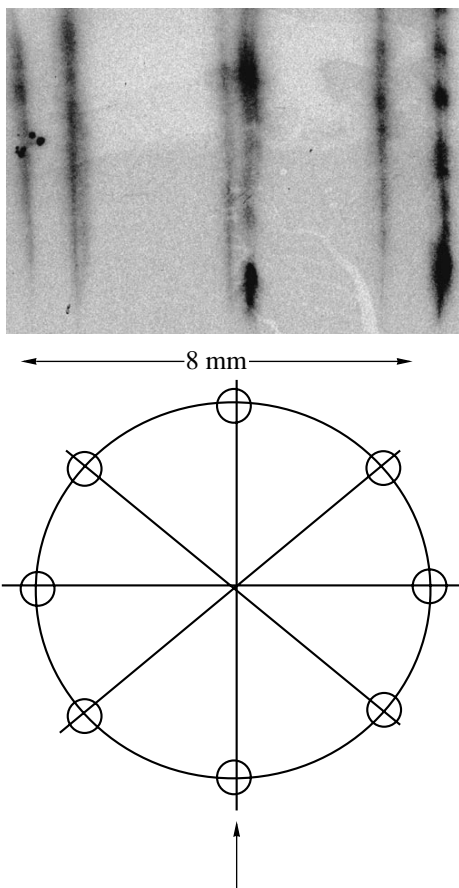


**Fig. 8.** Visible-light image of an array consisting of 7.5-μm eight tungsten wires with a current of 3 kA per wire. A schematic of the wire array and the viewing direction are shown at the bottom.

the shape of the voltage pulse are much closer to the experimental results. Breakdown along the wire is delayed from the beginning of the second stage by 2.5 ns, which is required for the necessary reduction in the density of the evaporated material due to expansion. Just after the breakdown of the gas shell and the formation of a plasma corona, the main current begins to flow through the corona, thereby heating it, and the Joule heating of the wire almost terminates. Up to this time, the characteristic tungsten temperature is 0.23 eV.

The above numerical simulations are only a rough approximation to the actual processes of the generation of a primary plasma and subsequent plasma production. Nevertheless, our model at least does not contradict the experimental data.

### 3.3. Spatial Nonuniformity of Plasma Generation

To study the process of energy deposition in a wire liner in the initial stage of implosion, we took frame-by-frame photographs of the liner in visible light. An image of an array consisting of eight 7.5-μm tungsten wires at the instant when the current reached a value of 3 kA per wire is given in Fig. 8. A characteristic feature of the liner image is a pronounced nonuniformity of the distribution of the emission intensity along the wire. The emission intensities of the individual wires are also slightly different. In the image, one can see well-defined regions with a nonuniform distribution of emission. The liner images testify to a nonuniform energy deposition in the wires in the initial stage of implosion. Note that the oscillations of the voltage on the array axis (see Fig. 5) may be attributed to the jitter in the breakdown time of the individual wires. This may be caused both by the factors affecting plasma production

(e.g., the nonuniformity of the impurity distribution along the wire) and by the onset of thermal and ionizational instabilities.

We note that the nonuniformity of the emission intensity along the wires begins to decrease when the current exceeds 5 kA per wire.

## 4. DISCUSSION OF THE RESULTS

### *4.1. Role of the Wire Diameter*

Measurements of the electric characteristics of discharges through cylindrical hollow arrays made of tungsten wires showed that the wire-material plasma, which is generated near the wires several nanoseconds after the beginning of the current pulse, plays the dominant role in the development of the discharge. From this moment on, the wire array can be regarded as a heterogeneous system consisting of dense wire cores and a plasma corona surrounding the wires. Hence, the question arises as to mechanisms for plasma generation at such low values of the tangential electric field on the wire surface.

In [9], it was supposed that the radial electric fields can play an important role in initiating the breakdown of the gas evaporated from the wire surface. Because of the small wire diameter, the radial electric field can be higher than the axial field by a factor of 100 [13]. The smaller the wire diameter, the higher the radial electric field, all other factors being the same. This field is produced by the charges that are accumulated on the wires in the initial stage of the voltage pulse before breakdown (i.e., before the plasma is produced on the wire surface). After breakdown, these charges flow down onto the electrodes of the liner unit. The direction and strength of the radial electric field on the wire surface depend on the electrode configuration. When the wire is connected perpendicularly to two infinite plane-parallel electrodes that are at different potentials, the radial electric field is zero. For other electrode configurations, the radial field is nonzero. It may happen that, on one segment of the wire, the field is directed toward the wire, whereas on the other segment, it is directed away from the wire.

The field directed toward the wire can enhance electron emission from the wire surface and cause the electron-impact ionization of the gas shell surrounding the wire. In [13], it was shown that electron emission from the wire results in an electron current in crossed electric and magnetic fields outside the wire. Electrons from this flow can cause the heating and evaporation of not only impurities, but also of a thin ($\sim10^{-3}$ μm) layer of the main wire material.

Gas breakdown occurs and plasma is produced at the instant when the gas density and electric field reach certain values. If surface gas breakdown on wires with different diameters takes place in the same radial field, then, for a thinner wire, gas breakdown will occur at lower values of the axial electric field because of the
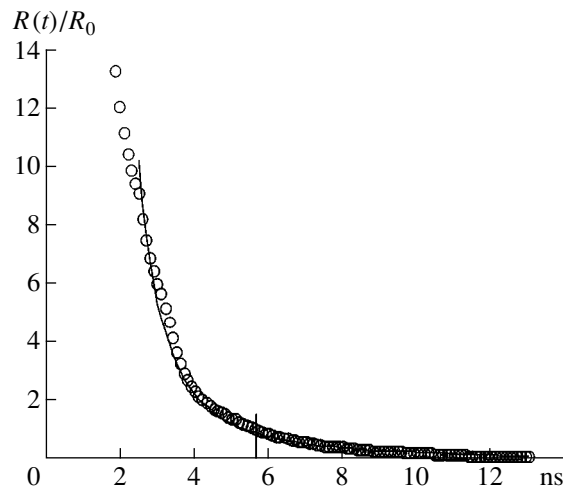
**Fig. 9.** Time evolution of the ratio of the plasma resistance near a single wire, $R(t)$, to the initial resistance of a cold wire, $R_0$. The circles show the experimental data, and the solid curve shows the result of simulations of an expanding plasma with an electron temperature of $T_e \sim 24$ eV. The instant at which the plasma resistance becomes equal to the resistance of the cold wire is indicated.

higher radial field on the wire surface. This conclusion is supported (in spite of the few statistics available and the large scatter in the data) by the results presented Fig. 4.

### *4.2. Estimates of the Plasma Parameters*

Under some assumptions, we can estimate the parameters of the produced plasma from the observed time dependences of the liner voltage and current, as well as from the plasma resistance calculated using these dependences. Let us consider a rather rough model. Let the electron temperature of the plasma surrounding each wire be $T_e$ [eV]. We assume that the plasma conductivity obeys the Spitzer law, the average ion charge number $Z$ is proportional to $T_e^{0.5}$, and the velocity of plasma expansion into vacuum is determined by its temperature. It turns out that this model agrees best with the measured liner voltage and current for a tungsten plasma with an electron temperature of $T_e \sim 20$–$30$ eV. Figure 9 shows the waveforms of the ratio of the plasma resistance near a single wire to the initial resistance of a cold wire. One of the profiles is calculated from the measured voltage and current (circles), while the other profile is calculated using the above model for a tungsten plasma with an electron temperature of $T_e \sim 24$ eV (solid curve). The vertical line near 5.5 ns indicates the time when the plasma resistance becomes equal to the initial wire resistance. In this case, the velocity of plasma expansion into vacuum is $\sim10^6$ cm/s. Hence, 10 ns after the plasma appears on the wire surface, the radius of the plasma column reaches $\sim100$ μm. These simple estimates are

qualitatively consistent with the above numerical simulations of plasma production on the surface of a tungsten wire.

Unfortunately, such estimates cannot be extended to longer times because, at these times, the plasma radius becomes larger than the skin depth. In addition, the model ignores a very important factor, namely, the presence of a magnetic field. First, the magnetic field produced by the current flowing through the wire should impede plasma expansion. Second, the total magnetic field of all the wires should result in the acceleration of the current-carrying plasma toward the array axis under the action of the Ampére force.

The magnetic field produced by the wire array is lower than the magnetic field of a single wire by a factor $d/2\pi r$, where $d$ is the distance between the wires and $r$ is the wire radius. In view of the fact that the gas-kinetic plasma pressure on the wire surface exceeds the pressure of the magnetic field produced by the current flowing through a single wire, the Ampére force caused by the total current cannot substantially affect the expansion of the plasma column as a whole during the first 10 ns. This conclusion, however, results from the roughness of the model. The density of the tungsten ions on the boundary of the plasma column decreases smoothly. Inside the array, there is a region where the Ampére force can accelerate a small amount of a low-density plasma toward the array axis. This results in the appearance of a plasma precursor [1], whose velocity ($\sim 10^7$ cm/s) is one order of magnitude higher than the expansion velocity of the plasma column [13].

There are also other factors that are not taken into account by the above model, in particular, the nonuniform plasma production along the wires and the nonsimultaneous plasma production on different wires. That these factors really do exist can be seen in Fig. 8. However, even such a rough model has allowed us to estimate the plasma temperature and to obtain the lower estimate for the tungsten ion density from the measured current–voltage characteristics.

## 5. CONCLUSIONS

It has been found that, a few nanoseconds after the beginning of the current pulse, a plasma is produced on the wire surfaces and the wire array becomes a heterogeneous system consisting of the metal wires and the plasma on their surfaces. The current switches from the wires to the plasma. As a result, the resistance of the system decreases and, accordingly, the voltage drop across the array decreases. A further heating of the wires is primarily provided by the current flowing through the plasma and by heat transfer from the plasma, rather than by the current flowing through the wires.

## REFERENCES

1. M. B. Bekhtev, V. D. Vikharev, S. V. Zakharov, *et al.*, Zh. Éksp. Teor. Fiz. **95**, 1653 (1989) [Sov. Phys. JETP **68**, 955 (1989)].
2. I. K. Aĭvazov, M. B. Bekhtev, V. V. Bulan, *et al.*, Fiz. Plazmy **16**, 645 (1990) [Sov. J. Plasma Phys. **16**, 373 (1990)].
3. R. B. Spielman, C. Deeney, G. A. Chandler, *et al.*, Phys. Plasmas **5**, 2105 (1998).
4. S. V. Lebedev, F. N. Beg, S. N. Bland, *et al.*, Phys. Plasmas **8**, 3734 (2001).
5. A. V. Branitskii, E. V. Grabovskii, M. V. Frolov, *et al.*, in *Proceedings of the 12th International Conference on High-Power Particle Beams, Haifa, 1998*, p. 599.
6. A. A. Aleksandrov, A. V. Branitskiĭ, G. S. Volkov, *et al.*, Fiz. Plazmy **27**, 99 (2001) [Plasma Phys. Rep. **27**, 89 (2001)].
7. A. Alexandrov, A. Branitskii, E. V. Grabovskii, *et al.*, in *Inertial Fusion Sciences and Application 99*, Ed. by Ch. Labaune, W. J. Hogan, and K. A. Tanaka (Elsevier, Paris, 1999), p. 621.
8. S. V. Lebedev and A. I. Savatinskiĭ, Usp. Fiz. Nauk **144**, 215 (1984) [Sov. Phys. Usp. **27**, 749 (1984)].
9. G. S. Sarkisov, B. S. Bauer, and D. S. De Groot, Pis'ma Zh. Éksp. Teor. Fiz. **73**, 74 (2001) [JETP Lett. **73**, 69 (2001)].
10. Z. A. Al'bikov, E. P. Velikhov, A. I. Veretennikov, *et al.*, At. Énerg. **68**, 26 (1990).
11. A. G. Alekseyev, V. N. Amosov, V. S. Khrunov, *et al.*, *Diagnostics for Experimental Thermonuclear Fusion Reactors*, Ed. by P. E. Stott, G. Gorini, and E. Sindoni (Plenum, New York, 1996).
12. S. F. Kozlov, US Patent No. 3668400 (June 6, 1972).
13. G. S. Sarkisov, P. V. Sasorov, K. W. Struve, *et al.*, Phys. Rev. E **66**, 046413 (2002).
14. N. A. Bobrova, T. L. Razinkova, and P. V. Sasorov, Fiz. Plazmy **18**, 517 (1992) [Sov. J. Plasma Phys. **18**, 269 (1992)].
15. N. A. Bobrova, S. V. Bulanov, T. L. Razinkova, and P. V. Sasorov, Fiz. Plazmy **22**, 387 (1996) [Plasma Phys. Rep. **22**, 349 (1996)].
16. M. M. Basko, Teplofiz. Vys. Temp. **23**, 483 (1985).
17. M. Basko, Th. Löwer, V. N. Kondrashov, *et al.*, Phys. Rev. E **56**, 1019 (1997).
18. N. A. Bobrova and P. V. Sasorov, Fiz. Plazmy **19**, 789 (1993) [Plasma Phys. Rep. **19**, 409 (1993)].
19. S. I. Braginskii, in *Reviews of Plasma Physics*, Ed. by M. A. Leontovich (Gosatomizdat, Moscow, 1963; Consultants Bureau, New York, 1965), Vol. 1.

*Translated by E.L. Satunina*

# Thermal Nonlinearity of Potential Surface Waves at a Plasma–Metal Interface

**N. A. Azarenkov, Yu. A. Akimov, and V. P. Olefir**

*Institute of High Technologies, Karazin Kharkov National University, pr. Kurchatova 31, Kharkov, 61108 Ukraine*
Received December 5, 2002; in final form, March 12, 2003

**Abstract**—A study is made of the effect of the heating of plasma electrons in the field of a potential surface wave on the wave dispersion properties. The wave is assumed to propagate along the boundary between a metal and a finite-pressure plasma. Different mechanisms for electron energy losses are considered in the weak heating approximation. The spatial distribution of the plasma electron temperature under nonlocal heating conditions is derived on the basis of the electron energy balance equation. Expressions for the spatial damping rate and the nonlinear shift of the wavenumber are analyzed for different values of the plasma parameters. The results obtained are valid for both semiconductor and gaseous plasmas. © 2003 MAIK "Nauka/Interperiodica".

## 1. INTRODUCTION

In recent years, the properties of surface waves (SWs) in plasma–metal structures have been actively studied both theoretically and experimentally [1, 2]. Interest in such structures is associated with their numerous applications in plasma and semiconductor electronics, gas discharges, and various plasma technologies [1]. The linear theory of SWs in plasma–metal structures has been developed quite well [2, 3]. However, the behavior of an SW can become essentially nonlinear even when the amplitude of its field is fairly small [4–6]. Depending on the values of the plasma parameters, different nonlinear self-interaction mechanisms such as the resonant generation of the second harmonic of an SW [2], the nonlinear damping of SWs [2, 7], the self-interaction of SWs due to the nonlinearities of quasi-hydrodynamic equations [2, 8], and the ionizational [9, 10] and thermal [11] nonlinearities of SWs, can be dominant.

The objective of the present paper is to investigate the thermal nonlinearity–induced self-interaction of SWs at the boundary between a metal and a warm plasma.

## 2. FORMULATION OF THE PROBLEM

We consider the nonlinear self-interaction of a finite-amplitude potential SW caused by the heating of plasma electrons in its field. We assume that the wave propagates along the interface between a metal and a finite-pressure plasma. We also assume that the plasma occupies the half-space $x > 0$ and is bounded at $x = 0$ by a perfectly conducting plane metal surface. It is well known that the properties of SWs in an inhomogeneous plasma are governed essentially by the character of the spatial distribution of the plasma density in the transi-

tion layer. In plasmas with large and small density inhomogeneities, the properties of SWs are determined by the integral parameters of the plasma in the region where the wave field is localized. [7]. In these cases, the plasma–metal boundary can be considered sharp and the plasma density can be assumed to be uniform and equal to its mean value in the localization region of the SW. This approach was found to be efficient and to agree well with the experimental data, in particular, with those from experimental investigations of gas discharges maintained by SWs. In what follows, we will assume that the plasma–metal interface is sharp and the plasma is homogeneous.

The effective collision frequency of electrons with scattering centers, $\nu = \nu_{col} + \nu_* + \nu_i$ (where $\nu_{col}$ is the elastic collision frequency, $\nu_*$ is the excitation frequency, and $\nu_i$ is the ionization frequency), is assumed to be much lower than the wave frequency $\omega$. In a gaseous plasma, the role of the scattering centers can be played by ions, working-gas particles, and impurities. In a semiconductor plasma, the electrons can also be scattered by optical and acoustic phonons [12–14].

The mechanism for the self-interaction of an SW operates as follows [2, 11]. The plasma electrons acquire additional energy from the wave and then transfer it to the scattering centers via collisions. As a result, the spatial distribution of the electron temperature, which determines the electron collision frequency and the electron pressure in the plasma, changes. These processes alter the electrodynamic parameters of the plasma, which govern the dispersion properties of SWs.

It should be noted that the thermal mechanism for self-interaction is closely related to the ionization nonlinearity [2, 9, 10]. The effect of the ionization nonlinearity is that, as the wave amplitude increases, the spatial distribution of the electron temperature changes; as

a consequence, the spatial distribution of the plasma density also changes, since the rates of elementary processes in the plasma depend on the electron temperature. Hence, an increase in the wave amplitude alters the dispersion properties of SWs. When the amplitude of an SW is small (i.e., the nonlinearity is weak), the wave-produced perturbations of the plasma parameters (the electron temperature, electron pressure, electron collision frequency, etc.) are much smaller than their unperturbed values. In this case, the effect of thermal and ionization nonlinearities on the dispersion properties of SWs can be described in the additive manner [2]. This circumstance allows the two self-interaction mechanisms to be studied independently.

## 3. RESULTS OF THE LINEAR THEORY

The dispersion properties of an SW propagating along the interface between a metal and a free plasma, as well as the spatial distribution of its potential, were investigated in [3] in the linear wave-field approximation. In that paper, it was shown that a necessary condition for the existence of SWs at a plasma–metal boundary is that the thermal velocity of the plasma electrons, $V_{Te} = \sqrt{2T_e/m_e}$ (where $T_e$ is the plasma electron temperature and $m_e$ is the mass of an electron), should be finite. In the general case of a collisional semiconductor plasma, the equation for the SW potential $\Psi$ has the form

$$
\frac{\partial^4 \Psi}{\partial x^4} + \frac{\partial^2 \Psi}{\partial x^2}\left[\frac{\omega\omega'}{V_{Te}^2}\left(1 - \frac{\omega_{pe}^2}{\varepsilon_0\omega\omega'}\right) - 2k_2^2\right]
$$
$$
+ k_2^2\Psi\left[k_2^2 - \frac{\omega\omega'}{V_{Te}^2}\left(1 - \frac{\omega_{pe}^2}{\varepsilon_0\omega\omega'}\right)\right] = 0,
\tag{1}
$$

where $\varepsilon_0$ is the permittivity of a semiconductor crystal lattice (for a gaseous plasma, we set $\varepsilon_0 = 1$), $\omega_{pe}$ is the electron plasma frequency, $\omega' = \omega + i\nu$, and $k_2$ is the complex wavenumber.

By analogy with [3], we seek the spatial distribution of the SW potential in the form

$$
\Psi(x, y, t) = (A_1 e^{-\lambda_1 x} + A_2 e^{-\lambda_2 x})e^{i(k_2 y - \omega t)},
\tag{2}
$$

where $A_1$ and $A_2$ are constants and the quantities $\lambda_{1,2}$ characterize the penetration of the SW field into the plasma. The expressions for $\lambda_{1,2}$ can be derived by substituting representation (2) into Eq. (1) for the potential:

$$
\lambda_{1,2}^2 = \frac{1}{2}\frac{\omega\omega'}{V_{Te}^2}\left\{2\frac{k_2^2 V_{Te}^2}{\omega\omega'} - \left(1 - \frac{\omega_{pe}^2}{\varepsilon_0\omega\omega'}\right) \pm \left(1 - \frac{\omega_{pe}^2}{\varepsilon_0\omega\omega'}\right)\right\}.
\tag{3}
$$

Using boundary conditions implying that the SW potential and the normal component of the hydrodynamic electron velocity vanish at the plasma–metal interface, we can obtain the dispersion relation

$$
1 + k_2^2 r_{De}^2 - r_{De}^2(\lambda_1^2 + \lambda_1\lambda_2 + \lambda_2^2) = 0,
\tag{4}
$$

where $r_{De} = \sqrt{\varepsilon_0}V_{Te}/\omega_{pe}$ is the electron Debye radius. The solution $k_2$ to this dispersion relation can be represented as

$$
k_2^2 = \frac{\omega\omega'}{V_{Te}^2}\frac{\varepsilon_0\omega'^2}{\varepsilon_0\omega'^2 + \omega_{pe}^2\omega'/\omega}.
\tag{5}
$$

According to solution (5), electron collisions cause an SW to be damped (the spatial damping rate of the wave is determined by the imaginary part of the wavenumber $k_2$). Since solution (5) is rather complicated, we restrict ourselves to investigating the self-interaction of an SW under the assumption that the plasma is sufficiently dense for the condition $\omega^2 \ll \omega_{pe}^2/\varepsilon_0$ to be satisfied. In this case, expressions (3) and (5) simplify to

$$
k_2 = k_2' + ik_2'' = \frac{\omega}{V_{Te}}\frac{\sqrt{\varepsilon_0}\omega}{\omega_{pe}}\left(1 + i\frac{\nu}{\omega}\right),
\tag{6}
$$

$$
\lambda_1 = \lambda_1' + i\lambda_1'' = \frac{\omega_{pe}}{V_{Te}\sqrt{\varepsilon_0}}\left(1 - \frac{1}{2}\varepsilon_0\frac{\omega^2}{\omega_{pe}^2}\left(1 + i\frac{\nu}{\omega}\right)\right),
$$
$$
\lambda_2 = \lambda_2' + i\lambda_2'' = \frac{\omega}{V_{Te}}\sqrt{\varepsilon_0}\frac{\omega}{\omega_{pe}}\left(1 + i\frac{\nu}{\omega}\right).
\tag{7}
$$

It should be noted that the expressions obtained are valid in the potential approximation for the waves under consideration. In the case of a sufficiently dense plasma, this approximation imposes the following restriction on the thermal velocity of plasma electrons: $V_{Te} \ll c\sqrt{\varepsilon_0}\,\omega/\omega_{pe}$, where $c$ is the speed of light in vacuum. An analysis of expression (6) shows that the phase velocity of an SW is much higher than the electron thermal velocity, which means that the hydrodynamic plasma description used here to investigate SWs is valid. Such a large difference between the phase velocity of an SW and the electron thermal velocity allows us to ignore collisionless Landau damping.

## 4. SPATIAL DISTRIBUTION OF THE ELECTRON TEMPERATURE

We consider a weak thermal nonlinearity, such that the perturbation of the electron temperature, $\delta T$, produced by heating in the SW field is much smaller than the equilibrium temperature $T_0$: $T = T_0 + \delta T$, with $\delta T \ll T_0$. We assume that the perturbation of the collision frequency, $\delta\nu = \delta\nu_{col} + \delta\nu_* + \delta\nu_i$, is much less than the unperturbed collision frequency $\nu$ in the absence of an SW. In this case, the frequency of electron collisions at

a temperature close to the unperturbed temperature $T_0$ can be described by the expressions

$$\nu_{col}(T) = \nu_{col}(T_0) + \delta\nu_{col},$$

$$\delta\nu_{col} = \delta T \frac{\partial\nu_{col}}{\partial T}\bigg|_{T_0} \ll \nu_{col}(T_0),$$

$$\nu_*(T) = \nu_*(T_0) + \delta\nu_*, \quad \delta\nu_* = \delta T\frac{\partial\nu_*}{\partial T}\bigg|_{T_0} \ll \nu_*(T_0),$$
(8)

$$\nu_i(T) = \nu_i(T_0) + \delta\nu_i, \quad \delta\nu_i = \delta T\frac{\partial\nu_i}{\partial T}\bigg|_{T_0} \ll \nu_i(T_0).$$

Here, according to [9, 15, 16], the excitation and ionization frequencies have the form

$$\nu_* = \nu_*^0 \exp(-U_*/T),$$

$$\nu_i = \nu_{i1}^0 \exp(-U_*/T), \quad T > (2/3)(U_i - U_*), \quad (9)$$

$$\nu_i = \nu_{i2}^0 \exp(-U_i/T), \quad T < (2/3)(U_i - U_*),$$

where $U_*$ and $U_i$ are the excitation and ionization energies of the first atomic level and the temperature $T$ is given in energy units.

When the wave frequency $\omega$ is much higher than the characteristic frequency $\tilde{\nu}$ of the energy transfer due to the presence of an SW in the system, the transfer of energy from electrons to scattering centers can be assumed to be quasi-steady [17]. In this case, the electron temperature perturbation depends on the coordinates and the averaged (over the wave period) squared wave amplitude, $\delta T = \delta T(x, y, |A_1|^2)$. The spatial distribution of the electron temperature perturbation can be determined from the energy balance equation averaged over the wave period:

$$(1/3)\text{Re}(\mathbf{j}\cdot\mathbf{E}^*) = \nabla\cdot\mathbf{Q} - P(T), \quad (10)$$

where $\mathbf{Q}$ is the vector heat flux carried by the electrons, $\mathbf{j}$ is the high-frequency electron current density, and $\mathbf{E}^*$ is the complex-conjugate electric field of the wave. The term $P(T) = -n_0\tilde{\nu}(T_0)(T - T_0)$ describes the energy transferred from electrons to scattering centers in a unit volume with the characteristic frequency

$$\tilde{\nu}(T_0) = \gamma\nu_{col}(T_0) + U_*\frac{\partial\nu_*}{\partial T}\bigg|_{T_0} + U_i\frac{\partial\nu_i}{\partial T}\bigg|_{T_0}, \quad (11)$$

where $n_0$ is the unperturbed plasma density and the quantity $\gamma = 2m_e M/(m_e + M)^2$ is the fraction of energy transferred in elastic collisions from electrons to scattering centers of masses $M$. It should be noted that, in the general case, the characteristic frequency $\tilde{\nu}$ is determined both by the elastic collision frequencies and by the excitation and ionization frequencies of the neutral gas particles. The contribution of these processes to energy transfer essentially depends on the plasma pressure. Thus, at high pressures, the main energy-loss mechanism is due to elastic collisions, whereas at low

pressures, it is due to inelastic collisions, which result in the excitation and ionization of the working-gas particles.

The left-hand side of energy balance equation (10) describes the dissipative heating of plasma electrons in the SW field. The terms on the right-hand side of the equation account for electron energy losses in a unit volume due to the finite plasma conductivity and energy transfer to the scattering centers. The vector heat flux $\mathbf{Q}$ in Eq. (10) is given by the expression $\mathbf{Q} = -\chi\nabla T$, where $\chi$ is the thermal conductivity of the plasma electrons. With this expression, Eq. (10) becomes

$$-\frac{1}{\lambda_T^2}\left(\frac{\partial^2}{\partial x^2} + \frac{\partial^2}{\partial y^2}\right)\frac{\delta T}{T_0} + \frac{\delta T}{T_0} = \left(\frac{\delta T}{T_0}\right)_{loc}. \quad (12)$$

Here, $\lambda_T^{-1} = (\sqrt{3m_e\nu\tilde{\nu}/(5T_0)})^{-1}$ is the characteristic scale on which the electron thermal conductivity varies [17, 18] and the quantity

$$(\delta T/T_0)_{loc} = -e\,\text{Re}(\mathbf{V}_e\cdot\mathbf{E}^*)/(3\tilde{\nu}T_0) \quad (13)$$

describes the relative change in the electron temperature under local heating conditions such that $|\nabla\cdot\mathbf{Q}| \ll |P(T)|$. Assuming that the wave propagates in the positive direction along the $y$ axis and taking into account expressions (2), (6), and (7), which are obtained using linear theory, we can rewrite expression (13) as

$$\left(\frac{\delta T}{T_0}\right)_{loc} = \frac{2}{3}\mu^2\frac{\omega}{\tilde{\nu}}e^{-2k_2''|y|}\left\{2\frac{\nu}{\omega}\varepsilon_0\frac{\omega^2}{\omega_{pe}^2}e^{-2\lambda_2'x}\right.$$

$$+\left[\sin(\lambda_1'' - \lambda_2'')x - 2\frac{\nu}{\omega}\varepsilon_0\frac{\omega^2}{\omega_{pe}^2}\cos(\lambda_1'' - \lambda_2'')x\right] \quad (14)$$

$$\left.\times e^{-(\lambda_1' + \lambda_2')x}\right\},$$

where the parameter $\mu = e|A_1|/(m_e V_{Te}^2)$ characterizes the ratio of the energy of an electron in the wave field to its thermal energy. The spatial temperature distribution of the plasma electrons under local heating conditions [see expression (13) for $(\delta T/T_0)_{loc}$] is shown in Fig. 1. It should be noted that a corresponding approach is used in many studies (see, e.g., [2, 9, 12, 13, 19–21]). However, under the above assumptions that the frequencies $\nu$ and $\tilde{\nu}$ are low, this approach fails to hold because the local heating conditions can be reduced to the inequality $\omega_{pe}^2/(\nu\tilde{\nu}) \ll 1$. Consequently, in the problem in question, the electron heating is essentially nonlocal and the quantity $(\delta T/T_0)_{loc}$ characterizes merely the spatial distribution of the SW power transferred to the electrons in the wave field due to their collisions with scattering centers.
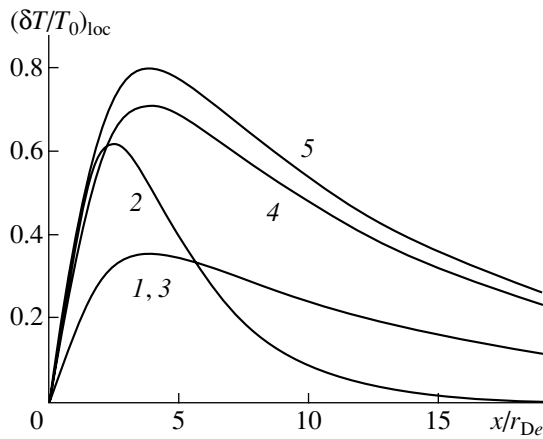
**Fig. 1.** Spatial profiles of the perturbed electron temperature under local heating conditions for the following values of the parameters $\sqrt{\varepsilon_0}\omega/\omega_{pe}$, $\nu/\omega$, $\nu/\tilde{\nu}$, and $\mu$: (*1*) 0.2, 0.1, $10^3$, and 0.1; (*2*) 0.4, 0.05, $10^3$, and 0.1; (*3*) 0.2, 0.2, $10^3$, and 0.1; (*4*) 0.2, 0.1, $2 \times 10^3$, and 0.1; and (*5*) 0.2, 0.1, $10^3$, and 0.15.
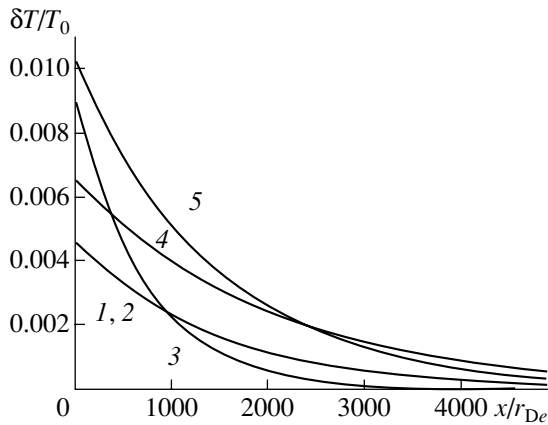


**Fig. 2.** Spatial profiles of the perturbed electron temperature near the source of perturbation for the same parameter values as in Fig. 1.

The spatial distribution of the electron temperature under the conditions of nonlocal heating of the plasma electrons in the SW field should be determined from Eq. (12) with expressions (14). In accordance with the boundary condition implying that the heat flux at the plasma–metal boundary is continuous, and in view of the fact that the thermal conductivity of the metal is much higher than that of the plasma, the heating of the metal is negligible compared to that of the plasma. As for the plasma electron temperature, it should be determined from the following integral form of the law of energy conservation during the heating of plasma electrons: $\int_0^\infty \delta T/T_0 dx = \int_0^\infty (\delta T/T_0)_{\text{loc}} dx$. As a result, the

expression for the relative change in the plasma electron temperature takes the form

$$\frac{\delta T}{T_0} = \frac{2}{3}\mu^2 e^{-2k_2''|y|}\left\{ P_1 e^{-2\lambda_2' x} + P_T e^{-\lambda_T x} \right.$$

(15)

$$\left. + [P_2 \sin(\lambda_1'' - \lambda_2'')x + P_3 \cos(\lambda_1'' - \lambda_2'')x]e^{-(\lambda_1' + \lambda_2')x} \right\},$$

where we have introduced the notation

$$P_1 = -\frac{3}{5}\frac{\nu^2}{\omega^2}, \quad P_2 = -\frac{6}{5}\frac{\nu}{\omega}\frac{\varepsilon_0\omega^2}{\omega_{pe}^2},$$

(16)

$$P_3 = -\frac{24}{5}\frac{\nu^2}{\omega^2}\frac{\varepsilon_0^2\omega^4}{\omega_{pe}^4}, \quad P_T = \sqrt{\frac{6}{5}\frac{\nu}{\tilde{\nu}}}\frac{\nu}{\omega}\frac{\sqrt{\varepsilon_0}\omega}{\omega_{pe}}.$$

An analysis of expression (15) shows that the relative change in the electron temperature reaches its maximum value

$$\left(\frac{\delta T}{T_0}\right)_{\text{max}} \approx \mu^2 \sqrt{\frac{8}{15}\varepsilon_0\frac{\nu}{\tilde{\nu}}}\frac{\nu}{\omega_{pe}}e^{-2k_2''|y|}$$

(17)

at distances from the plasma–metal boundary that are on the order of the electron Debye radius. Consequently, due to the heating of the plasma electrons, there is a heat flux into the plasma interior. Of course, there also exists a heat flux from the plasma to the grounded metal surface. However, in the case under consideration, this flux is negligibly small in compared to that into the plasma interior (Fig. 2).

The condition that the heating be weak, $\delta T \ll T_0$, $|\delta\nu| \ll \nu(T_0)$, yields the following limitation on the wave field amplitude:

$$\mu^2 \sqrt{\frac{8}{15}\varepsilon_0\frac{\nu}{\tilde{\nu}}}\frac{\nu}{\omega_{pe}}\frac{U_{*,i}}{T_0} \ll 1.$$

(18a)

On the other hand, it is also necessary to take into account the fact that the results of linear theory that are used in the present study are valid under the condition

$$\mu \ll 1.$$

(18b)

The results of the numerical analysis that are presented in Fig. 2 show that condition (18) is well satisfied at field amplitudes such that $\mu \le 0.1$.

As was expected, an increase in the normalized wave amplitude $\mu$ and normalized electron collision frequency $\nu/\omega$ leads to an increase in the Joule loss power and, thus, has a significant impact on the electron heating process. An increase in the parameter $\nu/\tilde{\nu}$ leads to an increase in the characteristic scale on which the electron thermal conductivity varies ($\lambda_T^{-1} \propto \sqrt{\nu/\tilde{\nu}}$), and to a more gradual decrease in the electron temperature toward the plasma interior (Fig. 2, curve *4*).

## 5. NONLINEAR DISPERSION RELATION

Recall that a change in the plasma electron temperature produces a corresponding correction $\delta\nu$ in the collision frequency [see formulas (8)]. We take into account this correction and the correction $\delta p = n_0 \delta T$ to the plasma electron pressure in the equation of electron motion

$$\frac{\partial \mathbf{V}_e}{\partial t} = \frac{e}{m_e}\nabla\Psi - \frac{\nabla[p(T_0) + \delta p]}{n_0 m_e} - [\nu(T_0) + \delta\nu]\mathbf{V}_e. \quad (19)$$

We then solve this equation simultaneously with the electron continuity equation and Poisson's equation to obtain the following equation for the wave potential:

$$r_{De}^2\left\{\frac{\partial^4\Psi}{\partial x^4} + \frac{\partial^2\Psi}{\partial x^2}\left[\frac{\omega\omega'}{V_{Te}^2}\left(1 - \frac{\omega_{pe}^2}{\varepsilon_0\omega\omega'}\right) - 2k_2^2\right]\right.$$
$$\left. + k_2^2\Psi\left[k_2^2 - \frac{\omega\omega'}{V_{Te}^2}\left(1 - \frac{\omega_{pe}^2}{\varepsilon_0\omega\omega'}\right)\right]\right\} = R_{\delta\nu} + R_{\delta p}. \quad (20)$$

Equation (20) with zero on the right-hand side is the equation for the SW potential to first order in the wave field amplitude [see Eq. (1)]. The right-hand side of Eq. (20) accounts for nonlinear effects due to the electron heating in the SW field:

$$R_{\delta\nu} = i\frac{2}{5}\left(1 + i\frac{\nu}{\omega}\right)^2\mu^2 A_1\frac{\nu}{\omega\omega}\frac{T}{\partial T}\frac{\partial\nu}{\partial T}\bigg|_{T_0}$$

$$\times\varepsilon_0\frac{\omega_{pe}^2}{V_{Te}^2}\frac{\omega^4}{\omega_{pe}^4}e^{-2k_2''|y|}\left\{-2\frac{\nu}{\omega}\left(1 - i\frac{\nu}{\omega}\right)e^{-(2\lambda_2' + \lambda_2)x}\right.$$

$$- \left[2\sin(\lambda_1'' - \lambda_2'')x - \frac{\nu}{\omega}\frac{\omega_{pe}^2}{\varepsilon_0\omega^2}\right]e^{-(\lambda_1 + 2\lambda_2')x}$$

$$+ \left[4\sin(\lambda_1'' - \lambda_2'')x + 19\frac{\nu}{\omega}\varepsilon_0\frac{\omega^2}{\omega_{pe}^2}\cos(\lambda_1'' - \lambda_2'')x\right] \quad (20a)$$

$$\times e^{-(\lambda_1' + \lambda_2' + \lambda_1)x} - \frac{\nu}{\omega}\frac{\omega_{pe}^2}{\varepsilon_0\omega^2}e^{-(\lambda_1 + \lambda_T)x}$$

$$+ 2\frac{\nu}{\omega}\frac{\lambda_2}{\lambda_T}\left[-2i\frac{\nu}{\omega}\left(1 - i\frac{\nu}{\omega}\right) + \frac{\omega_{pe}^2}{\sqrt{\varepsilon_0}\omega^2}\lambda_T r_{De}\right]e^{-(\lambda_2 + \lambda_T)x}\bigg\},$$

$$R_{\delta p} = \frac{2}{5}\mu^2 A_1\frac{\nu}{\omega}\frac{\omega_{pe}^2}{V_{Te}^2}\frac{\omega^2}{\omega_{pe}^2}e^{-2k_2''|y|}\left\{\frac{\nu}{\omega}\frac{\omega_{pe}^2}{\varepsilon_0\omega^2}e^{-(\lambda_1 + 2\lambda_2')x}\right.$$

$$+ \left[4\sin(\lambda_1'' - \lambda_2'')x + 19\frac{\nu}{\omega}\varepsilon_0\frac{\omega^2}{\omega_{pe}^2}\cos(\lambda_1'' - \lambda_2'')x\right] \quad (20b)$$

$$\times e^{-(\lambda_1' + \lambda_2' + \lambda_1)x} - 2\frac{\nu}{\omega}\frac{\lambda_2}{\lambda_T}\frac{\omega_{pe}^2}{\varepsilon_0\omega^2}e^{-(\lambda_1 + \lambda_T)x}\bigg\}.$$

Taking into account these expressions for $R_{\delta\nu}$ and $R_{\delta p}$, we represent the sought solution to Eq. (20) for the SW potential as

$$\Psi = A_1 e^{-\lambda_1 x} + A_2 e^{-\lambda_2 x} + \Psi_{\delta\nu} + \Psi_{\delta p}. \quad (21)$$

The nonlinear corrections $\Psi_{\delta\nu}$ and $\Psi_{\delta p}$ in representation (21) are related to the perturbations of the collision frequency and electron pressure and are described by the expressions

$$\Psi_{\delta\nu} = i\frac{1}{5}\left(1 + i\frac{\nu}{\omega}\right)^2\mu^2 A_1\frac{\nu}{\omega\omega}\frac{T}{\partial T}\frac{\partial\nu}{\partial T}\bigg|_{T_0}$$

$$\times\varepsilon_0^2\frac{\omega^4}{\omega_{pe}^4}e^{-2k_2''|y|}\left\{\frac{1}{2}\frac{\nu}{\omega}\frac{\omega_{pe}^4}{\varepsilon_0^2\omega^4}\left(1 - i\frac{\nu}{\omega}\right)e^{-(2\lambda_2' + \lambda_2)x}\right.$$

$$- \frac{1}{2}\frac{\omega_{pe}^2}{\varepsilon_0\omega^2}\left[2\sin(\lambda_1'' - \lambda_2'')x - \frac{\nu}{\omega}\frac{\omega_{pe}^2}{\varepsilon_0\omega^2}\right]e^{-(\lambda_1 + 2\lambda_2')x}$$

$$+ \frac{1}{6}\left[4\sin(\lambda_1'' - \lambda_2'')x + 19\frac{\nu}{\omega}\varepsilon_0\frac{\omega^2}{\omega_{pe}^2}\cos(\lambda_1'' - \lambda_2'')x\right] \quad (22a)$$

$$\times e^{-(\lambda_1' + \lambda_2' + \lambda_1)x} - 2\frac{\nu}{\omega}\frac{\omega_{pe}^2}{\varepsilon_0\omega^2}\frac{\lambda_1\lambda_2}{\lambda_T\lambda_T}e^{-(\lambda_1 + \lambda_T)x}$$

$$+ 2\frac{\nu}{\omega}\frac{\omega_{pe}^2}{\varepsilon_0\omega^2}\frac{\lambda_1\lambda_2}{\lambda_T\lambda_T}\left[2i\frac{\nu}{\omega}\left(1 - i\frac{\nu}{\omega}\right) - \frac{\omega_{pe}^2}{\sqrt{\varepsilon_0}\omega^2}\lambda_T r_{De}\right]$$

$$\times e^{-(\lambda_2 + \lambda_T)x}\bigg\},$$

$$\Psi_{\delta p} = \frac{1}{5}\mu^2 A_1\frac{\nu}{\omega}\varepsilon_0\frac{\omega^2}{\omega_{pe}^2}e^{-2k_2''|y|}\left\{\frac{1}{2}\frac{\nu}{\omega}\frac{\omega_{pe}^4}{\varepsilon_0^2\omega^4}e^{-(\lambda_1 + 2\lambda_2')x}\right.$$

$$+ \frac{1}{6}\left[4\sin(\lambda_1'' - \lambda_2'')x + 19\frac{\nu}{\omega}\varepsilon_0\frac{\omega^2}{\omega_{pe}^2}\cos(\lambda_1'' - \lambda_2'')x\right] \quad (22b)$$

$$\times e^{-(\lambda_1' + \lambda_2' + \lambda_1)x} - 2\frac{\nu}{\omega}\frac{\omega_{pe}^2}{\varepsilon_0\omega^2}\frac{\lambda_1\lambda_2}{\lambda_T\lambda_T}e^{-(\lambda_1 + \lambda_T)x}\bigg\}.$$

We use the boundary conditions implying that the wave potential and the normal component of the elec-

Re $S_{\delta\nu}/(\partial\nu/\partial T\, T/\nu)$



Im $S_{\delta\nu}/(\partial\nu/\partial T\, T/\nu)$



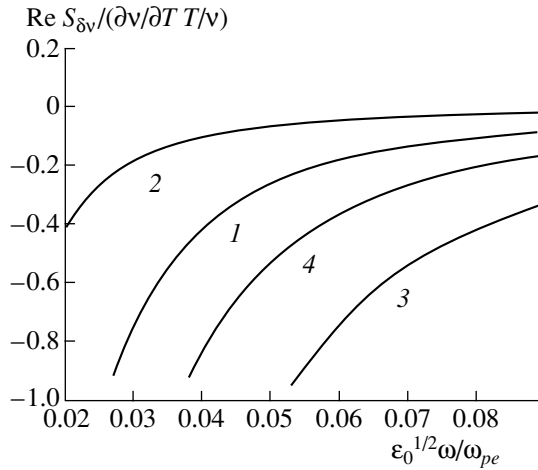**Fig. 3.** Dependence of the real part of the coefficient $S_{\delta\nu}$ on the wave frequency for the following values of the parameters $\nu/\omega_{pe}$, $\nu/\tilde{\nu}$, and $\mu$: (*1*) 0.01, $10^3$, and 0.1; (*2*) 0.01, $10^3$, and 0.05; (*3*) 0.02, $10^3$, and 0.1; and (*4*) 0.01, $2\times10^3$, and 0.1.
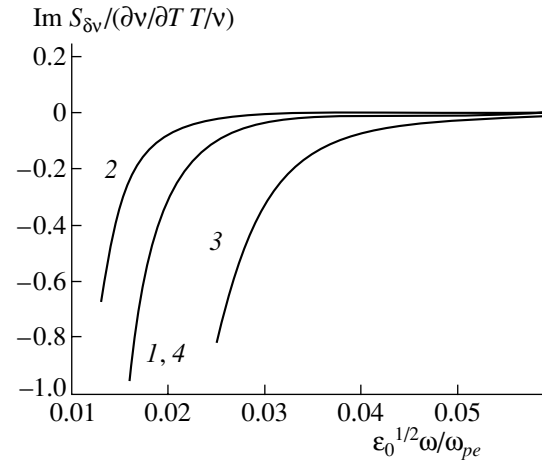
**Fig. 4.** Dependence of the imaginary part of the coefficient $S_{\delta\nu}$ on the wave frequency for the same parameter values as in Fig. 3.

tron velocity vanish at the plasma–metal boundary. As a result, we obtain the nonlinear dispersion relation

$$1 + k_2^2 r_{\mathrm{D}e}^2 - r_{\mathrm{D}e}^2(\lambda_1^2 + \lambda_1\lambda_2 + \lambda_2^2)$$
$$= -\frac{\varepsilon_0\omega^2}{\omega_{pe}^2}\left(1 + i\frac{\nu}{\omega}\right)(S_{\delta\nu} + S_{\delta p}), \tag{23}$$

where

$$S_{\delta p} = \frac{4}{5}\mu^2\frac{\nu^2}{\omega^2}\left(1 - i\frac{\nu}{\omega}\right)e^{-2k_2''|y|},$$
$$S_{\delta\nu} = -i\frac{1}{5}\mu^2\frac{T_0}{\nu}\frac{\partial\nu}{\partial T}\bigg|_{T_0}\frac{\nu^3}{\omega^3}\frac{\omega_{pe}^2}{\varepsilon_0\omega^2}\left\{\frac{1}{2} - i\frac{10}{3}\frac{\varepsilon_0\omega^3}{\omega_{pe}^2\tilde{\nu}}\right\}e^{-2k_2''|y|}. \tag{24}$$

The complex wavenumber $k_2$ satisfying this dispersion relation has the form

$$k_2 = \frac{\omega}{V_{Te}}\frac{\sqrt{\varepsilon_0}\omega}{\omega_{pe}}\left(1 + i\frac{\nu}{\omega}\right)(1 + S_{\delta\nu} + S_{\delta p}). \tag{25}$$

In the limit $|A_1| \longrightarrow 0$, nonlinear dispersion relation (23) and its solution (25) transform into linear dispersion relation (4) and linear solution (6), respectively.

## 6. RESULTS AND DISCUSSIONS

According to expressions (24) and solution (25), a change in the electron pressure produces a positive nonlinear shift of the real part of the wavenumber ($\mathrm{Re}\,S_{\delta p} > 0$) and reduces the damping rate of the SW ($\mathrm{Im}\,S_{\delta p} < 0$). In

this case, the nonlinear correction to the real part of the wavenumber exceeds that to the imaginary part:

$$|\mathrm{Re}\,S_{\delta p}|/|\mathrm{Im}\,S_{\delta p}| = \frac{\omega}{\nu} \gg 1. \tag{26}$$

From expressions (24), we see that the effect of a change in the electron collision frequency on the SW dispersion is governed by the dependence of the collision frequency on the electron temperature. First, we consider the case in which the electron collision frequency increases with temperature, $\partial\nu/\partial T|_{T_0} > 0$. This takes place, e.g., in a semiconductor plasma in which the electrons are scattered by optical and acoustic phonons, $\nu(T) \propto \sqrt{T}$, $T^{3/2}$ [12–14], or in a low-pressure gas-discharge plasma in which the electron collision frequency is determined by inelastic collisions, which result in the ionization and excitation of the working-gas particles [see expressions (9)]. In this situation, the nonlinear shift of the real part of the wavenumber $k_2$ is negative ($\mathrm{Re}\,S_{\delta\nu} < 0$, see Fig. 3) and the nonlinear damping rate (25) is lower ($\mathrm{Im}\,S_{\delta\nu} < 0$, see Fig. 4) than its linear value (6).

In the case in which the electron collision frequency decreases as the electron temperature increases, $\partial\nu/\partial T|_{T_0} < 0$ (as is the case, e.g., with elastic collisions of electrons with ions or impurities in a gaseous plasma, $\nu(T) \propto T^{-3/2}$, $T^{-1/2}$ [14]), the situation is opposite: the shift of the real part of the wavenumber is positive and the damping rate of the wave is higher than its linear value. In this case, in contrast to relationships (26), the nonlinear corrections to the real and imaginary parts of the wavenumber that are introduced by the per-

turbation of the electron collision frequency can be of the same order of magnitude:

$$\left| \operatorname{Re} S_{\delta\nu} \right| / \left| \operatorname{Im} S_{\delta\nu} \right| \; = \; \frac{5}{3} \frac{\varepsilon_0 \omega^3}{\omega_{pe}^2 \tilde{\nu}}. \qquad (27)$$

A comparison between the effects produced by the perturbation of the electron collision frequency and by the change in the electron pressure on the self-interaction of an SW shows that the latter is of minor importance; thus, the contribution from the nonlinear corrections decreases with the wave frequency (Figs. 3, 4).

We note that the nonlinear corrections to the imaginary part of the wavenumber are also determined by the mechanism for electron energy losses, $\operatorname{Re} S_{\delta\nu} \propto \nu/\tilde{\nu}$. Thus, in a semiconductor plasma or a high-pressure gas-discharge plasma, the dominant energy-loss mechanism is by elastic electron collisions [17]. In this case, the ratio of the collision frequency $\nu$ to the characteristic frequency of energy transfer, $\tilde{\nu}$, is described by the expression

$$\nu/\tilde{\nu} \; = \; 0.5 M/m_e \gg 1. \qquad (28)$$

As the electron pressure decreases, the loss mechanism involving inelastic electron collisions [16, 17] that excite the neutral gas particles becomes dominant and this ratio decreases:

$$\nu/\tilde{\nu} \; = \; (1 + \nu_{\text{col}}/\nu_*) T_0^2/U_*^2 \ll 0.5 M/m_e. \qquad (29)$$

Hence, an analysis of relationships (28) and (29) allows us to conclude that, for a high-pressure plasma, the nonlinear corrections to the real part of the wavenumber that are introduced by the electron heating in the SW field are the most important.

Let us compare the efficiencies of the thermal and ponderomotive mechanisms for the self-interaction of an SW. It is well known that the ponderomotive nonlinearity results in plasma density perturbations, $\delta n/n_0 \cong -\mu^2 e^{-2k_2''|y|}$, in the region where the wave energy density is the highest. In Eq. (25), this density perturbation can be taken into account by the term $S_{\delta n} = (\delta k_2/k)_{\text{st}} \cong 0.5\mu^2 e^{-2k_2''|y|}$, which is dominant for a low-pressure plasma:

$$\frac{|S_{\delta n}|}{|S_{\delta\nu}|} \cong \left( \frac{T_0}{\nu} \frac{\partial \nu}{\partial T} \Big|_{T_0} \right)^{-1} \frac{\omega^2 \tilde{\nu}}{\nu^3}. \qquad (30)$$

Hence, the thermal nonlinearity plays a governing role at sufficiently high plasma pressures, such that the condition $\omega/\nu \ll \sqrt{\nu/\tilde{\nu}}$ is satisfied.

## 7. CONCLUSIONS

We have investigated the effect of electron heating on the self-interaction of a weakly nonlinear potential SW propagating along a plasma–metal interface.

We have obtained the spatial distribution of the electron temperature in a dense plasma ($\omega^2 \ll \omega_{pe}^2/\varepsilon_0$) in the weak heating approximation such that the perturbation of the electron temperature in the wave field is small compared to the unperturbed electron temperature. We have shown that, in this case, the electron heating is essentially nonlocal and the electron temperature is determined predominantly by heat transport processes in the plasma.

We have derived and investigated the nonlinear dispersion relation for an SW under nonlocal heating conditions. We have also obtained analytic expressions for the nonlinear shift of the wavenumber and for the spatial damping rate of an SW.

We have shown that the self-interaction of an SW due to the thermal nonlinearity is governed by the dependence of the electron collision frequency on temperature and that, at sufficiently high plasma pressures, the effect of the self-interaction is greatest.

The results obtained are applicable to both semiconductor and gaseous plasmas.

## ACKNOWLEDGMENTS

## REFERENCES

1. M. Moisan, J. Hurbert, J. Margot, and Z. Zakrzewski, *Advanced Technologies Based on Wave and Beam Generated Plasmas* (Kluwer, Amsterdam, 1999).
2. N. A. Azarenkov and K. N. Ostrikov, Phys. Rep. **308**, 333 (1999).
3. N. A. Azarenkov, Zh. Tekh. Fiz. **57**, 1165 (1987) [Sov. Phys. Tech. Phys. **32**, 681 (1987)].
4. A. V. Gurevich and A. B. Shvartsburg, *Nonlinear Theory of Radiowave Propagation in Ionosphere* (Nauka, Moscow, 1973).
5. V. N. Karpman, *Nonlinear Waves in Dispersive Media* (Nauka, Moscow, 1973; Pergamon, Oxford, 1975).
6. J. Weiland and H. Wilhelmsson, *Coherent Nonlinear Interaction of Waves in Plasmas* (Pergamon, Oxford, 1976; Énergoizdat, Moscow, 1981).
7. A. N. Kondratenko, *Plasma Waveguides* (Atomizdat, Moscow, 1976).
8. N. A. Azarenkov, Yu. A. Akimov, and A. V. Gapon, Vestn. Kharkovsk. Nats. Univ., Ser.: Yadra, Chastitsy, Polya **12** (496), 29 (2000).
9. Yu. M. Aliev, A. G. Boev, and A. Shivarova, J. Phys. D **17**, 2233 (1984).
10. N. A. Azarenkov, K. N. Ostrikov, and M. Y. Yu, J. Appl. Phys. **84**, 4176 (1998).

11. A. G. Litvak and V. A. Mironov, *Thermal Nonlinear Phenomena in Plasmas* (Inst. of Applied Physics, USSR Acad. Sci., Gorki, 1979).

12. F. G. Bass and Yu. G. Gurevich, *Hot Electrons and High-Power Electromagnetic Waves in Semiconductors and Gas-Discharge Plasmas* (Nauka, Moscow, 1975).

13. F. G. Bass and Yu. G. Gurevich, Usp. Fiz. Nauk **103**, 447 (1971) [Sov. Phys. Usp. **14**, 113 (1971)].

14. N. N. Beletskiĭ, V. M. Svetlichnyĭ, D. D. Khalameĭda, and V. M. Yakovenko, *Microwave Electromagnetic Phenomena in Inhomogeneous Semiconductors* (Naukova Dumka, Kiev, 1991).

15. Yu. M. Aliev, K. Ivanova, M. Moisan, and A. Shivarova, Plasma Sources Sci. Technol. **2**, 145 (1993).

16. L. M. Biberman, V. S. Vorob'ev, and I. T. Yakubov, *Kinetics of Nonequilibrium Low-Temperature Plasma* (Nauka, Moscow, 1982; Consultants Bureau, New York, 1987).

17. V. E. Golant, A. P. Zhilinsky, and S. A. Sakharov, *Fundamentals of Plasma Physics* (Atomizdat, Moscow, 1977; Wiley, New York, 1980).

18. Yu. M. Aliev, H. Schluter, and A. Shivarova, Plasma Sources Sci. Technol. **5**, 514 (1996).

19. Yu. M. Aliev, A. V. Maximov, and H. Schluter, Phys. Scr. **48**, 464 (1993).

20. Yu. M. Aliev, A. V. Maximov, I. Ghanashev, *et al.*, IEEE Trans. Plasma Sci. **23**, 409 (1995).

21. Yu. M. Aliev, V. Yu. Bychenkov, A. V. Maximov, and H. Schluter, Plasma Sources Sci. Technol. **1**, 126 (1992).

*Translated by I.A. Kalabalyk*

# Coronal Oscillations and Internal Loop Structure

## A. A. Solov'ev*, B. B. Mikhalyaev**, and E. A. Kirichek**

*\*Pulkovo Astronomical Observatory, Russian Academy of Sciences,*
*Pulkovskoe shosse 65/1, St. Petersburg, 196140 Russia*
*\*\*Kalmyk State University, Elista, Russia*
Received August 2, 2002; in final form, April 28, 2003

**Abstract**—The transverse oscillations of a coronal magnetic loop whose ends are rigidly fixed in the photosphere are investigated. The loop is assumed to be inhomogeneous and to comprise two internal structural components: a central dense hot filament and a coaxial rarefied shell around it, in which the plasma density is lower than the density of the surrounding coronal plasma. The Alfvén speed in the shell, $V_{Am}$, is higher than that in the central filament and in the corona: $V_{Am} > V_{Ae} > V_{Ai}$. It is shown that, in the perfectly conducting plasma approximation, such a loop can generate two fast magnetosonic waves. The higher velocity wave is emitted in a radial direction, thereby ensuring the effect of the radiative damping of oscillations at the frequency of the $m = 1$ cylindrical mode. The results of calculating the effect of radiative losses show that, for typical loop parameters (corresponding to those of the loops observed in the solar corona), the quality factor of oscillations may be fairly low ($Q \approx 40$). Under the conditions in question, the second (lower velocity) fast magnetosonic wave is not emitted (in contrast to the first) but rather turns out to be trapped in the magnetic flux tube. © 2003 MAIK "Nauka/Interperiodica".

## 1. INTRODUCTION

The oscillations of arch loops that were revealed by the TRACE (Transition Region and Coronal Explorer) spacecraft in the solar corona [1–4] have drawn increased attention to the problem of the propagation and damping of MHD waves in the solar corona and also to the more general problem of heating the coronal plasma to temperatures of about 1 MK. Direct observations by a UV telescope on the TRACE spacecraft made it possible to detect and thoroughly investigate not only the transverse oscillations of long thin coronal loops (such that the transverse displacement of the loop may sometimes be larger than the diameter of its cross section) [1, 2] but also the longitudinal perturbations within the loops (which are presumably of MHD origin) [3, 4]. There is some observational evidence that the internal structure of coronal loops is inhomogeneous: according to [4], the loop may consist of a filament and a coaxial shell or may be composed of individual filaments with different temperatures.

One of the main difficulties in a theoretical analysis of the oscillatory properties of coronal loops by means of a linearized set of MHD equations is the following [5–10]: The internal structure of a coronal loop is usually described using the model of a homogeneous magnetic flux tube in the form of a circular cylinder, on the inside and outside of which the plasma density and magnetic induction are uniform and their values, as well as the values of the gas pressure, are different but are consistent with the condition of equilibrium in the radial direction. In a thin tube approximation such that the tube radius is much smaller than the wavelength, the dispersion relation for transverse oscillations of the

loop at the frequencies of cylindrical modes with $m \geq 1$ has the form

$$\rho_{0i}(\omega^2 - V_{Ai}^2 k_z^2) = -\rho_{0e}(\omega^2 - V_{Ae}^2 k_z^2). \qquad (1)$$

Here, $\rho_{0i}$ and $\rho_{0e}$ are the unperturbed values of the plasma density on the inside and outside of the tube, $V_{Ai}$ and $V_{Ae}$ are the corresponding values of the Alfvén speed, and $k_z$ is the wavenumber along the tube (the longitudinal wavenumber). Since, for coronal tubes, the inequality $V_{Ai} < V_{Ae}$ (or, equivalently, $\rho_{0i} > \rho_{0e}$) is obviously satisfied, it follows from dispersion relation (1) that the phase velocity of the oscillations should be lower than the Alfvén speed on the outside of the tube, $\omega/k_z < V_{Ae}$. Under this condition, the radial wavenumber of the wave on the outside is purely imaginary [see expression (8) below]; consequently, the wave cannot propagate in the radial direction in the space surrounding the tube, or, in other words, it cannot be emitted. The transverse wave satisfying dispersion relation (1) is a fast magnetosonic (FMS) wave; the wave at the frequency of the $m = 0$ mode is a slow magnetosonic wave, which also can propagate only along the tube.

Hence, a thin coronal loop modeled by a homogeneous magnetic flux tube is merely a waveguide that does not emit MHD waves into the surrounding space. This circumstance has given new impetus to the search for other mechanisms for the damping of oscillations, specifically, those that are not associated with the emission of wave energy (e.g., the anomalous plasma viscosity and/or anomalous plasma resistivity [2] and the
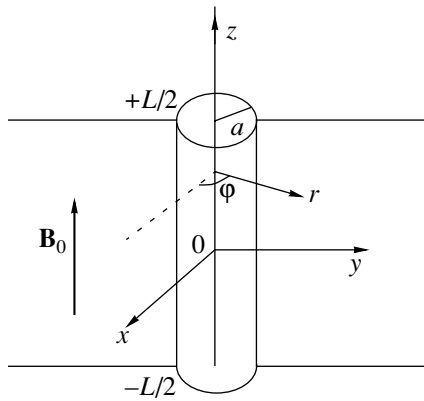
**Fig. 1.** Representation of a coronal loop in the form of a straight circular cylinder with length *L* and cross-sectional radius *a* in the cylindrical and Cartesian coordinate systems.

resonant absorption of MHD waves in a narrow boundary layer of the tube [10]).

In our earlier paper [11], we showed that a magnetized plasma cylinder performing one-dimensional finite-amplitude transverse oscillations in an external uniform magnetic field aligned with it efficiently generates outwardly propagating FMS waves. The energy flux carried away from the surface of an oscillating cylinder by the MHD waves per unit time turns out to be so intense that the energy stored in the cylinder under the action of the initial perturbation that has driven the oscillations is dissipated during a time as short as several periods of free oscillations. In [11], in order to simplify the problem to the ultimate possible extent and to capture the main effect, namely, the radiative damping of oscillations, we considered only the side displacements of a magnetized cylinder with free ends. In the case of such displacements, the perturbed magnetic field has only the longitudinal component and the oscillations of the cylinder are dissipationless: $k = \omega/V_{SA}$, where $V_{SA} = (C_S^2 + V_A^2)^{1/2}$, with $C_S$ being the speed of sound. Also, in [11], we did not solve MHD equations inside the cylinder.

In the present paper, we consider the oscillatory properties of a coronal magnetic loop containing two structural components: a central filament and a surrounding cylindrical shell. Below, we will show that, under certain conditions, such a loop is capable of emitting MHD waves. For this to occur, it is necessary that the central part (filament) of the loop be surrounded by a coaxial cylindrical shell in which the Alfvén speed $V_{Am}$ is higher than those in the filament and in the environment:

$$V_{Am} > V_{Ae} > V_{Ai}. \tag{2}$$

Here and below, the subscripts $i$, $m$, and $e$ refer, respectively, to the internal region (the filament), the intermediate region (the shell), and the external region (the surrounding coronal plasma). Since the magnetic induction in the filament differs insignificantly from that in the shell, the above condition implies that the plasma density in the shell should be lower than the density of the surrounding medium. We thus are dealing with a model in which the central (denser and hotter) part of the loop is surrounded by a rarefied shell. As will be shown below, such a loop (tube) is capable of generating two FMS waves at the frequency of the $m = 1$ cylindrical mode. One of these waves is emitted into the surrounding space, while the other propagates within the tube, never leaves it, and thus appears to be trapped by it. The latter effect is of great interest for the problem of heating coronal loops. It should be noted that, under certain conditions, this second wave can also be emitted into space; however, under the conditions adopted in our study, it always remains within the tube.

Our paper is organized as follows: In Section 2, we present the model of a coronal loop in the form of a filament surrounded by a shell and write out the solutions to a linearized set of MHD equations for three regions: the internal region (the filament), the intermediate region (the shell), and the external region (the surrounding coronal plasma). In Section 3, we derive the dispersion relation and describe oscillations at the frequency of the first ($m = 1$) cylindrical mode. In Section 4, we calculate the damping rate of the oscillations. And finally, in Section 5, we discuss the results obtained.

## 2. SOLUTION OF LINEARIZED MHD EQUATIONS

We will work in the cylindrical ($r$, $\varphi$, $z$) and Cartesian ($x$, $y$, $z$) coordinate systems (Fig. 1). In the region $-L/2 < z < +L/2$, we consider a straight magnetic flux tube with length $L$ and cross-sectional radius $a$, whose ends are fixed at the planes $z = +L/2$ and $z = -L/2$. Since the loops observed in the solar corona are thin ($L \gg a$) and are curved only slightly, this geometric model of a loop in the form of a straight magnetic flux tube of finite length provides a fairly adequate description of the actual loop structure.

We consider a loop with nonuniform radial profiles of the plasma density and magnetic induction and approximate the profiles by step functions like that shown in Fig. 2. In this model of the loop, there are three different regions in the radial direction: the internal region $r < b$, the intermediate region $b < r < a$, and the external region $r > a$. The internal region is the central part of the loop (a filament with an elevated plasma density), the external region is the space surrounding the loop, and the intermediate region is a rarefied shell. In each of these three regions, the unperturbed magnetic field is uniform, the only nonzero component of the magnetic induction being the $z$ component. In an unperturbed state, the transverse equilibrium condition has the form

$$p_{0i} + \frac{B_{0i}^2}{8\pi} \;=\; p_{0m} + \frac{B_{0m}^2}{8\pi} \;=\; p_{0e} + \frac{B_{0e}^2}{8\pi}. \qquad (3)$$

Let the loop be displaced from its equilibrium position only in the $x$ direction, the displacement amplitude being $X_0$. We describe the displacement by the formula

$$X \;=\; X_0 \cos(k_z z) e^{-i\omega t}, \qquad (4)$$

where $k_z = n\pi/L$ with $n = 0, 1, 2, \ldots$. The value $n = 0$ corresponds to the transverse displacements of a loop as a whole, i.e., to transverse oscillations of a loop with free ends. The oscillations of a loop with fixed ends are described by odd values of $n$. The value $n = 1$ corresponds to the half-wave transverse oscillations of a loop; it is this oscillation mode that was detected by the TRACE UV telescope. The values $n \gg 1$ correspond to short-wavelength perturbations.

We assume that the coronal loop executes small oscillations that can be described in a linear approximation. The linearized set of ideal MHD equations has the form

$$\rho_0 \frac{\partial \mathbf{v}}{\partial t} \;=\; -\nabla p + \frac{1}{4\pi}(\nabla \times \mathbf{B}) \times \mathbf{B}_0,$$

$$\frac{\partial p}{\partial t} + \gamma p_0 \nabla \cdot \mathbf{v} \;=\; 0, \qquad (5)$$

$$\frac{\partial \mathbf{B}}{\partial t} \;=\; \nabla \times (\mathbf{v} \times \mathbf{B}_0),$$

where $\mathbf{B}_0$ and $\rho_0$ are the unperturbed magnetic induction and unperturbed plasma density and $\mathbf{B}$, $\rho$, and $\mathbf{v}$ are perturbations of the induction, density, and velocity, respectively. In accordance with the geometry of the perturbation under analysis, we seek a solution to Eqs. (5) in the form of a superposition of cylindrical modes. In what follows, we will describe the perturbations of the radial velocity component, pressure, and longitudinal magnetic induction by functions of the form of $f(\mathbf{r}, t) = f(r)\cos\varphi\cos(k_z z)\exp(-i\omega t)$.

From Eqs. (5) we obtain the following equations for the radial component of the perturbed velocity, $v_r(r)$, and the perturbed total pressure $P(r) = p(r) + B_0 B_z(r)/4\pi$:

$$v_r \;=\; -\frac{i\omega}{(\omega^2 - V_A^2 k_z^2)\rho_0} \frac{dP}{dr},$$

$$(\omega^2 - C_S^2 k_z^2)P \;=\; (\omega^2(V_A^2 + C_S^2) - C_S^2 V_A^2 k_z^2) \qquad (6)$$

$$\times \left( \frac{1}{i\omega r} \frac{d}{dr} r v_r + \frac{1}{\omega^2 - V_A^2 k_z^2} \frac{P}{r^2} \right).$$

In turn, from Eqs. (6) we see that the perturbed total pressure $P$ satisfies the Bessel equation

$$r^2 \frac{d^2 P}{dr^2} + r\frac{dP}{dr} + (k^2 r^2 - 1)P \;=\; 0, \qquad (7)$$
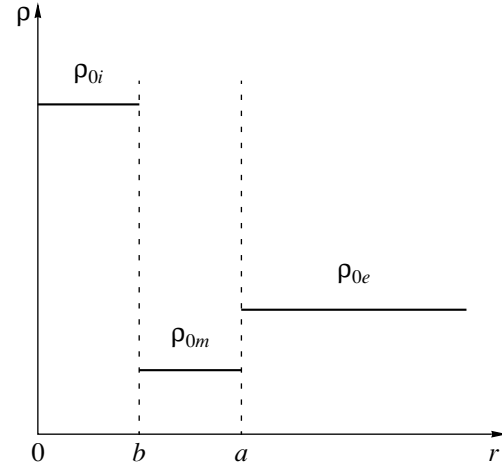
**Fig. 2.** Model step profile of the plasma density in a coronal loop containing two structural components: $b$ is the radius of the central part (filament) of a loop with an elevated plasma density, and $a$ is the radius of a shell with a reduced density.

where we have introduced the notation

$$k^2 \;=\; \frac{(\omega^2 - V_A^2 k_z^2)(\omega^2 - C_S^2 k_z^2)}{(C_S^2 + V_A^2)(\omega^2 - C_T^2 k_z^2)},$$

$$C_T^2 \;=\; \frac{C_S^2 V_A^2}{C_S^2 + V_A^2}. \qquad (8)$$

In each of the above three spatial regions, the perturbed total pressure $P$ satisfies the same equation (7) and, accordingly, expression (8) for the radial wavenumber takes the same form but with different values of the sound and Alfvén speeds. In what follows, we will denote the radial wavenumber $k$ in the three regions by the corresponding subscripts: $k_i$, $k_m$, and $k_e$. The values of the parameter $k_z$ in the regions are chosen to be the same in order to satisfy the condition for the global solution to be continuous.

Let us write out the solutions for each of the three regions. The solution for the internal region (filament) is expressed through the Bessel function that has no singularity at the loop axis ($r = 0$):

$$v_{ri}(r) \;=\; -i\omega X_{0i} \frac{J_1'(k_i r)}{J_1'(k_i b)},$$

$$P_i(r) \;=\; X_{0i} \frac{\rho_{0i}(\omega^2 - V_{Ai}^2 k_z^2)}{k_i} \frac{J_1(k_i r)}{J_1'(k_i b)}, \qquad (9)$$

where $X_{0i}$ is the amplitude of the radial oscillations within the filament.

A distinctive feature of the solution for the intermediate region is the inequality $k_m^2 < 0$ (see Section 3 for details), which implies that the oscillations in the shell

are of the nature of surface waves. The solution in the intermediate region should be expressed in terms of the Hankel and Bessel functions $K_1$ and $I_1$. Since this region neither includes the loop axis nor extends to infinity, we retain both of the arbitrary constants in the general solution to the modified Bessel equation:

$$v_{rm}(r) = -i\omega(AK_1'(l_m r) + CI_1'(l_m r)),$$

$$l_m = \sqrt{-k_m^2}, \qquad (10)$$

$$P_m(r) = \frac{\rho_{0m}(\omega^2 - V_{Am}^2 k_z^2)}{l_m}(AK_1(l_m r) + CI_1(l_m r)).$$

The solution to the problem for the external region is expressed through the Hankel function of the first kind, which describes the waves propagating away from the cylinder to infinity:

$$v_{re}(r) = -i\omega X_{0e}\frac{H_1^{(1)'}(k_e r)}{H_1^{(1)'}(k_e a)},$$

$$P_e(r) = X_{0e}\frac{\rho_{0e}(\omega^2 - V_{Ae}^2 k_z^2)}{k_e}\frac{H_1^{(1)}(k_e r)}{H_1^{(1)'}(k_e a)}. \qquad (11)$$

## 3. OSCILLATION MODES IN A TUBE WITH A SHELL

The relationships between the coefficients $X_{0e}$, $X_{0i}$, $A$, and $C$ can be obtained from the matching conditions, which imply that the radial component of the perturbed velocity, $v_r$, and the perturbed total pressure $P$ are continuous at the boundaries between the three regions. From the boundary conditions for the perturbed radial velocity at the filament surface ($r = b$) and at the outer surface of the shell ($r = a$) we obtain

$$X_{0i} = AK_1'(l_m b) + CI_1'(l_m b), \qquad (12)$$

$$X_{0e} = AK_1'(l_m a) + CI_1'(l_m a). \qquad (13)$$

The corresponding boundary conditions for the perturbed total pressure yield

$$X_{0i}\frac{\rho_{0i}}{k_i}(\omega^2 - V_{Ai}^2 k_z^2)\frac{J_1(k_i b)}{J_1'(k_i b)}$$

$$= \frac{\rho_{0m}}{k_m}(\omega^2 - V_{Am}^2 k_z^2)(AK_1(l_m b) + CI_1(l_m b)), \qquad (14)$$

$$X_{0e}\frac{\rho_{0e}}{k_e}(\omega^2 - V_{Ae}^2 k_z^2)\frac{H_1^{(1)}(k_e a)}{H_1^{(1)'}(k_e a)}$$

$$= \frac{\rho_{0m}}{k_m}(\omega^2 - V_{Am}^2 k_z^2)(AK_1(l_m a) + CI_1(l_m a)). \qquad (15)$$

We thus arrive at the set of four linear equations (12)–(15) for the four coefficients $X_{0e}, X_{0i}, A$, and $C$. An equation stating that the determinant of this set is zero is precisely the sought-for dispersion relation:

$$\frac{\rho_{0i}}{k_i}(\omega^2 - V_{Ai}^2 k_z^2)\frac{\rho_{0e}}{k_e}(\omega^2 - V_{Ae}^2 k_z^2)J_1(k_i b)H_1^{(1)}(k_e a)$$

$$\times[K_1'(l_m b)I_1'(l_m a) - K_1'(l_m a)I_1'(l_m b)]$$

$$+ \frac{\rho_{0i}}{k_i}(\omega^2 - V_{Ai}^2 k_z^2)\frac{\rho_{0m}}{k_m}(\omega^2 - V_{Am}^2 k_z^2)J_1(k_i b)H_1^{(1)'}(k_e a)$$

$$\times[K_1(l_m a)I_1'(l_m b) - K_1'(l_m b)I_1(l_m a)]$$

$$+ \frac{\rho_{0e}}{k_e}(\omega^2 - V_{Ae}^2 k_z^2)\frac{\rho_{0m}}{k_m}(\omega^2 - V_{Am}^2 k_z^2)J_1'(k_i b)H_1^{(1)}(k_e a) \qquad (16)$$

$$\times[K_1'(l_m a)I_1(l_m b) - K_1(l_m b)I_1'(l_m a)]$$

$$+ \frac{\rho_{0m}^2}{k_m^2}(\omega^2 - V_{Am}^2 k_z^2)^2 J_1'(k_i b)H_1^{(1)'}(k_e a)$$

$$\times[K_1(l_m b)I_1(l_m a) - K_1(l_m a)I_1(l_m b)] = 0.$$

In general, Eq. (16) is rather difficult to solve. However, for our purposes here, it is sufficient to consider its solution in a thin tube approximation such that the filament radius $b$ and the shell radius $a$ are small in comparison with the wavelengths of the waves in question. We assume that the inequalities $k_i b \ll 1$, $k_e a \ll 1$, $l_m b \ll 1$, and $l_m a \ll 1$ hold, which allows us to use series expansions for the solutions to the Bessel equation. In each of the expansions, we retain the lowest order term to obtain the zero-order dispersion relation

$$(a^2 - b^2)[\rho_{0m}^2(\omega^2 - V_{Am}^2 k_z^2)^2$$

$$+ \rho_{0i}(\omega^2 - V_{Ai}^2 k_z^2)\rho_{0e}(\omega^2 - V_{Ae}^2 k_z^2)]$$

$$+ (a^2 + b^2)\{\rho_{0m}(\omega^2 - V_{Am}^2 k_z^2) \qquad (17)$$

$$\times[\rho_{0i}(\omega^2 - V_{Ai}^2 k_z^2) + \rho_{0e}(\omega^2 - V_{Ae}^2 k_z^2)]\} = 0.$$

The frequency $\omega$ that satisfies dispersion relation (17) is real and provides a zero-order approximation to the solution of dispersion relation (16). Equation (17) has two solutions corresponding to two different modes of magnetosonic waves. Since Eq. (17) contains Alfvén speeds and does not include sound speeds, both of the modes are FMS ones; the higher velocity mode will be referred to as a fast mode, and the lower velocity mode will be referred to as a slow mode. Dispersion relation (17) is a quadratic equation for the squared phase velocity $v^2 = \omega^2/k_z^2$ and thus is easy to solve, but its solutions are quite lengthy and we will not reproduce them here.

Let us consider the values of the phase velocities in the limits $b \longrightarrow 0$ and $b \longrightarrow a$. In the first case, the lim-

iting velocity of the fast mode is $v^2 \longrightarrow v_{10}^2$ and that of the slow mode is $v^2 \longrightarrow v_{20}^2$, where

$$v_{10}^2 = \frac{(\rho_{0m}V_{Am}^2 + \rho_{0e}V_{Ae}^2)}{\rho_{0m} + \rho_{0e}},$$

$$v_{20}^2 = \frac{(\rho_{0m}V_{Am}^2 + \rho_{0i}V_{Ai}^2)}{\rho_{0m} + \rho_{0i}}.$$

In the second case ($b \longrightarrow a$), the limiting velocities of the fast and slow modes are as follows: $v^2 \longrightarrow v_{1a}^2 = V_{Am}^2$ and $v^2 \longrightarrow v_{2a}^2 = (\rho_{0i}V_{Ai}^2 + \rho_{0e}V_{Ae}^2)/(\rho_{0i} + \rho_{0e})$. Comparing the latter relationship with dispersion relation (1), we can see that a FMS wave with $m = 1$, which is generated in a homogeneous tube, is nothing more than a slow mode in the limit $b \longrightarrow a$.

In order to clarify whether one or another mode can be emitted into the surrounding space, we consider expression (8) for $k_e^2$ in the third (external) region. Using the conditions $V_{Ae} > C_{Se} > C_{Te}$, which are satisfied for the solar corona, we arrive at the inequality $k_e^2 > 0$, which holds for $v > V_{Ae}$. In this case, the wave will propagate in the radial direction or, in other words, it will be emitted into the surrounding space. In order to check the condition $v > V_{Ae}$, we consider the differences

$$v_{10}^2 - V_{Ae}^2 = \frac{\rho_{0m}(V_{Am}^2 - V_{Ae}^2)}{\rho_{0m} + \rho_{0e}},$$

$$v_{20}^2 - V_{Ae}^2 = \frac{(\rho_{0m}(V_{Am}^2 - V_{Ae}^2) - \rho_{0i}(V_{Ae}^2 - V_{Ai}^2))}{\rho_{0m} + \rho_{0i}}. \tag{18}$$

For $0 < b < a$, the phase velocity of the fast mode lies within the range $v_{10} < v < v_{1a} = V_{Am}$. Taking into account conditions (2), we can state that, for all values of the filament and shell radii satisfying the inequalities $0 < b < a$, the fast mode can be emitted. The phase velocity of the slow mode lies within the range $v_{20} > v > v_{2a}$. If we consider transverse equilibrium condition (3) in the solar corona and ignore the gas pressure, then, under the inequality

$$2 - V_{Ae}^2 \left( \frac{1}{V_{Am}^2} + \frac{1}{V_{Ai}^2} \right) > 0 \tag{19}$$

we can see that the condition $v_{2a} > V_{Ae}$ can hold, in which case the second of the differences (18) is positive and the slow mode also can be emitted. Consequently, for all parameter values satisfying conditions (2) in the limit $b \longrightarrow a$, the slow mode cannot be emitted and thus appears to be trapped; however, under condition
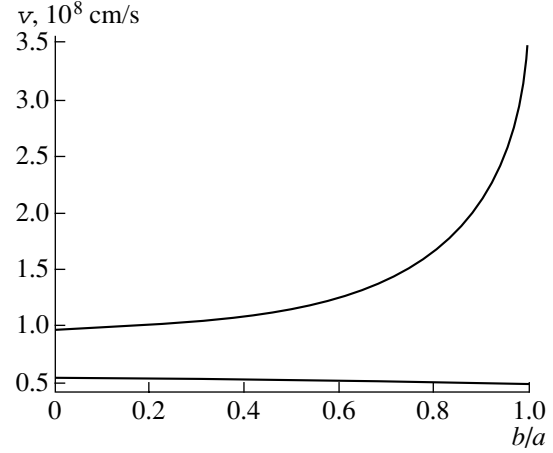
**Fig. 3.** Dependence of the phase velocities of FMS waves on the ratio of the filament radius to the shell radius. The upper and lower curves refer to the fast and slow modes, respectively.

(19), there exists a narrow range of $b$ values that are close to zero and at which the slow mode can be emitted. The dependence of the phase velocities of the fast and slow modes on the ratio $b/a$ is shown in Fig. 3.

In side the shell, the wave that can be emitted into space is a surface wave and, at the same time, it is an internal wave in the filament. Such a wave is generated within the filament and then is emitted from the outer surface of the shell. In the emission process, the wave is emitted only after it has penetrated the shell; in this sense, the emission process resembles the quantum tunneling of a particle through a potential barrier [12].

## 4. DAMPING OF THE OSCILLATIONS OF A CORONAL LOOP

According to the above analysis, a fast mode that is generated within a magnetic flux tube and is then emitted into the surrounding space can cause the oscillations of the tube to be damped. The damping is described by the imaginary part of the solution to dispersion relation (16). Recall that, in the zeroth approximation, the solution is purely real; consequently, the damping effect should manifest itself in the first approximation. We seek a solution to Eq. (16) in the form $\omega = \omega_0(1 + \varepsilon)$, where $\omega_0$ is the zero-order approximation and $\varepsilon \ll 1$ is the first-order correction. The quality factor of the oscillations can naturally be defined as $Q = 1/(2|\text{Im}\varepsilon|)$. We calculate only the imaginary part of the correction $\varepsilon$ because its real part makes only a small contribution to the real part of the frequency $\omega_0$. In the series expansions that will be used below, the quantity $v = \omega_0/k_z$ is treated as the phase velocity of the fast mode in the zeroth approximation. In dispersion relation (16), we take into account the first
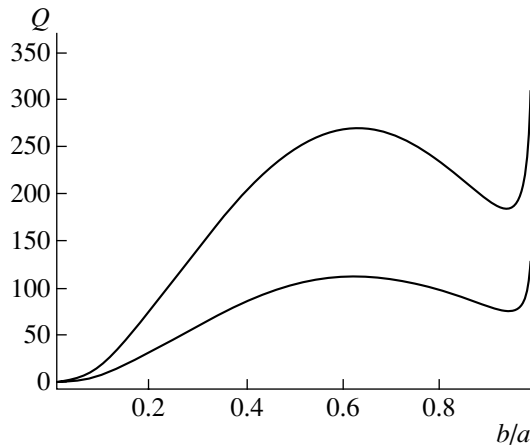
**Fig. 4.** Dependence of the quality factor $Q$ of oscillations at the frequency of the fast mode on the ratio $b/a$ of the filament radius to the shell radius. The upper and lower curves are calculated for $b = 2000$ km and $b = 3100$ km, respectively.

two terms in the series expansions for the solutions to the Bessel equation. As a result, we obtain

$$
\begin{aligned}
8v^2 \operatorname{Im}\varepsilon\{(a^2 - b^2) \\
\times [\rho_{0i}\rho_{0e}(2v^2 - V_{Ai}^2 - V_{Ae}^2) + 2\rho_{0m}^2(v^2 - V_{Am}^2)] \\
+ (a^2 + b^2)[\rho_{0m}\rho_{0i}(2v^2 - V_{Ai}^2 - V_{Am}^2) \\
+ \rho_{0m}\rho_{0e}(2v^2 - V_{Ae}^2 - V_{Am}^2)]\} + \pi k_e^2 a^2 \{(a^2 - b^2) \\
\times [\rho_{0i}\rho_{0e}(v^2 - V_{Ai}^2)(v^2 - V_{Ae}^2) - \rho_{0m}^2(v^2 - V_{Am}^2)^2] \\
+ (a^2 + b^2)[\rho_{0m}\rho_{0e}(v^2 - V_{Ae}^2)(v^2 - V_{Am}^2) \\
- \rho_{0m}\rho_{0i}(v^2 - V_{Ai}^2)(v^2 - V_{Am}^2)]\} = 0.
\end{aligned}
\tag{20}
$$

Dispersion relations (17) and (20) provide the solution to the problem about the damping of transverse oscillations of a magnetic flux tube with a shell. In particular, they make it possible to numerically calculate how the quality factor of oscillations depends on the ratio $b/a$. The results of such calculations are illustrated in Fig. 4. The calculations were carried out for the following values of Alfvén speeds in the unperturbed media: $V_{Ae} = 0.7 \times 10^8$ cm/s in the external region (in agreement with the observational data from [1]), $V_{Ai} = 0.39 \times 10^8$ cm/s in the filament, and $V_{Am} = 3.5 \times 10^8$ cm/s in the shell. The equilibrium values of the remaining model parameters correspond to transverse equilibrium condition (3) and the assumption that the gas pressure is negligible in comparison with the magnetic pressure. When Alfvén speeds in the shell and in the surrounding medium differ by a factor of 5, the densities in these two regions differ by a factor of 25. According to [13], the plasma density in the loops in the solar corona can be higher than that in the surrounding medium by a factor of 8 to 18. We assume that the den-

sity of the shell plasma can be lower than that of the surrounding plasma by approximately the same factor.

For the longitudinal wavenumber $k_z = \pi/L$ of oscillations with the period $T = 256$ s that were observed in a coronal loop of length $L = 130000$ km [2], we obtain $k_z = 0.024 \times 10^{-8}$ cm$^{-1}$; in this case, the phase velocity of oscillations is equal to $v = 1.02 \times 10^8$ cm/s, which corresponds to the fast mode. In Fig. 3, this value of the phase velocity corresponds the ratio $b/a \approx 0.3$. For the above values of Alfvén speeds, the condition for the slow mode to be emitted [i.e., dispersion relation (20)] is not satisfied, which indicates that, under the conditions adopted in our model, it remains trapped. From Fig. 4 we can see that, for the above value of the ratio $b/a$ and for $b = 3100$ km, the quality factor of the fast mode is about $Q \approx 40$, which coincides in order of magnitude with the values determined from observations.

## 5. DISCUSSIONS AND CONCLUSIONS

The quality factor obtained above is several times higher than the $Q$ value found in our earlier paper [11] ($Q \approx 9$), in which it was calculated by estimating the potential energy that is stored in the loop under the action of an initial external perturbation and is expended in emitting MHD waves into the surrounding space. In the present paper, we have treated the problem in a traditional formulation; i.e., instead of the initial perturbation of a given amplitude driven by an external action, we have considered infinitely small perturbations that are generated spontaneously in the system. We also assumed that the effect of radiative damping of oscillations is a priori small—the imaginary part of the frequency is a second-order quantity in the small parameter $k_z a$. A fundamentally important point in the model developed here is that an oscillating coronal loop with a nonuniform radial distribution of the plasma parameters is subject to a considerable radiative damping. Our preliminary estimates show that, in a more complicated model in which not only the nonuniformity of the plasma density but also that of the magnetic field in the loop is taken into account, the effect under consideration will be even more pronounced. The investigation of such a model is the subject of an ongoing investigation.

In order to provide a more realistic description of the one-dimensional oscillations of a coronal magnetic loop, we have developed a model that assumes that the ends of the loop are fixed in the photosphere and the internal loop structure is inhomogeneous. This model has allowed a significant amount of progress to be made in the investigation of the oscillatory properties of coronal loops. The main conclusions of our study can be formulated as follows:

(i) In contrast to the model of a homogeneous loop, the model of a magnetic flux tube with a shell yields a precise formulation of the problem of the radiative

damping of the transverse oscillations of a coronal loop.

(ii) The model with a shell makes it possible to describe two FMS waves whose propagation conditions are essentially different. The higher velocity mode can be emitted into the surrounding space; as a result, an oscillating loop becomes subject to radiative damping. The shell of the loop, within which FMS waves are of the same nature as surface waves, plays the role of a potential barrier through which the waves propagating from the central dense region pass into the environment.

(iii) Under the conditions in question, the other (lower velocity) FMS wave appears to be trapped in the central region of the tube. This effect is of interest for the problem of heating coronal loops. However, under appropriate model conditions, the lower velocity FMS mode also can be emitted from the loop.

(iv) In our model, the loop is assumed to comprise two internal structural components. The plasma density in the shell is lower than that in the filament and in the surrounding environment. The shell is thus a rarefied cavity surrounding a well pronounced hot and dense central region of the coronal loop.

## ACKNOWLEDGMENTS

## REFERENCES

1. M. J. Aschwanden, L. Fletcher, C. J. Schrijver, *et al.*, Astrophys. J. **520**, 880 (1999).
2. V. M. Nakariakov, L. Ofman, and E. E. Deluca, Science **285**, 862 (1999).
3. D. Tsiklauri and V. M. Nakariakov, Astron. Astrophys. **379**, 1106 (2001).
4. E. Robbrecht, E. Verwichte, D. Berghmans, *et al.*, Astron. Astrophys. **370**, 591 (2001).
5. B. Roberts, P. M. Edwin, and O. A. Benz, Astrophys. J. **279**, 857 (1984).
6. B. I. Meerson, P. V. Sasorov, and A. V. Stepanov, Sol. Phys. **56**, 165 (1978).
7. P. R. Wilson, Astron. Astrophys. **87**, 121 (1980).
8. H. S. Spruit, Sol. Phys. **75**, 3 (1982).
9. P. M. Edwin and B. Roberts, Sol. Phys. **88**, 179 (1983).
10. M. S. Ruderman and B. Roberts, Astrophys. J. **577**, 475 (2002).
11. A. A. Solov'ev, B. B. Mikhalyaev, and E. A. Kirichek, Fiz. Plazmy **28**, 758 (2002) [Plasma Phys. Rep. **28**, 699 (2002)].
12. Y. D. Zhugzhda, Sol. Phys. **25**, 329 (1972).
13. M. J. Aschwanden, Astrophys. J. **560**, 1035 (2001).

*Translated by O.E. Khadin*

# Investigation of the Anisotropic Electron Distribution Function in a Glow Discharge in Hydrogen

## Yu. B. Pankrashkin and M. B. Shapochkin

*Moscow Power Engineering Institute (Technical University), ul. Krasnokazarmennaya 14, Moscow, 111250 Russia*
Received October 23, 2002; in final form, February 27, 2003

**Abstract**—Results are presented from measurements of the electron distribution function in a glow discharge in hydrogen with the help of a plane probe by the second-harmonic method. The parameters are determined for a model description of the distribution function of thermal and suprathermal electrons. © *2003 MAIK "Nauka/Interperiodica".*

## 1. INTRODUCTION

When a current flows through an ionized gas, the velocity distributions of positive and negative charge carriers are always anisotropic: each of the functions has a component describing the directed current of the corresponding type of carrier. The anisotropy can arise, e.g., due to the energy and particle input in the plasma. The directed motion of plasma electrons is described by an anisotropic electron distribution function (EDF). A detailed study of the processes occurring in gas discharges requires a determination of the suprathermal anisotropic part of the EDF.

The parameters of the EDF in a plasma can be estimated from the probe current–voltage (*I–V*) characteristic in terms of the Langmuir theory [1] only under the assumption that charged particles obey isotropic Maxwellian velocity distributions. However, this assumption significantly limits the possibility of measuring the EDF. Under actual gas-discharge conditions, there is a vast variety of factors resulting in plasma anisotropy. This is why probe diagnostic methods [2–9] need to be modified. The relative motion of the plasma and the probe can also be considered as a kind of anisotropy. The results of measurements [2–7] show that the EDF not only deviates substantially from being Maxwellian but also is often anisotropic.

The problem of investigating the anisotropic EDF can be successfully solved by spectropolarimetric methods [10–14]. This implies solving the inverse problem in which the parameters of the anisotropic EDF are determined from the measured degree of the linear polarization of atomic line emission, provided that the model anisotropic EDF is prescribed [12]. In [12–14], it was shown that the anisotropic EDF can be described well by the expression

$$f(\varepsilon, \theta, \varphi) = \frac{N_t}{4\pi} f_t(\varepsilon) + N_{st} f_{st}(\varepsilon, \theta) f_{st}(\varepsilon), \quad (1)$$

where $N_t$ is the density of thermal electrons, $f_t(\varepsilon)$ is their Maxwellian energy distribution function with the temperature $T_0$, $N_{st}$ is the density of suprathermal electrons, and $f_{st}(\varepsilon)$ is their energy distribution function.

An analysis of the results of calculations of the intensities of spectral lines by means of a Maxwellian and a power-law distribution function shows that the power-law function is more appropriate for describing suprathermal electrons:

$$f_{st}(\varepsilon) = \frac{1-\gamma}{\varepsilon_1}\left(\frac{\varepsilon}{\varepsilon_1}\right)^{-\gamma}, \quad (2)$$

where $\varepsilon_1$ and $\gamma$ are the constants of the distribution.

We specify the angular dependence of the distribution function of suprathermal electrons in the following form:

$$f_{st}(\varepsilon, \theta) = \begin{cases} \dfrac{a+1}{2\pi}\cos^a\Theta & \text{for} \quad 0 < \Theta \le \dfrac{\pi}{2} \\ 0 & \text{for} \quad \dfrac{\pi}{2} \le \Theta \le \pi, \end{cases} \quad (3)$$

where $a = \dfrac{\bar{\varepsilon}}{\varepsilon_2}$, with $\varepsilon_2$ being the anisotropy constant.

Thus, for an electron beam, we have $a \longrightarrow \infty$, whereas, as $a \longrightarrow 0$, the distribution tends to become isotropic.

Unfortunately, the validity of expression (1) has not yet been confirmed by the probe measurements of the anisotropic EDF in spectropolarimetric studies. In the present paper, which is aimed at measuring the anisotropic EDF by probes and determining the parameters of a model distribution function in a glow discharge in hydrogen, we bridge this gap.

## 2. FORMULATION OF THE PROBLEM

By measuring the second derivative of the probe current *I* with respect to the probe voltage *U* at different
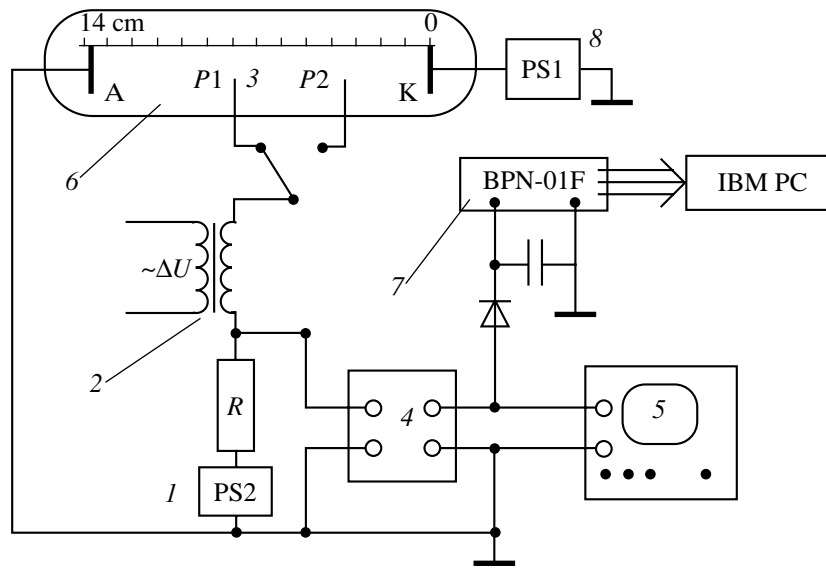
**Fig. 1.** Circuit diagram of the experimental setup: (*1*) B3-3 power source for supplying the probes; (*2*) transformer; (*3*) probes *P*1 and *P*2; (*4*) U2-8 narrowband amplifier; (*5*) oscilloscope; (*6*) gas-discharge tube; (*7*) BPN-01F analog-to-digital converter, controlled by an IBM PC; and (*8*) power supply unit for the gas-discharge tube.

values of the latter, we can completely determine the EDF [2]:

$$f(\varepsilon) = \frac{4m}{e^2 N_e S} U \frac{d^2 I}{dU^2}, \tag{4}$$

where $S$ is the surface area of the probe and $N_e$ is the electron density.

There are several approaches to solving the problem of probe measurements in an anisotropic plasma [3, 6–8]. In these approaches, which apply to an axisymmetric plasma, the electron velocity distribution function is specified in spherical coordinates with the polar axis pointing along the symmetry axis of the plasma and can be expanded in a series in Legendre polynomials. Measurements by a double-sided plane probe and a cylindrical probe make it possible to determine the coefficients of the even terms of the series expansion. The coefficients of both the even and odd terms of the expansion can be determined from measurements by a one-sided and a double-sided plane probe. Thus, in [7], the potentialities of this approach were demonstrated experimentally by investigating low-voltage arc discharges in helium with the help of two cylindrical probes oriented along and perpendicular to the symmetry axis of the discharge gap.

The first and second derivatives of the probe current with respect to the probe voltage can be determined graphically from the probe *I–V* characteristic. However, this method may lead to significant errors. This is why Zakharov [9] proposed an experimental method for directly determining the second derivative of the probe *I–V* characteristic. In this method, the probe is held at a

voltage that is the sum of a slowly varying voltage $U_0$ and a voltage $U_1$ varying rapidly at the frequency $\omega$:

$$U = U_0 + U_1 \cos(\omega t). \tag{5}$$

In this case, the current to the probe is described by the expression

$$I = f(U_0 + U_1 \cos(\omega t)). \tag{6}$$

If the voltage amplitude $U_1$ is sufficiently small, we can expand the current in harmonics of the frequency $\omega$:

$$\begin{aligned} I &= \left[ f(U_0) + \frac{1}{4} U_1^2 f''(U_0) + \ldots \right] \\ &\quad + [U_1^2 f'(U_0) + \ldots] \cos(\omega t) \\ &\quad + \left[ \frac{U_1^2}{4} f''(U_0) + \ldots \right] \cos(2\omega t) \\ &= A_0 + A_1 \cos(\omega t) + A_2 \cos(2\omega t). \end{aligned} \tag{7}$$

This expansion shows that the coefficient $A_2$ of the second current harmonic is determined by the second derivative to within terms of higher orders. The second harmonic of the probe current is singled out using a filter or a narrowband amplifier.

## 3. EXPERIMENTAL SETUP

The anisotropic EDF was measured in glow discharges in hydrogen at a pressure of about $10^{-2}$ mm Hg (Fig. 1). The positive discharge column in hydrogen is stratified, which means that the EDF is spatially nonuniform. The distance between the indirectly heated cathode and the anode in the discharge tube was 135 mm.
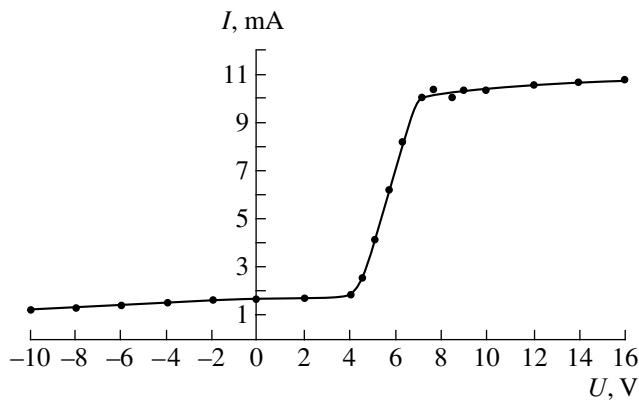
**Fig. 2.** *I–V* characteristic of probe *P*1: the points show the experimental data and the solid curve was obtained by their linear interpolation.
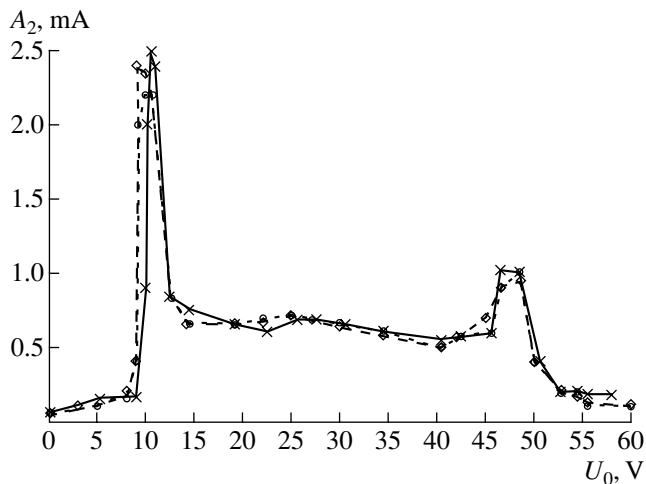


**Fig. 3.** Dependence of the amplitude $A_2$ of the second harmonic of the current to plane probe *P*1 on the voltage amplitude $U_0$ for different voltages between the anode and cathode: 250 V (diamonds), 300 V (crosses), and 350 V (circles).

The measurements were carried out by two 1.5-mm-diameter plane probes soldered into the discharge tube at distances of 35 and 80 mm from the cathode along the discharge axis. The tube was 40 mm in diameter. The dc voltage between the cathode and anode was supplied from a B3-3 power source (PS1). The distribution function was measured in regimes with discharge currents of 30, 35, and 42 mA, the voltages between the cathode and anode being 250, 300, and 350 V, respectively. The probes were held at a dc voltage that was varied between –30 and +60 V and was supplied from a B3-3 power source (PS2) (*1*). At higher voltages, the probes begin to function as anodes, which may cause their destruction.

At the same time, an ac voltage was supplied to the probes by means of transformer *2*. The ac voltage amplitude $U_1$ was 0.1 V, which did not exceed the 0.1 of the dc voltage amplitude $U_0$ over the entire range of measurements. As an ac voltage source, we used a sine-wave oscillator operating at a frequency of 500 Hz.

The voltage signal from the measuring resistor *R* was fed to a U2-8 narrowband amplifier (*4*), which was used to single out the second harmonic (with a frequency of 1000 Hz). The amplified ac signal was then fed to an oscilloscope and, simultaneously, to a rectifying diode. The rectified signal was digitized by a BPN-01F analog-to-digital converter and was stored in an IBM PC for further processing.

## 4. RESULTS FROM PROBE MEASUREMENTS

The measurements were carried out with two plane probes placed at different distances from the cathode. The data from each of the probes were obtained for three different values of the voltage between the cathode and anode: 250, 300, and 350 V.

In the first stage of the experiment, we measured the *I–V* characteristic of each of the probes by the Langmuir single-probe method [1].

The plasma potential near probe *P*1 was determined from the position of the inflection point in the *I–V* characteristic and was found to be 8 V. This potential corresponded to a "zero" energy for the EDF [1] (see Fig. 2). Accordingly, when determining the anisotropic EDF, the results of the second-harmonic measurements (Fig. 3) were shifted along the energy axis by an amount equal to this plasma potential, 8 V. Under the assumption that the plasma electrons obey a Maxwellian velocity distribution, we can calculate the temperature of the thermal electrons [1],

$$T_e = -\frac{e}{k\dfrac{d\ln(I)}{dU}},$$

where *k* is Boltzmann's constant.

Measurements with probe *P*1 yielded an electron temperature of 22 500 K (or 2.3 eV).

In the second stage of the experiment, we measured the EDF with both probes by the second-harmonic method [9]. Figure 3 shows the amplitude of the second harmonic of the anode current (*7*) measured by probe *P*1 in three different discharge regimes, while Fig. 4 illustrates the results of measurements with probe *P*2. The probes were oriented so that the normals to their surfaces were perpendicular to the discharge axis (Fig. 1).

As can be seen from Figs. 3 and 4, the EDF is weakly sensitive to the discharge regime.

However, the two probes gave somewhat different results. By averaging the results of measurements over different regimes and by shifting them along the energy axis by an amount equal to the plasma potential
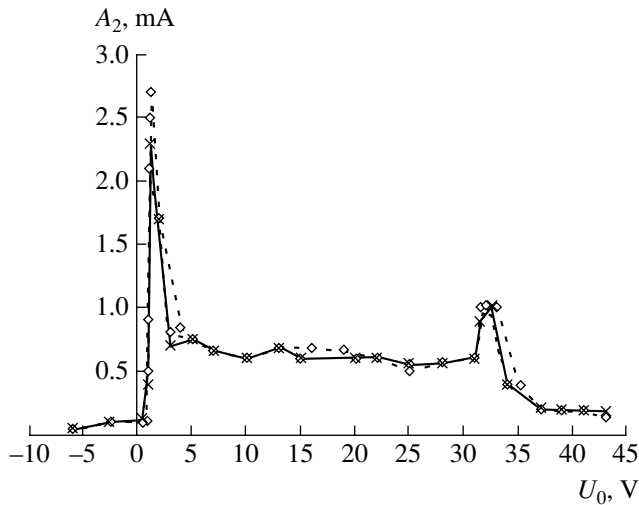
**Fig. 4.** Dependence of the amplitude $A_2$ of the second harmonic of the current to plane probe $P2$ on the voltage amplitude $U_0$ for different voltages between the anode and cathode: 250 V (diamonds), 300 V (crosses), and 350 V (circles).

obtained from the probe *I–V* characteristic, we can compare the EDFs measured by the two probes (Fig. 5). The results derived in this way show clearly that the anisotropic EDF has a component with energies of up to 5 eV; this component corresponds to thermal electrons with a Maxwellian distribution. The temperature of these thermal electrons was determined from the position of the first peak in the EDF and was found to be about 2 eV, which coincides with the temperature value obtained from the *I–V* characteristic by the method developed by Langmuir and Mott-Smith [1]. Since the data on the EDF from each probe in all discharge regimes are highly reproducible and since the second-harmonic method and the single-probe method yield nearly the same temperatures of the thermal elec-
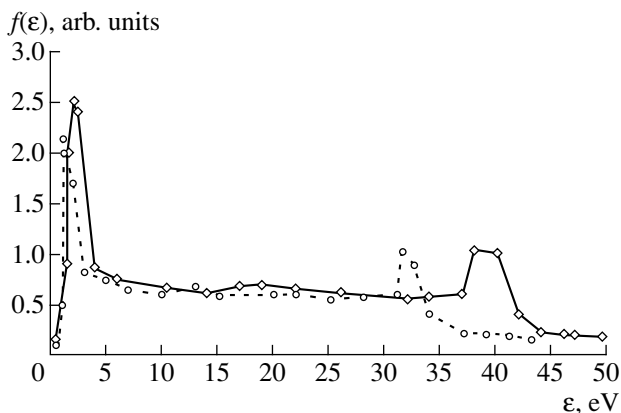
trons, it is justifiable to presume that the probes only slightly perturb the plasma and thereby have an insignificant impact on the measurement accuracy.

At energies higher than 5 eV, the EDF is seen to deviate substantially from a Maxwellian function. This energy range corresponds to anisotropic suprathermal electrons.

The second peak in the measured EDF in the energy range 30–40 eV can be associated with the initially Maxwellian electrons that are emitted from the cathode.

The accuracy of measurements of the anisotropic EDF by the second-harmonic method is determined by the extent to which the measured results are reproducible. In the energy range around the first peak, where the EDF character changes radically, the measurement error was no larger than 10%. At other energies, the measurement error was less than 3%.

## 5. DETERMINATION OF THE PARAMETERS FOR A MODEL DESCRIPTION OF THE EDF

From Fig. 6, we can see that, in the energy range corresponding to thermal electrons, the EDF measured by probe $P2$ is well approximated by the Maxwellian function

$$f(\varepsilon) = \frac{2}{\sqrt{\pi}}(kT)^{-3/2}\exp\left\{-\frac{\varepsilon}{kT}\right\}\sqrt{\varepsilon}$$

with the temperature $T = 2$ eV.

The remaining part of the EDF corresponds to suprathermal electrons and can be approximated by power-law function (2). In contrast to the thermal electrons, which obey an isotropic Maxwellian distribution, the suprathermal electrons are described by anisotropic distribution function (3). Consequently, the conditions under which these two groups of electrons contribute to the resulting probe current are different. This is why a
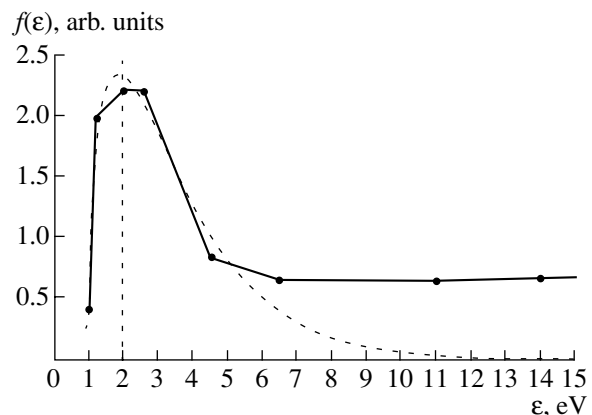


**Fig. 5.** EDFs obtained from measurements by probe $P1$ (circles) and probe $P2$ (diamonds).



**Fig. 6.** Approximation of the experimental EDF (circles) by a Maxwellian function (dashed curve).

Parameters of the model distribution

| | 250 V | 300 V | 350 V |
|---|---|---|---|
| | $T, \varepsilon_1, \gamma, \delta$ | $T, \varepsilon_1, \gamma, \delta$ | $T, \varepsilon_1, \gamma, \delta$ |
| Probe $P1$ | 2.3; 10; 1.7; 88% | 2.3; 10; 1.7; 90% | 2.0; 10; 1.7; 90% |
| Probe $P2$ | 2.0; 10; 1.8; 85% | 2.0; 10; 1.8; 85% | 2.0; 10; 1.8; 85% |

comparison of the parts of the anisotropic EDF that correspond to thermal and suprathermal electrons does not provide adequate information about the numbers of these electrons.

In order to estimate the accuracy with which the parameters $T$, $\varepsilon_1$, and $\gamma$ of the power-law EDF are adjusted to fit the experimental data, we determine how the ratio

$$\delta = \frac{|S_{pl} - S_{exp}|}{S_{exp}}$$



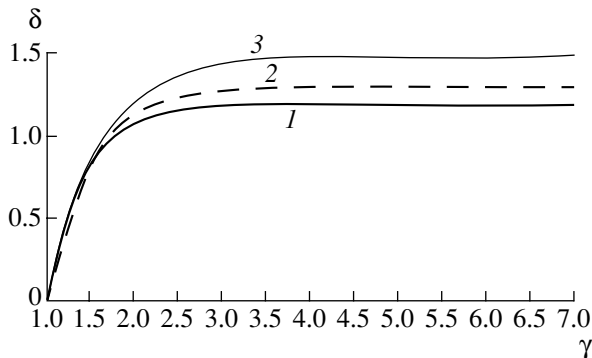**Fig. 7.** Dependence of the parameter $\delta$ on $\gamma$ for $\varepsilon_1 = $ (*1*) 5, (*2*) 7, and (*3*) 10.
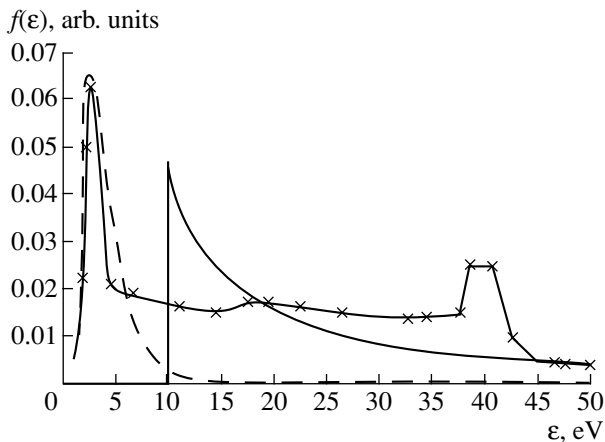


**Fig. 8.** Comparison of the anisotropic EDF obtained experimentally from probe $P1$ (crosses) with a Maxwellian function (dashed curve) and a power-law distribution function of suprathermal electrons (solid curve).

depends on these parameters. Here, $S_{pl}$ is the area under the curve of the power-law EDF and $S_{exp}$ is the area under the curve of the experimentally obtained EDF.

As an example, Fig. 7 shows the plot of the ratio of these areas versus the parameter $\gamma$.

It was found that the most suitable parameter values for a model EDF approximating the EDF obtained experimentally by the first probe are $\gamma = 1.7$ and $\varepsilon_1 = 10$ eV. For these parameter values, we have $\delta = 90\%$. The plot of the power-law EDF with these parameter values in the energy range above 10 eV is shown in Fig. 8.

The values of the parameters $T$ (in eV), $\varepsilon_1$ (in eV), and $\gamma$ obtained from probes $P1$ and $P2$ in all regimes and the accuracy $\delta$ with which the parameters were determined are given in the table.

The peak in the energy range around 40 eV in Fig. 8 can be approximated, e.g., by a Gaussian function. However, the fraction of these electrons in the total number of suprathermal electrons is as small as 15%. Consequently, in expression (1) for the anisotropic EDF, this electron subgroup can be neglected, the loss of accuracy being just 15%. Otherwise, expression (1) should be supplemented with the corresponding term describing these electrons.

## 6. CONCLUSIONS

The results of measuring the EDF in a glow discharge in hydrogen show that there is a substantial amount of suprathermal electrons that should be taken into account when analyzing the kinetics of the discharge processes. These suprathermal electrons can be described by the power-law distribution function whose parameters have been determined in our study. The description of suprathermal electrons by a Maxwellian distribution function is far less accurate, which agrees with the conclusions obtained from an analysis of the optical spectra [14]. The anisotropy parameter $\varepsilon_2$ of model distribution function (3) is reliably determined by spectropolarimetric methods [13, 14], while the probe method for measuring the anisotropic EDF fails to determine it.

## REFERENCES

1. I. Langmuir and H. M. Mott-Smith, Phys. Rev. **28**, 727 (1926).
2. M. J. Druyvesteyn, Z. Phys. **64**, 781 (1930).

3. Yu. M. Kagan, G. M. Malyshev, and V. L. Fedorov, Zh. Tekh. Fiz. **23**, 894 (1953).

4. R. M. Howe, J. Appl. Phys. **24**, 881 (1953).

5. N. D. Twiddy, Proc. R. Soc. London, Ser. A **262**, 379 (1961).

6. N. A. Vorob'eva, Yu. M. Kagan, and V. M. Milenin, Zh. Tekh. Fiz. **33**, 571 (1963) [Sov. Phys. Tech. Phys. **8**, 423 (1963)].

7. A. P. Mezentsev, A. S. Mustafaev, and V. L. Fedorov, Zh. Tekh. Fiz. **55**, 544 (1985) [Sov. Phys. Tech. Phys. **30**, 322 (1985)].

8. V. F. Lapshin and A. S. Mustafaev, Zh. Tekh. Fiz. **59** (2), 35 (1989) [Sov. Phys. Tech. Phys. **34**, 150 (1989)].

9. V. M. Zakharov, Zh. Tekh. Fiz. **30**, 442 (1960) [Sov. Phys. Tech. Phys. **5**, 411 (1960)].

10. S. A. Kazantsev and A. V. Subbotenko, Fiz. Plazmy **10**, 135 (1984) [Sov. J. Plasma Phys. **10**, 78 (1984)].

11. S. A. Kazantsev and J. C. Henoux, *Polarization Spectroscopy of Ionized Gases* (Kluwer, London, 1995), p. 214.

12. E. Haug, Sol. Phys. **61**, 129 (1979).

13. M. B. Shapochkin, Fiz. Plazmy **27**, 734 (2001) [Plasma Phys. Rep. **27**, 692 (2001)].

14. F. Walden, H.-J. Kunze, A. Petoyan, *et al.*, Phys. Rev. E **59**, 3562 (1999).

*Translated by G.V. Shepekina*

<div align="center">

LOW-TEMPERATURE
PLASMA

</div>

# Abnormal and Subnormal Regimes of a Spherical Glow Discharge in the Drift-Diffusion Approximation

## G. I. Sukhinin and A. V. Fedoseev

*Kutateladze Institute of Thermophysics, Siberian Division, Russian Academy of Sciences,*
*pr. Akademika Lavrent'eva 1, Novosibirsk, 630090 Russia*
Received October 30, 2002; in final form, June 4, 2003

**Abstract**—A spherical glow discharge with a pointlike anode is considered in a self-consistent drift-diffusion approximation. The model includes the time-dependent continuity equations for ions and electrons in the drift-diffusion approximation and Poisson's equation for the radial electric field. In finding steady-state distributions, Ohm's law is used to relate the discharge voltage and discharge current. Steady-state distributions of the plasma parameters across the discharge gap, current–voltage characteristics, and cathode characteristics for an abnormal spherical discharge in molecular nitrogen are obtained. In a subnormal glow-discharge regime, oscillations in the conduction current, potential, and other discharge parameters are revealed. Similar regimes are also observed in conventional discharges in tubes. © 2003 MAIK "Nauka/Interperiodica".

## 1. INTRODUCTION

At present, glow dc discharges in tubes [1, 2] are one of the best studied types of glow discharges. In recent years, volume discharges with a pointlike anode [3–7] have attracted considerable interest. A spherical glow discharge with a central small-size anode enclosed by a large-area spherical cathode was investigated in [5–7]. Studies of a spherical discharge with a pointlike anode show that the discharge structure is qualitatively the same as that of a plane discharge. In particular, the cathode sheath and the positive column are formed and the electric properties and cathode characteristics of a spherical glow discharge, on the whole, correspond to those of discharges in tubes. At the same time, spherical discharges differ substantially from conventional glow discharges in tubes. For example, the spatial distributions of the electron and ion densities in the positive column of a spherical discharge are highly nonuniform. At high discharge voltages, the charged particle densities decrease in inverse proportion to the square of distance from the pointlike anode. In contrast to the plasma of the positive column in tubes, the space charge is nonzero and decreases in inverse proportion of the distance from the anode.

In this paper, a spherical glow discharge is considered using a self-consistent time-dependent drift-diffusion model for the entire discharge gap. We use a spherically symmetric one-dimensional model in which all the parameters depend only on the distance from the anode center. We also assume that the cathode is entirely occupied by the discharge current. Such a model, in spite of its simplicity, yields qualitatively correct radial distributions of the plasma parameters in a spherical abnormal discharge. To describe the normal regime of a spherical glow discharge, when the spheri-

cal symmetry is lost, it is necessary to consider a two-dimensional problem.

One of the classical problems of gas discharge physics is the study of different discharge regimes. There are subnormal, normal, and abnormal regimes of a glow discharge, which occur over a wide range of gas pressures $p$, discharge voltages $U_d$, and discharge currents $J_d$ [8]. In many experimental studies, it was pointed out that, in subnormal discharges in tubes (i.e., in the transition region between a Townsend discharge and a normal glow discharge), there is a regime of self-sustained oscillations of the discharge current [8–12]. When studying spherical discharges, it was also found that, in the parameter range corresponding to a subnormal discharge, the system changes to an oscillatory regime if the power source voltage is insufficient for sustaining a discharge with a well-formed cathode sheath.

## 2. MODEL

In this paper, a spherical glow discharge in a low-density ($0.1 \leq p \leq 5$ torr) molecular nitrogen was simulated using time-dependent equations for ion and electron transport in a self-consistent electric field that was determined from Poisson's equation. Steady-state solutions were found by the relaxation method over the entire discharge gap (from the anode to the cathode). The radii of the spherical anode and the surrounding cathode ($a = 0.5$, $R_c = 12.5$) were chosen in accordance with the geometrical dimensions of the devices in which spherical stratified discharges have been investigated [5–7]. In view of their spherical symmetry, all of the plasma parameters were assumed to depend only on the radial coordinate.

It was assumed that the chamber contained neutral nitrogen with a molecular density of $N_g \sim 10^{16}$ cm$^{-3}$ at room temperature, ions with a density $n_i$, and electrons with a density $n_e$. The electron and ion flows were considered in the drift-diffusion approximation:

$$\Gamma_e = -n_e \mu_e E - D_e \frac{\partial n_e}{\partial r}, \qquad (1)$$

$$\Gamma_i = +n_i \mu_i E - D_i \frac{\partial n_i}{\partial r}, \qquad (2)$$

where $\mu_e$ ($\mu_i$) is the electron (ion) mobility and $D_e$ ($D_i$) is the electron (ion) diffusion coefficient. The particle densities satisfy the continuity equations

$$\frac{\partial n_e}{\partial t} + \frac{1}{r^2}\frac{\partial}{\partial r}(r^2 \Gamma_e) = N_g \alpha_i(T_e)|\Gamma_e| - \beta_r n_e n_i, \qquad (3)$$

$$\frac{\partial n_i}{\partial t} + \frac{1}{r^2}\frac{\partial}{\partial r}(r^2 \Gamma_i) = N_g \alpha_i(T_e)|\Gamma_e| - \beta_r n_e n_i, \qquad (4)$$

where the ionization coefficient $\alpha_i$, the diffusion coefficients of electrons and ions, and their drift velocities ($W_{e,i} = \mu_{e,i} E$) were specified in the local field approximation. The diffusion coefficients and the mobilities of electrons and $N_2^+$ ions in molecular nitrogen and the electron-impact ionization coefficients for nitrogen as functions of the reduced electric field were taken from [13, 14]. The coefficient of electron dissociative recombination in nitrogen $\beta_r$ was assumed to be constant and equal to $2 \times 10^{-7}$ cm$^{-3}$ [15].

The radial distribution of the electric field in the discharge gap was found from Poisson's equation

$$-\frac{1}{r^2}\frac{\partial}{\partial r}\left(r^2 \frac{\partial \varphi}{\partial r}\right) = 4\pi e(n_i - n_e), \quad E(r) = -\frac{\partial \varphi}{\partial r}. \quad (5)$$

Equations (1)–(5) were solved numerically by the relaxation method on a uniform mesh (500–1000 nodes) using an implicit scheme. The initial conditions were specified throughout the entire discharge gap. The boundary conditions for the electron and ion flows were imposed at the anode and cathode. The initial electron and ion densities were assumed to be uniform and equal to a certain small value ($n_i(r, t = 0) = n_e(r, t = 0) = $ const $\sim 10^4$ cm$^{-3}$). The grounded cathode ($r = R_c$) was maintained at a zero potential. At the anode, the initial potential was equal to the power supply voltage (see Fig. 1).

The initial distributions of the potential and the electric field in the discharge gap were given in the form

$$U(r, t = 0) = U_{ps}(r^{-1} - R_c^{-1})/(a^{-1} - R_c^{-1}),$$

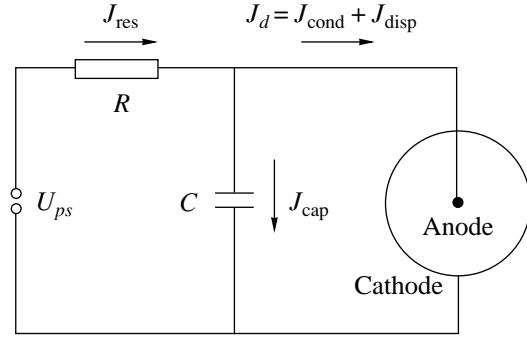$$E(r, t = 0) = \frac{U_{ps}}{r^2}/(a^{-1} - R_c^{-1}),$$

**Fig. 1.** Electric circuit: $U_{ps}$ is the power supply, $R$ is the resistance of the external circuit, and $C$ is the capacitance.

where $U_{ps}$ is the power supply voltage. The boundary conditions were imposed as follows:

(i) At the cathode, we specified the condition of secondary electron emission, $\Gamma_e = -\gamma_T \Gamma_i$, where $\gamma_T$ is the second Townsend coefficient. The values of the effective secondary-emission coefficient for various gases and materials lie in the range $10^{-2}$–$10^{-1}$ [1] and somewhat increase with increasing reduced field $E/N_g$. In this paper, the coefficient $\gamma_T$ is assumed to be independent of $E/N_g$ and equal to 0.05.

(ii) The second spatial derivative of the ion density at the cathode was taken to be zero, $\partial^2 n_i/\partial r^2|_c = 0$. This is the so-called free-inflow condition, which limits neither the value of the ion density $n_i$ ($r = R_c$) nor its derivative $\partial n_i/\partial r$ at the cathode.

(iii) The ion flux density at the anode was assumed to be zero, $\Gamma_i = 0$.

(iv) The free-inflow condition for electrons was imposed at the anode, $\partial^2 n_e/\partial r^2|_a = 0$.

The calculations showed that the choice of other boundary conditions for ions at the cathode and for electrons at the anode affected the results obtained insignificantly.

Subtracting Eq. (3) from Eq. (4) and substituting the result into Eq. (5), we find the expression for the total discharge current,

$$J_d = 4\pi e r^2(\Gamma_i - \Gamma_e) + r^2\frac{\partial E}{\partial t}, \qquad (6)$$

where the first term is the conduction current $J_{cond}$ and the second term is the displacement current $J_{disp}$. It follows from the derivation of Eq. (6) that $J_d$ should be spatially uniform; i.e., it should be independent of the radius. The constancy of the total current $J_d(t)$ throughout the entire discharge gap in the course of the discharge served as an additional criterion of the correctness of the simulation results. The displacement current $J_{disp}$ differed from zero only in unsteady and oscillatory regimes.
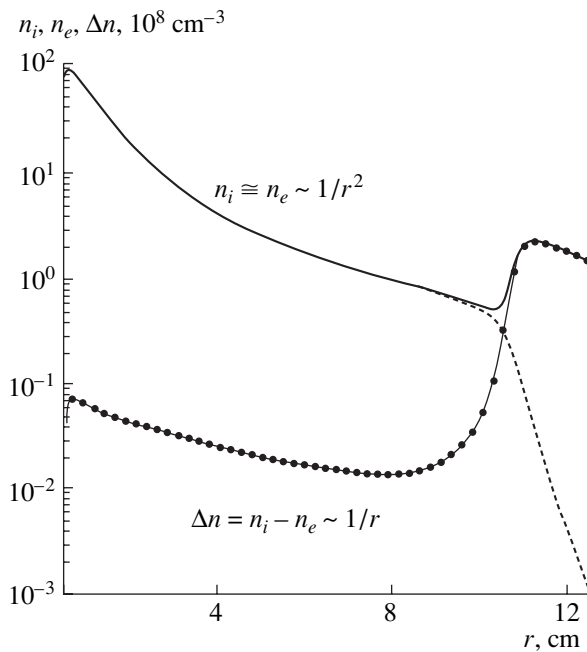
**Fig. 2.** Radial steady-state distribution of the ion density $n_i(r)$ (solid line), electron density $n_e(r)$ (dashed line), and positive charge density $\Delta n(r)$ (dots).

In numerical simulations, the time step $\Delta t$ depended on the gas pressure and was varied from $10^{-6}$ to $10^{-4}$ μs. Poisson's equation for the potential was solved by the sweep method with a zero boundary condition at the cathode, $U(r = R_c, t) = 0$. The positive potential at the anode $U_d$ was recalculated at every time step using the feedback equation.

Figure 1 shows the diagram of the electric circuit, which contains a power supply with a voltage of $U_{ps} = 0.5–6$ kV, an external-circuit resistance of $R = 20$ kΩ, a capacitance of $C = 500$ pF, and the spherical discharge chamber. As a feedback equation, we use Ohm's law, relating the discharge voltage $U_d$ to the discharge current $J_d$ (for a given power supply voltage $U_{ps}$):

$$U_d = U_{ps} - RJ_{res}, \qquad (7)$$

where $J_{res}$ is the electric current in the external circuit, which is equal to the sum of the currents flowing through the discharge and the capacitor of the external circuit: $J_{res} = J_d + J_{cap}$. The current through the capacitor can be represented in the form

$$J_{cap} = \frac{U_{ps} - U_d}{R} - (J_{cond} + J_{disp}). \qquad (8)$$

The presence of the capacitive current leads to a change in the voltage across the capacitor. This change is equal to the change in the discharge voltage. As a result, the change in the anode voltage $\Delta U$ during the time step $\Delta t$ can be represented as follows:

$$\Delta U = \frac{1}{C} J_{cap} \Delta t. \qquad (9)$$

## 3. RESULTS OF CALCULATIONS AND DISCUSSION

The computational procedure was as follows. The time-dependent problem (1)–(5) was solved for a certain gas pressure lying in the above range and a sufficiently high power supply voltage ($U_{ps} > 2000$ V). The plasma parameters in the discharge gap evolved from the initial distribution to a certain steady-state distribution. The temporal stages of the evolution of a spherical discharge are described in detail in [16]. As a result, after $10^7–10^8$ time steps that corresponded to times of a few hundred microseconds, a steady-state equilibrium distribution of the plasma parameters was established, including the cathode sheath and the positive column (PC), in which the radial electric field depended slightly on the radius.

Figure 2 shows an example of the radial distributions of the electron and ion densities, $n_e(r)$ and $n_i(r)$, and their difference $\Delta n(r)$ at the time $t \approx 100$ μs. The cathode radius is $R_c = 12.5$ cm, and the anode radius is $a = 0.5$ cm. The power supply voltage is $U_{ps} = 2$ kV. The nitrogen pressure is $p = 0.5$ torr. By this time, the conduction current $J_{cond}$ and the total current $J_d = 70$ mA become constant throughout the entire discharge gap, whereas the displacement current almost completely vanishes (the relative value of the displacement current is less than $10^{-5}$). This regime can be regarded as completely established, and the parameters in the discharge can be considered steady-state. One can see the formed cathode sheath with a length of $d_c \sim 1–2$ cm, in which the ion density substantially exceeds the electron density, and the PC. Here, by PC, we traditionally mean the region in which the ion density differ only slightly from the electron density. Under these conditions, the electric field strength at the cathode is on the order of $E_c(r) \sim 200$ V/cm. In the PC, the reduced electric field depends only slightly on the radius and is on the order of $E/p \sim 10$ V/(cm torr). The electron and ion density distributions in the PC vary as $n_i(r) \sim n_e(r) \sim 1/r^2$. The space charge in the PC is nonzero, $\Delta n = (n_i - n_e) \sim 1/r$, which is a characteristic feature of a spherical discharge. It can be seen that the quasineutrality condition in the PC is satisfied accurate to within a value on the order of $|\Delta n|/n_i \sim 10^{-3}–10^{-2}$. Indeed, it follows from Poisson's equation (5) that, in the spherical case, the space charge density at a constant field $E(r) = E_0$ should vary in inverse proportion to $r$:

$$\Delta n = (n_i - n_e) = \frac{1}{2\pi e} \frac{E_0}{r},$$

whereas in the case of plane geometry and a constant field, we have $\Delta n = 0$.

After a steady-state discharge regime had been reached for one value of the power supply voltage, the value of $U_{ps}$ was changed by $\Delta U_{ps} = 50$–$500$ V at a fixed gas pressure. The previously calculated radial distributions of the plasma parameters (the charged particle densities and the electric field strength) were then used as initial data. After a relaxation process that lasted several dozen microseconds, the system arrived at a new steady state with new values of the potential and the discharge current. In this way, the current–voltage characteristic of the discharge was calculated for a fixed gas pressure. The gas pressure was then altered somewhat, and the procedure was repeated. As a result of such numerical experiments, the current–voltage characteristics were obtained for different gas pressures.

Figure 3 shows typical current–voltage characteristics of a spherical discharge for different nitrogen pressures. The minimum pressure is $p = 0.1$ torr (at pressures of $p \leq 1$ torr the curves everywhere have a positive slope). As the pressure increases, both the slope of the curves and the discharge voltage $U_d$ decrease. For $p = 0.8$–$1.0$ torr, the discharge voltage $U_d$ is minimum. At pressures above 1 torr, a minimum appears in the current–voltage characteristic in the current range under consideration. The minima of the current–voltage characteristics for $p = 2, 3, 4$, and 5 torr are indicated by large crosses and are joined by the dashed line. It can be seen that, as the discharge current increases, the current–voltage characteristics come closer to the lowest current–voltage characteristic, corresponding to the pressure $p \approx 1$ torr.

It is well known that the higher the gas pressure, the higher the power supply voltage $U_{ps}$ required for maintaining the abnormal regime of a glow discharge. From Fig. 3, it can be seen that, as the pressure increases, the minima of the current–voltage characteristics shift toward high currents, which corresponds to higher power supply voltages. At the left branches of the current–voltage characteristics, the discharge becomes unstable. As the power supply voltage decreases, the length of the cathode sheath increases and the electric field at the cathode decreases. As a result, a regime is established in which all the discharge parameters oscillate. Similar oscillations were observed experimentally in tubes in the parameter range corresponding to a subnormal glow discharge [8–12] (these oscillations will be described below in more detail). As the power supply voltage decreases further, the oscillatory discharge changes to a Townsend discharge.

Let us draw an analogy with the classification of different regimes of discharges in tubes and propose a classification of the observed regimes of a spherical discharge. It should be remembered that the one-dimensional model under consideration is inapplicable to the description of the normal regime of a glow discharge, when the cathode surface is only partially occupied by
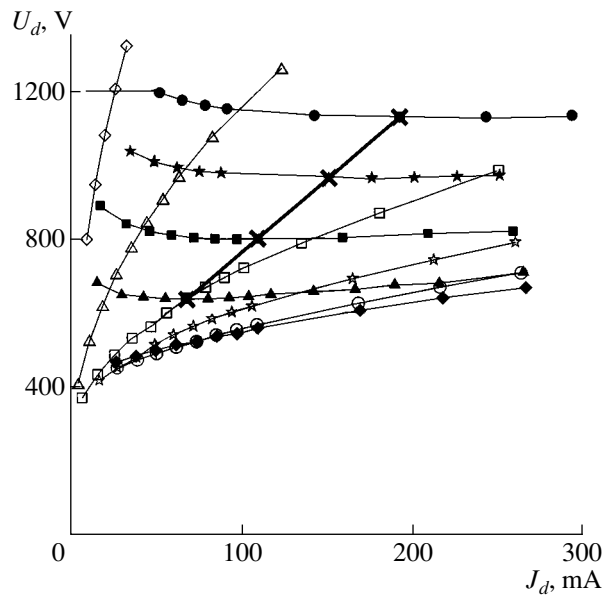


**Fig. 3.** Current–voltage characteristics of a spherical discharge at different nitrogen pressures: ($\diamond$) 0.1, ($\triangle$) 0.2, ($\square$) 0.4, ($\star$) 0.6, ($\circ$) 0.8, ($\blacklozenge$) 1.0, ($\blacktriangle$) 2.0, ($\blacksquare$) 3.0, ($\bigstar$) 4.0, and ($\bullet$) 5.0 torr.

the discharge current. The right branches of the current–voltage characteristics for pressures of $p > 1$ torr and all of the characteristics for pressures below 1 torr correspond to the abnormal regime of a spherical discharge. As the discharge current increases, the discharge voltage increases too. The oscillatory regimes that fall to the left of the minima of the voltage–current characteristics for $p > 1$ torr will be referred to as subnormal regimes. The regime corresponding to a single minimum in the current–voltage characteristic for a given gas pressure will be conventionally referred to as a normal regime.

The phenomena occurring in the cathode sheath play a decisive role in the formation of a glow discharge. In our study, we analyzed the main cathode characteristics of a spherical discharge. The cathode sheath length $d_c$ is most conveniently defined as the distance between the cathode surface and the radius at which the rate of electron-impact ionization of the gas is maximum. The cathode fall voltage $U_c$ was defined as the voltage drop over the cathode sheath length $d_c$.

Figure 4 shows the cathode fall voltage as a function of the product $pd_c$. All of the calculated points are seen to fall on a single curve. Interestingly, all the points corresponding to the normal regime at different pressures turn out to fall in a very narrow parameter range near the point ($U_c = 230 \pm 5$ V, $pd_c = 1.01 \pm 0.05$ torr cm), which is indicated by the cross. All the points corresponding to the abnormal regime fall to the left of this point.

It is well known that, in the case of an abnormal discharge in a tube, the discharge current $J_d$ can be
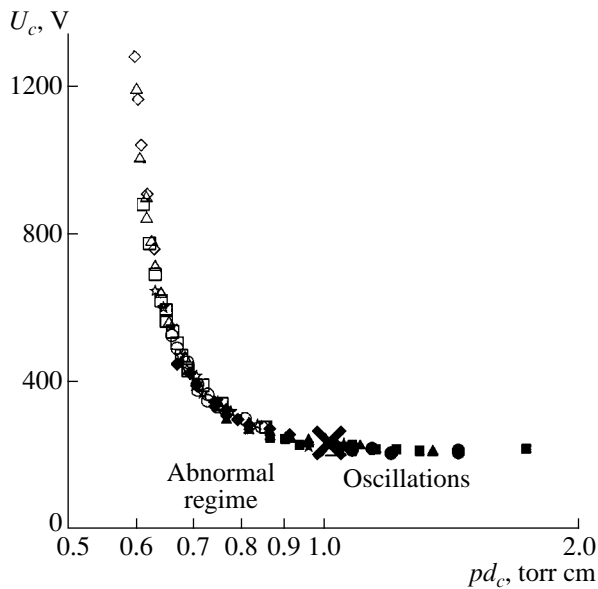
**Fig. 4.** Cathode fall voltage $U_c$ vs. product $pd_c$. The symbols correspond to the same pressures as in Fig. 3.



**Fig. 5.** Dependence of $U_c$ on $j/p^2$. The symbols correspond to the same pressures as in Fig. 3.

increased by increasing the power supply voltage $U_{ps}$ or decreasing the external-circuit resistance $R$. The higher the discharge current $J_d$, the higher the discharge voltage $U_d$. At the same time, the increase in the discharge current is accompanied by an increase in the cathode fall voltage $U_c$ and a decrease in the cathode sheath length $d_c$ [17]. On the other hand, below the so-called normal cathode drop $U_n$, which depends on the sort of gas and the cathode material, the discharge changes to the normal regime, in which $U_c = U_n$ and $pd_c = pd_n$. Hence, in the case of a discharge in a tube, the curve $U_c(pd_c)$ terminates at the point $(U_n, pd_n)$. Nevertheless, the points corresponding to the subnormal regime are shown in Fig. 4. It is worth noting that the farther the point from the normal regime, the more pronounced the oscillations of the discharge parameters.

Figure 5 shows the cathode fall voltage $U_c$ as a function of $j/p^2$. All the data also fall on a single curve. The characteristic value of $j/p^2$ corresponding to the normal regime is equal to $(j/p^2)_n = (7.4 \pm 1.2) \times 10^{-3}$ mA/(cm² torr²). The current density was calculated as the ratio of the current at the cathode to the cathode area. It will be remembered that the current density in discharge tubes is constant over the tube length, whereas the current density in a spherical discharge decreases in inverse proportion to the square of the distance from the anode. If we use the geometric mean of the current density over the gap when calculating the value of $(j/p^2)_n$, then the obtained value $(j/p^2)_n = 0.185$ mA/(cm² torr²) will almost coincide with the usual value of this parameter for nitrogen discharges in tubes.
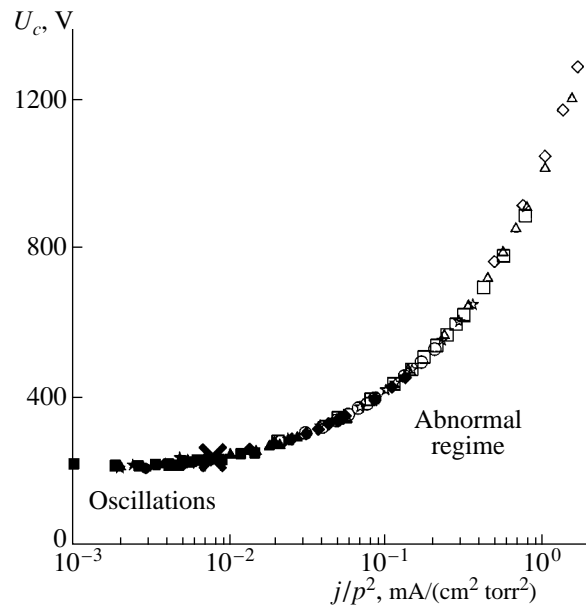
The transition and quenching regimes of the discharge require particular consideration. In numerical simulations, relaxation oscillatory regimes with oscillations of the discharge parameters were observed to the left of the minimum of the current–voltage characteristic. When passing to a new value of $U_{ps}$ at sufficiently high power supply voltages, aperiodic oscillations of the discharge parameters and their subsequent rapid relaxation to new steady-state values are observed. Figure 6 shows an example of such a relaxation of the electric field strength at the cathode at a nitrogen pressure of $p = 3.5$ torr. Curve $1$ corresponds to a change from a power supply voltage of $U_{ps} = 1500$ V to a lower voltage of $U_{ps} = 1400$ V, whereas curve $2$ corresponds to a change from $U_{ps} = 1350$ to 1400 V. It can be seen that the oscillatory transition from different states results in a new steady state that corresponds to a new power supply voltage. The lower the final value of the power supply voltage, the larger the oscillation amplitude and the lower the oscillation frequency and the damping rate. Similar oscillations are also observed in other discharge parameters.

At a certain critical value of the power supply voltage, $U_{ps}^*$, the relaxation oscillatory regime changes to a harmonic undamped self-sustained regime. However, such a transition occurs only at gas pressures higher than a certain critical pressure $p^*$, which depends on the cathode radius. For example, for $R_c = 12.5$ cm and an external-circuit resistance of $R = 20$ kΩ, the critical pressure above which oscillatory regimes are observed is equal to $p^* \approx 1.9$ torr. At this pressure, the critical voltage is $U_{ps}^* \approx 800$ V and the oscillation frequency is
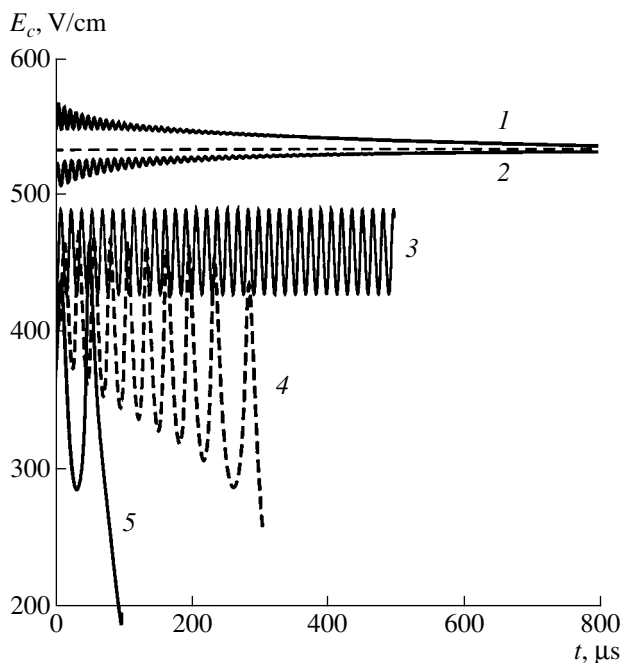
**Fig. 6.** Oscillatory relaxation processes (curves *1–3*) for different $\Delta U_{ps}$ and damped regimes (curves *4, 5*)



**Fig. 7.** Radial profiles of the electric field at instants *1* and *2* with an interval of $\Delta t = 12.5$ μs, corresponding to opposite oscillation phases.

$f \approx 30$ kHz. At a pressure of $p = 3.5$ torr, the critical voltage is $U_{ps}^{*} \approx 1250$ V. This regime is represented by curve *3* in Fig. 6. It can be seen that, under these conditions, almost sinusoidal oscillations with a frequency of $f = 60$ kHz take place.

The mechanism for these oscillations can be interpreted as follows. The ions generated by the electrons in the cathode sheath arrive at the cathode and cause secondary emission. A new portion of the emitted electrons is accelerated in the field of the cathode sheath. The ionization of atoms by these electrons produces a new number of ions moving toward the cathode, and so on. The electron velocity is higher than the ion one; for this reason, the oscillation frequencies ($f \sim 0.1$ MHz) correspond to the time it takes for the ions to move from the center of the cathode sheath to the cathode surface. The oscillation frequency can be estimated as follows:

$$f \approx \langle v_i \rangle / \Delta R_c, \qquad (10)$$

where $\Delta R_c$ is the characteristic length of the cathode sheath, $\langle v_i \rangle \sim \mu_i E_c$ is the ion velocity, and $E_c$ is the electric field in the cathode sheath.

The spatial distributions of the discharge parameters (the total current, the electron density, the electric field, etc.) vary substantially during the oscillation period throughout the entire discharge gap, rather than only in the cathode region. Figure 7 shows the radial distribution of the electric field at two instants with an interval of $\Delta t = 12.5$ μs, corresponding to opposite oscillation phases at $U_{ps} = 1250$ V and $p = 3.5$ torr. The oscillation amplitude of the electric field at the cathode is 30 V/cm
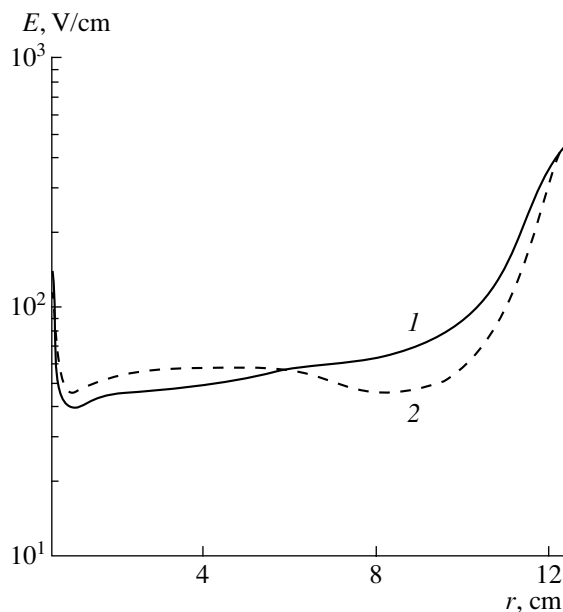
at a mean value of the cathode field $\langle E_c \rangle \approx 456$ V/cm. In the PC, the electric field is on the order of 50 V/cm and its oscillation amplitude is comparable to its mean value. It can be seen that the spatial distributions of the electric field differ substantially at instants corresponding to opposite oscillation phases; i.e., the so-called "breathing" regime of the discharge is realized.

It was found that, in regimes with $U_{ps} \le U_{ps}^{*}(p)$, the second mode of oscillations with a double period arises. The amplitude of this mode increases with increasing $\Delta U_{ps} = U_{ps}^{*}(p) - U_{ps}$. For a gas pressure of $p = 4$ torr, the voltage at which oscillations appear is $U_{ps}^{*} = 1300$ V. Figure 8 shows the oscillations of the electric field at the cathode $E_c(t)$ for $\Delta U_{ps} = 25$ V. The frequencies of the first and second modes of oscillations of all the discharge parameters are $f_1 \approx 45.5$ kHz and $f_2 \approx 22.7$ kHz, respectively. The mechanism for the second-mode generation can be explained as follows. At power supply voltages $U_{ps}$ below the critical value $U_{ps}^{*}(p)$, the cathode sheath length $\Delta R_c$ varies periodically from the minimum to maximum value (twofold for the regime under consideration). The stopping points of the cathode sheath, which occur each half-period of oscillations, correspond to the two frequencies defined by relation (10).

At $U_{ps} < U_{ps}^{*}(p)$, the discharge passes to a damped regime. The cathode sheath becomes substantially wider, the cathode electric field averaged over the oscillation period decreases (the cathode sheath is
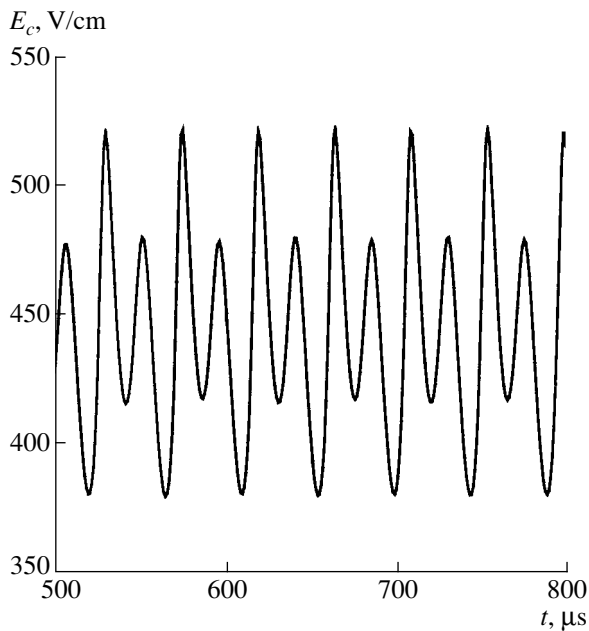
$E_c$, V/cm



**Fig. 8.** Bifurcation of the oscillation period of the electric field at the cathode $E_c(t)$. The curve is a superposition of two modes with the frequencies $f_1 \approx 45.5$ kHz and $f_2 \approx 22.7$ kHz and the amplitudes $E_1 \approx 52$ V/cm and $E_2 \approx 27$ V/cm, respectively.

destroyed), and the period-averaged values of the space charge and current densities decrease over the entire discharge gap. The damping rate of the average current, as well as the amplitude and frequency of oscillations, depends on the value of $\Delta U_{ps} = U_{ps}^*(p) - U_{ps}$. At sufficiently high values of $\Delta U_{ps}$, oscillations become aperiodic and the discharge passes to a Townsend regime (see Fig. 6; curves *4, 5*).

## 4. CONCLUSIONS

A novel numerical method has been elaborated for simulating spherical glow discharges. The model includes time-dependent continuity equations in the drift-diffusion approximation and Poisson's equation for the electric field. The adopted spherical symmetry makes it possible to consider the problem in the one-dimensional approximation.

The time-dependent drift-diffusion model under consideration, which includes the external electric circuit (feedback), is the simplest self-consistent model of a glow discharge. It allows one to consider the entire discharge gap (from the anode to the cathode). The relaxation method used in calculations allows the discharge to either relax to a steady state or to pass to an oscillatory regime. With this model, we have considered the abnormal regime of a spherical glow discharge and determined the main characteristics of this discharge, such as steady-state radial distributions of the space charge, electric field, and potential. On the

whole, the characteristics of a spherical glow discharge correspond to those of classical glow discharges in tubes; in particular, a positively charged cathode sheath with a strong electric field is formed. The main difference from discharges in tubes is that, in a spherical discharge, the space charge in the PC behaves as $\Delta n \propto 1/r$. The relative deviation from neutrality amounts to $\Delta n/n_i \sim 10^{-2}$.

The numerical simulations carried out over a wide range of gas pressures and electric circuit parameters yielded the discharge current–voltage characteristic and the parameters of the cathode sheath. The results obtained also cover the parameter range corresponding to the abnormal regime of a glow discharge. On each of the current–voltage characteristics obtained for different values of the gas pressure, a point corresponding to a transition from the abnormal to the normal regime is determined. Thus, we have obtained the parameter ranges corresponding to the normal characteristics of the cathode sheath: $U_n = 230 \pm 5$ V, $pd_n = 1.01 \pm 0.05$ torr cm, $(j/p^2)_n = (7.4 \pm 1.2) \times 10^{-3}$ mA/(cm$^2$ torr$^2$). We note that the calculated value of $pd_n$ is somewhat higher than the values usually obtained for glow discharges in tubes [1, 17, 18]. The value of the normal current density is almost one order of magnitude lower than that for glow discharges in tubes; this can be explained by the specific features of a spherical discharge. A similar behavior in the cathode characteristics of discharges in tubes was observed experimentally and in numerical simulations [18]. Under certain conditions, oscillations of the plasma parameters arise. This regime lies on the left of the minimum of the current–voltage characteristic. This regime of a spherical discharge was called a subnormal regime.

In the calculations, we observed three types of self-sustained oscillations of a spherical glow discharge: an oscillatory regime, undamped harmonic oscillations of the plasma parameters, and an aperiodic damped regime. Oscillations were observed in all of the plasma parameters throughout the entire discharge gap (from the anode to the cathode). The oscillations are associated with periodic gas ionization in the cathode sheath, ion drift onto the cathode, and secondary emission of electrons from the cathode due to the bombardment by ions. The oscillation frequency lies in the range 10–100 kHz and depends on the gas pressure, the applied voltage, and the length of the discharge gap. Under certain conditions, bifurcation of the oscillation period has been observed. Similar oscillations of the discharge parameters have been observed experimentally in tubes. Various theoretical models have been proposed to explain this effect. In particular, in [8–12, 19], it was pointed out that this effect is two-dimensional in nature and depends on both the area of the region occupied by the current at the cathode and the rate of transverse ion diffusion. The results obtained in our study for a spherical discharge gap show that the oscillations of the discharge current in the parameter range corresponding to

a subnormal discharge can be attributed to the radial ion drift toward the cathode.

To describe the structure of the cathode sheath and to model the effect of stratification of the PC, it is necessary to consider both the electron beam generated in the cathode sheath and nonlocal kinetic processes. The most appropriate method of solving this problem is to use a hybrid model that has been actively developed in recent years (see, e.g., [20–22]). In the hybrid model, the nonlocal Boltzmann equation for the electron distribution function or the Monte Carlo method is used to describe fast electrons. From the electron distribution function determined in this way, one can find the source terms (the ionization rate and inelastic electron energy losses) that are used in the hydrodynamic equations for slow electrons and ions. Apparently, the only way to provide an adequate description of a spherical discharge is to use an approach that simultaneously takes into consideration both the nonlocal kinetic and collective processes in low-temperature plasma.

## ACKNOWLEDGMENTS

## REFERENCES

1. Yu. P. Raizer, *Physics of the Gas Discharge* (Nauka, Moscow, 1987; Springer-Verlag, Berlin, 1991).
2. G. G. Lister, J. Phys. D **25**, 1649 (1992).
3. L. Conde and L. León, Phys. Plasmas **1**, 2441 (1994).
4. B. Song, N. D'Angelo, and R. L. Merlino, J. Phys. D **25**, 938 (1992).
5. O. A. Nerushev, S. A. Novopashin, V. V. Radchenko, and G. I. Sukhinin, Pis'ma Zh. Éksp. Teor. Fiz. **66**, 679 (1997) [JETP Lett. **66**, 711 (1997)].
6. O. A. Nerushev, S. A. Novopashin, V. V. Radchenko, and G. I. Sukhinin, Fiz. Plazmy **26**, 81 (2000) [Plasma Phys. Rep. **26**, 78 (2000)].
7. O. A. Nerushev, S. A. Novopashin, V. V. Radchenko, and G. I. Sukhinin, Phys. Rev. E **58**, 4897 (1998).
8. B. N. Klyarfel'd, L. G. Guseva, and A. S. Pokrovskaya-Soboleva, Zh. Tekh. Fiz. **36**, 704 (1966) [Sov. Phys. Tech. Phys. **11**, 520 (1966)].
9. A. L. Ward and J. Eifionydd, Phys. Rev. **122**, 376 (1961).
10. V. N. Melekhin and N. Yu. Naumov, Zh. Tekh. Fiz. **54**, 1521 (1984) [Sov. Phys. Tech. Phys. **29**, 888 (1984)].
11. V. N. Melekhin, N. Yu. Naumov, and N. P. Tkachenko, Zh. Tekh. Fiz. **57**, 454 (1987) [Sov. Phys. Tech. Phys. **32**, 274 (1987)].
12. I. D. Kaganovich, I. D. Fedotov, and L. D. Tsendin, Zh. Tekh. Fiz. **64** (3), 22 (1994) [Tech. Phys. **39**, 241 (1994)].
13. L. Huxley and R. Crompton, *The Diffusion and Drift of Electrons in Gases* (Wiley, New York, 1974; Mir, Moscow, 1977).
14. W. L. Morgan, J. P. Boeuf, and L. Pitchford, Siglo Data Base, CPAT and Kinema Software, http://www.csn.net/siglo (1998).
15. B. M. Smirnov, *Ions and Excited Atoms in Plasma* (Atomizdat, Moscow, 1974).
16. G. I. Sukhinin and A. V. Fedoseev, Teplofiz. Aeromekh. **10** (1), 63 (2003).
17. V. A. Lisovskiĭ and S. D. Yakovin, Fiz. Plazmy **26**, 1139 (2000) [Plasma Phys. Rep. **26**, 1066 (2000)].
18. A. V. Phelps, Plasma Sources Sci. Technol. **10**, 329 (2001).
19. V. I. Kolobov and A. Fiala, Phys. Rev. E **50**, 3018 (1994).
20. V. A. Shveĭgert and I. V. Shveĭgert, Fiz. Plazmy **14**, 347 (1988) [Sov. J. Plasma Phys. **14**, 204 (1988)].
21. A. Bogaerts and R. Gijbels, J. Tech. Phys. **41**, 183 (2000).
22. Z. Donko, Phys. Rev. E **57**, 7126 (1998).

*Translated by N.F. Larionova*

# Yakov Borisovich Faĭnberg
# (in Honor of His 85th Birthday)

On September 7, 2003, we celebrated the 85th birthday of Yakov Borisovich Faĭnberg, an academician of the National Academy of Sciences of Ukraine. The name of this eminent scientist is inseparably connected with the development of the physics and technology of accelerators, nonrelativistic and relativistic plasma electronics, plasma physics, and controlled fusion research.

In 1940, Faĭnberg graduated from Kharkov State University with a degree in an experimental speciality, Electronuclear Physics. He took part in World War II. After demobilization, he began work at the Theoretical Department of the Kharkov Institute of Physics and Technology (KhIPT). To put his ideas into practice and to prove them experimentally, in 1957, Faĭnberg became head of the experimental laboratory and, in 1972, the experimental–theoretical department.

His more than half a century of scientific activity is indissolubly linked to the KhIPT. He carried out fundamental studies on the theory of linear accelerators. His pioneering works (together with works by V.P. Veksler and G.I. Budker) laid the foundations for the collective methods of acceleration. Modifications of the method of charged-particle acceleration proposed by Faĭnberg have been widely adopted and are now considered the most promising among the new methods of acceleration. Based on his theoretical investigations and calculations, the first linear electron accelerators in the Soviet Union were built at the KhIPT. Under his leadership, the theory of high-energy linear accelerators was developed. In particular, the calculations were performed for the 2-GeV linear accelerator (the largest in Europe), which was built at the KhIPT. Faĭnberg proposed and implemented a number of new ideas in this field, in particular, a fundamentally new method for the simultaneous radial and longitudinal stabilization of particles in a linear accelerator—the so-called method of alternating phase focussing. Based on this method, new types of linear ion accelerators were developed. In 1996, his work was awarded the Ukraine State Prize in Science and Technology.

Faĭnberg contributed significantly to plasma physics. The studies carried out by him and his colleagues resulted in the development of a new branch of plasma physics—nonrelativistic and relativistic plasma electronics. In 1948, he (together with A.I. Akhiezer) described and investigated the beam–plasma instability, the most widely occurring microinstability of a nonequilibrium plasma. It is difficult to overestimate the importance of this result, which has already become classical and is included in each monograph on plasma physics. He and his pupils were the first to observe beam–plasma instability and to develop methods for controlling it. They were the first to discover a new type of gas discharge, the beam–plasma discharge, and developed a new collisionless method for plasma heating—beam heating.

Together with his colleagues, he carried out the first theoretical and experimental investigations of the interaction of relativistic electron beams with plasmas and demonstrated that this interaction is very efficient. These investigations led to the development of a new line of research—relativistic plasma electronics—which resulted in the creation of high-power microwave oscillators and lasers.

Faĭnberg also made a great contribution to the development of fundamentally new high-current inductive plasma accelerators of electrons and ions.

In his scientific work, fundamental studies have always been closely connected with applied problems (in particular, defense problems). It should be noted that, under his leadership, very effective defense systems were developed for the Defense Ministry. Faĭnberg has conducted important organizing work: he is the chairman of the Scientific Council on Plasma Electronics and New Acceleration Methods of the National Academy of Sciences of Ukraine. He created a powerful scientific school of plasma electronics and new methods of acceleration (more than 25 doctors and 35 candidates of sciences), which is now well known all over the world. For more than 25 years, he conducted pedagogical work at Kharkov State University, at which he created special courses on accelerator physics, plasma physics, and plasma electronics. For his major contributions to science and the training of qualified specialists, Honored Scientist of Ukraine Ya.B. Faĭnberg was awarded the Order of the Red Banner of Labor and a number of medals.

The scientific community heartily congratulates Yakov Borisovich on his eighty fifth birthday and wishes him good health and many years of fruitful work and creative achievement.

=========== **TOKAMAKS** ===========

# Real-Time Determination of the Position and Shape of the Plasma Column from External Magnetic Measurements in the GLOBUS-M Tokamak

**V. M. Amoskov\*, V. A. Belyakov\*, S. E. Bender\*, V. K. Gusev\*\*, A. A. Kavin\*, E. A. Lamzin\*, R. G. Levin\*\*, S. N. Sadakov\*, N. V. Sakharov\*\*, S. E. Sychevskiĭ\*, and O. G. Filatov\***

*\*Federal State Unitary Enterprise Efremov Scientific Research Institute of Electrophysical Apparatus, Sintez Scientific and Technical Center, St. Petersburg, 196641 Russia*
*\*\*Ioffe Physicotechnical Institute, Russian Academy of Sciences, St. Petersburg, 194021 Russia*
Received January 29, 2003; in final form, April 28, 2003

**Abstract**—A fast algorithm is elaborated for determining the position and shape of the plasma column from measurements performed with magnetic probes located outside the vacuum vessel of the GLOBUS-M tokamak. The algorithm is based on the modeling of the plasma current by movable current filaments and allows one to take into account the effect of eddy currents induced in the vacuum vessel. The algorithm was tested in a series of model discharges under conditions characteristic of the GLOBUS-M tokamak and serves now as a software component of its magnetic diagnostic system. By employing a conventional PC (Pentium 1 GHz, 200-MHz data bus), the calculation time of the plasma column parameters at one instant in time does not exceed 3 ms, which offers the possibility of controlling the plasma parameters during a discharge. © 2003 MAIK "Nauka/Interperiodica".

## 1. INTRODUCTION

One of the main problems in the magnetic diagnostics of plasmas in present-day tokamaks is the real-time acquisition of data on the position and shape of the plasma column for the purpose of controlling the plasma, as well as the determination of certain equilibrium plasma parameters (the ratio of the gas-kinetic plasma pressure to the pressure of the poloidal magnetic field, the internal inductance, etc.). The theoretical grounds of the magnetic diagnostic technique were laid by L.E. Zakharov and V.D. Shafranov (see, e.g., [1]). Quite soon, a wide range of magnetic diagnostic methods for tokamak plasma were formulated mathematically and implemented in the form of computer codes (see [2, 3]). Since that time, the methods of magnetic diagnostics have been mainly developed toward the optimization of the computational accuracy and speed. The problems of magnetic diagnostics can be placed among the so-called inverse problems of mathematical physics [4, 5], which significantly complicates the arrangement of the calculation process and calls for applying a regularization procedure.

Most of the magnetic diagnostic methods are based on an a priori parametrical representation of the plasma flux function and differ only in the form of representation. The parameters of any specific representation are obtained by minimizing the discrepancy between the measured and calculated plasma parameters. Generally speaking, each method exploits its own set of the measured parameters. Computer codes based on the models of a continuous plasma distribution are generally the

most accurate but least rapid. Moreover, they are rather cumbersome. They are mainly applied to the analysis of the discharge in pauses between shots (the so-called off-line mode).

To quickly determine the plasma parameters, including the position and shape of the plasma column, one needs simplified models (methods). Simple models are of especial necessity in resolving the problem of controlling the plasma discharge in real time (the on-line mode), when the computational speed becomes of crucial importance (the characteristic calculation times should not exceed several milliseconds). An analysis of the available methods for determining the position of the plasma boundary from external magnetic measurements that are appropriate for real-time plasma control and enable the required accuracy in reconstructing the plasma boundary shows that such methods are very limited in number (see review [6]).

The method of harmonics [7–12] is based on the expansion (generally in toroidal geometry) of the flux function in terms of the eigenfunctions of the Grad–Shafranov differential operator. The parameters to be determined are the radius of the base circle of the toroidal coordinate system and the coefficients by several first harmonics.

In the method of a local approximation [7, 13–15], the flux function is represented by a segment of a Tailor expansion in the vicinity of some characteristic points in the plasma, i.e., only some of the most important (from the standpoint of controlling) points of the plasma boundary (rather than the entire boundary) are

determined. The model parameters to be determined are the coefficients in the Tailor series.

The method of a simple-layer potential [16–18] is based on the replacement of the plasma column with a closed surface that is located inside the plasma and does not necessarily coincide with the plasma boundary. The whole of the plasma current is assumed to flow along this surface. The model parameters are related to the location of this surface.

The method of current filaments is based on a model representation of the plasma current as a system of a few thin ring currents. Within this model, one can distinguish two methods that differ in the set of parameters to be reconstructed. In the method of fixed current filaments, one needs to determine only the magnitudes of the ring currents, whereas the location of the current filaments is given [10, 15, 19–21]. In the method of movable current filaments [15, 22, 23], it is necessary to determine both the current magnitudes and the coordinates of the current filaments. The latter method seems to be the most efficient in terms of a compromise between computational speed and accuracy in reconstructing the plasma boundary. It is this method that will be discussed in detail in this paper.

The purpose of our study is to develop a numerical simulation technique and an algorithm for determining the position and shape of the plasma column in tokamaks, including those with strongly elongated plasma cross sections and divertor configurations. The problem should be resolved on the basis of the data from external magnetic measurements, with allowance for the screening effect of eddy currents induced in the vacuum vessel of a tokamak. As applied to the GLOBUS-M tokamak [24–26], we should limit ourselves to the data from the magnetic probes placed exclusively outside the vacuum vessel.

An important additional requirement is that the algorithm should be sufficiently fast for it to be applied to real-time data processing (on-line mode). This means that the data should be acquired over a time period on the order of a few milliseconds (less than 3 ms for the GLOBUS-M tokamak). The developed algorithm meets this condition when being implemented with a conventional PC (Pentium 1 GHz, 200-MHz data bus). This provides the possibility of controlling the plasma discharge in the GLOBUS-M tokamak. However, application of the results obtained to the problem of active plasma control is beyond the scope of this study.

Based on the algorithm proposed, the ROMS (Reconstruction of Magnetic Surfaces) code was developed. It is quite universal and can be applied to different facilities of the tokamak type. The ROMS code has been tested in a series of model calculations of plasma discharges in the ITER and GLOBUS-M tokamaks and serves as a software component of the magnetic diagnostic system of the GLOBUS-M.

In this paper, we present the results of testing the algorithm for numerically reconstructing the position and shape of the plasma column boundary with allowance for eddy currents under conditions typical of the GLOBUS-M tokamak.

## 2. FORMULATION OF THE PROBLEM

Figure 1 presents the main notations and outlines a cross section of the GLOBUS-M tokamak in the plane $\varphi$ = const of a cylindrical coordinate system ($r$, $\varphi$, $z$). It is assumed that all the physical quantities possess axial symmetry (do not depend on $\varphi$).

The vectors of the plasma current density **j** and magnetic field **B** can be decomposed into the sum of poloidal and toroidal components:

$$\mathbf{B} = \mathbf{B}_p + B_\varphi \mathbf{e}_\varphi,$$

$$\mathbf{j} = \mathbf{j}_p + j_\varphi \mathbf{e}_\varphi.$$

The poloidal magnetic field $B_p$ measured by the probes is a superposition of the fields produced by the plasma current, poloidal coils, and eddy currents induced in the vacuum vessel. The poloidal magnetic field is measured by a set of $N_p$ two-component magnetic probes placed along the vacuum vessel wall (beyond the region occupied by the plasma) and constituting the measuring contour $L$.

The poloidal components of the current and magnetic field are represented by the two scalar functions $\psi$ and $F$ in the form [27]

$$\mathbf{B}_p = \frac{1}{2\pi r} \nabla \psi \times \mathbf{e}_\varphi,$$

$$\mathbf{j}_p = \frac{1}{2\pi r} \nabla F \times \mathbf{e}_\varphi,$$

where the functions $\psi$ and $F$ are related to the toroidal components of the vector potential $A_\varphi$ and magnetic field $B_\varphi$ via the relations (in CGS units)

$$\psi = 2\pi r A_\varphi,$$

$$F = \frac{cr}{2} B_\varphi,$$

and represent the total magnetic flux and total current through a ring loop with coordinates $r$ and $z$.

An equilibrium plasma in a strong magnetic field is described by the well-known set of the ideal magnetohydrodynamic (MHD) equations [27]

$$\begin{cases} \nabla \times \mathbf{B} = \dfrac{4\pi}{c} \mathbf{j} \\[2mm] \nabla \cdot \mathbf{B} = 0 \\[2mm] \nabla p = \dfrac{1}{c} \mathbf{j} \times \mathbf{B}, \end{cases} \quad (1)$$
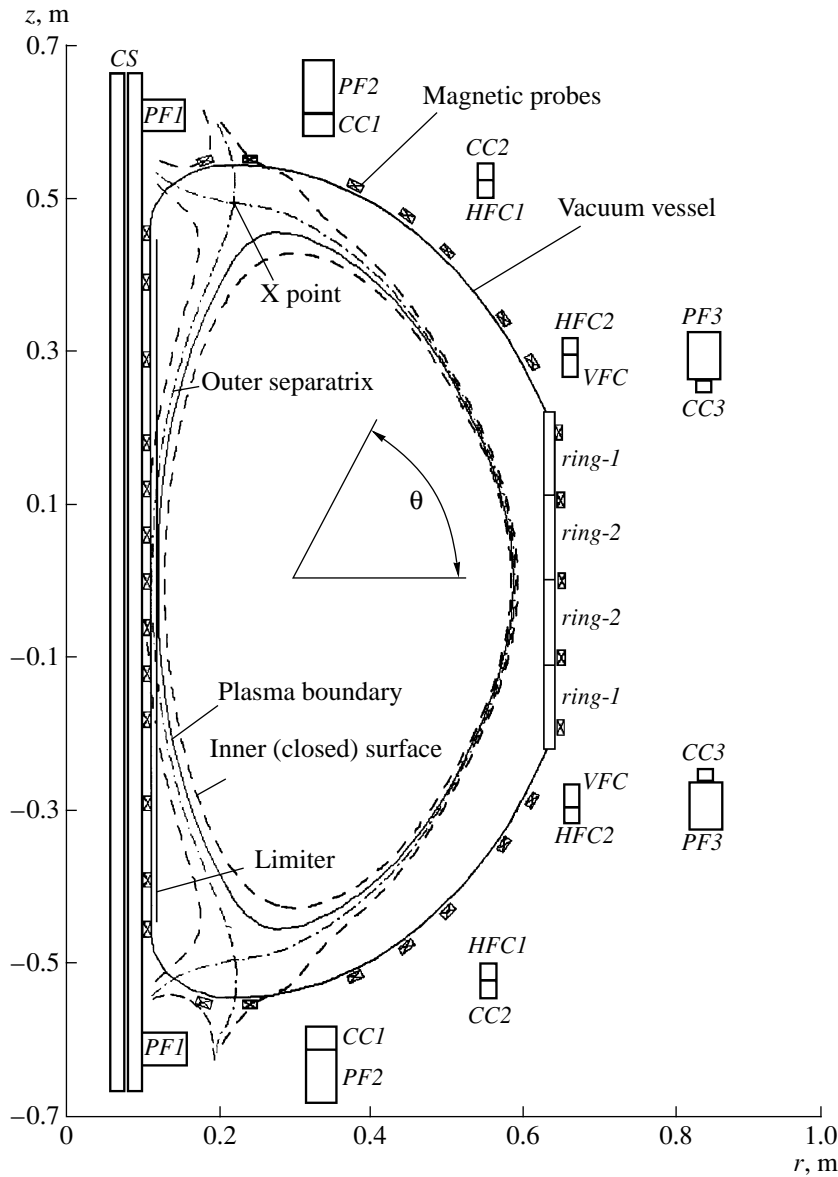
**Fig. 1.** Schematic of the plasma control system of the GLOBUS-M tokamak and the boundary of the limiter plasma for $I_p = 176$ kA. The solid line shows the limiter plasma boundary, $\psi/\psi_{lim} = 1$. The dashed lines show the surfaces $\psi/\psi_{lim} = 1 \pm 0.03$. The dashed-and-dotted line shows the outer separatrix, $\psi/\psi_{lim} = 0.9873$.

where $p$ is the gas-kinetic plasma pressure and **j** is the plasma current density. Equations (1) describe the equilibrium of a real plasma with macroscopic parameters varying slowly in time [1, 28, 29].

In the case of axial symmetry, Eqs. (1) reduce to the equation for the flux function $\psi$,

$$\Delta^*\psi = r^2\nabla \cdot \left(\frac{\nabla\psi}{r^2}\right)$$

$$= \frac{\partial^2\psi}{\partial r^2} - \frac{1}{r}\frac{\partial\psi}{\partial r} + \frac{\partial^2\psi}{\partial z^2} = -\frac{8\pi^2}{c}rj_\varphi,$$

(2)

which is known in the theory of MHD plasma equilibrium as the Grad–Shafranov equation. Here,

$$j_\varphi(r, z) = 2\pi cr\frac{dp}{d\psi} + \frac{2F}{cr}\frac{dF}{d\psi}$$

is the density of the toroidal plasma current.

In terms of the flux function, the problem of determining the plasma boundary reduces to finding a magnetic surface defined by the equation $\psi(r, z) = \psi_0$, where $\psi_0$ is the magnetic flux (i) at the point of contact between the limiter and the plasma $(r_{lim}, z_{lim})$ for a limiter configuration and (ii) at the X point $(r_s, z_s)$ for a divertor configuration (hereafter, the data related to the

limiter and separatrix are marked with indices lim and *s*, respectively). Such a magnetic surface is usually referred to as the outermost magnetic surface.

It is known [29] that, in tokamaks, surfaces with $\psi > \psi_0$ are always closed and located inside the outermost magnetic surface. To illustrate, Fig. 1 shows the contour of the outermost magnetic surface $\psi(r, z) = \psi_0 = \psi_{lim}$ (solid line) for a limiter plasma configuration and the contour $\psi/\psi_0 = 1.03$ (the closed dashed line within the contour of the outermost magnetic surface). The contours are calculated using the PET MHD equilibrium code [30]. The contour $\psi = \psi_S$ corresponds to the separatrix, which, in this case (the limiter regime), is not the outermost magnetic surface determining the plasma boundary. In Fig. 1, the contours corresponding to $\psi/\psi_0 \approx 0.9873$ (the separatrix) and $\psi/\psi_0 = 0.97$ (the outer open dashed line) are also shown.

The outermost magnetic surface (the plasma boundary) is determined as follows:

(i) Based on the results of external observations, the required set of parameters that determine the mathematical model of plasma in an approximation adopted for describing physical phenomena under consideration is sought. Since the problem of reconstructing the field sources by the fields they produce is an inverse problem of mathematical physics—one which reduces to the Cauchy problem for elliptic equations, and various parametric plasma models are generally used to resolve it. Here, we use a model in which the plasma current is represented by a discrete set of movable current filaments (see Section 3). The parameters to be determined are the coordinates of these current filaments and the and currents in them.

(ii) For a known set of external currents at a certain instant, the plasma configuration (the limiter or divertor one) and the base point $(r_0, z_0)$ lying on the outermost magnetic surface are determined. This point is the limiter contact point for a limiter configuration and the X point for a divertor configuration. First, the X point is deduced from the condition $|\mathbf{B}_p| = 0$. If the condition $\psi(r_S, z_S) > \psi(r_{lim}, z_{lim})$ is satisfied for all the points of the limiter, then we have a divertor configuration; otherwise, we have a limiter configuration, determined by the point $(r_{lim}, z_{lim})$ in which the magnetic flux is maximum.

(iii) Knowing the flux function $\psi_0 = \psi(r_0, z_0)$ at one point on the outermost magnetic surface, one can reconstruct the entire surface consisting of the points $(r, z)$ determined by the equation $\psi(r, z) = \psi_0$.

To calculate the flux function at the observation point $(r, z)$ and the magnetic field produced at this point by the current ring with coordinates $(r_c, z_c)$ and the current $I_c$, the following relations are used [27]:

$$\psi(r, z) = 8\pi \frac{I_c}{c} \frac{\sqrt{r_c r}}{k}\left(\left(1 - \frac{k^2}{2}\right)K(k) - E(k)\right),$$

$$B_r(r, z) = \frac{I_c}{c}\frac{z_c - z}{r}2k\sqrt{r_c r}\left(\left(1 - \frac{k^2}{2}\right)E(k) - K(k)\right),$$

$$B_z(r, z) = \frac{I_c}{c}2k\sqrt{r_c r}\left(\frac{r - r_c}{r}\left(1 - \frac{k^2}{2}\right)E(k) - K(k)\right),$$

$$k^2 = \frac{4r_c r}{(r_c + r)^2 + (z_c - z)^2},$$

where $K(k)$ and $E(k)$ are complete elliptic integrals of the first and second kind, respectively. In order to reduce the computation time, they are calculated using the Landen transformation.

## 3. METHOD OF MOVABLE CURRENT FILAMENTS

In this study, the algorithm for reconstructing the plasma boundary is based on the method of movable current filaments and is aimed at using it in real time. It was proposed in [15, 22] and is described in detail in [23].

Here, we suggest that the field of the plasma current can be deduced from the magnetic measurements, assuming the currents in the external conductors are known (the fields of these currents are determined numerically). Provided that the plasma field is smooth enough, this procedure enables the required accuracy of calculating the relevant circulation integrals along the measuring loop. The algorithm of taking into account the eddy currents induced in the vacuum vessel will be discussed in Section 4.

Using the above introduced Grad–Shafranov operator $\Delta^*$ (2), we can use the so-called second Green formula for arbitrary functions $u$ and $v$ [31]:

$$\int_{(S)} r^{-1}(u\Delta^* v - v\Delta^* u)dS = \oint_{(L)} r^{-1}\left(u\frac{\partial v}{\partial n} - v\frac{\partial u}{\partial n}\right)dl, \quad (3)$$

where $S$ is a two-dimensional area in the plane $\varphi = $ const and $L$ is the smooth boundary of this area. In what follows, by $L$ we mean a closed measuring loop passing through all the magnetic probes.

Using the latter formula for the two arbitrary functions $u = \chi$ and $v = \psi$ satisfying the equations $\Delta^*\chi = 0$ and $\Delta^*\psi = -(8\pi^2/c)rj_\varphi$, we obtain the following relation [32]:

$$\int_{(S)} \chi j_\varphi dS = \frac{c}{8\pi^2} \oint_{(L)} r^{-1}\left(\psi\frac{\partial \chi}{\partial n} - \chi\frac{\partial \psi}{\partial n}\right)dl.$$

Using a linear combination of the normal and tangential components of the poloidal magnetic field ($B_n = \frac{1}{2\pi r}\frac{\partial \psi}{\partial \tau}$ and $B_\tau = -\frac{1}{2\pi r}\frac{\partial \psi}{\partial n}$, respectively), this identity can be rewritten in the form [32]

$$\int_{(S)} \chi j_\varphi dS = \frac{c}{4\pi} \oint_{(L)} (\xi B_n + \chi B_\tau)dl, \quad (4)$$

where $\xi$ is a function conjugated with $\chi$ and defined by the equation $\nabla(r^{-1}\xi) = \nabla\chi \times \nabla\varphi$. It can be shown [32] that the function $\xi$ satisfies the equation $\Delta(r^{-1}\xi) = 0$, where $\Delta$ is the Laplacian in cylindrical coordinates.

The plasma current can be represented as a discrete set of $N$ circular current filaments, each of which is characterized by the two coordinates $r_i$ and $z_i$ and the current magnitude $I_i$, where $i = 1\ldots N$. The total plasma current is

$$I_p = \int_{(S)} j_\varphi dS = \sum_{i=1}^{N} I_i.$$

Hence, the problem reduces to determining the coordinates of the current filaments and the currents in them at a given instant.

If we choose the function $\chi$ in the form of homogeneous polynomials,

$$\chi_m(r, z) = \sum_{k=0}^{[n/2]} \frac{(m-1)!/2}{k!(k+1)!(m-2k-1)!} r^{2+2k} z^{m-2k-2},$$

then the functions $\chi_m$ conjugated with $\xi_m$ are [2, 32]

$$\xi_m(r, z) = \sum_{k=0}^{[n+1/2]} \frac{m!}{k!k!(m-2k-2)!} r^{1+2k} z^{m-2k-1}.$$

The moments of the toroidal current density in plasma, $Y_m$, are related to the pair of functions $\chi_m$ and $\xi_m$ by the relationship

$$Y_m = \int_{(S)} j_\varphi \chi_m dS = \oint_{(L)} (B_\tau \chi_m + B_n \xi_m) dL, \qquad (5)$$

where $S$ is the area enclosed by the measuring loop $L$ and $B_\tau$ and $B_n$ are the field components tangential and normal to this loop.

For a system of current filaments, the distribution of the current density $j_\varphi(r, z)$ can be represented via the $\delta$ functions in the form

$$j_\varphi(r, z) = \sum_{i=1}^{N} I_i \delta(r - r_i, z - z_i).$$

Therefore, Eq. (5) takes the form

$$\sum_{i=1}^{N} I_i \chi_m(r_i, z_i) = Y_m, \qquad (6)$$

where the moments of the current density $Y_m$ are calculated via circulation integrals (5).

For a single current filament ($N = 1$) and corresponding pairs of the functions $\chi$ and $\xi$, the moments of the current density have a clear physical meaning. For the normalized (generally, to the major radius of the torus)

values of $r$ and $z$, these moments can be calculated in the explicit form [32]

$$I_1 = I_p = Y_0 = \frac{c}{4\pi} \int_{(L)} B_\tau dl,$$

$$z_1 = Y_1 = \frac{c}{4\pi I_p} \oint_{(L)} (-r\ln r B_n + z B_\tau) dl,$$

$$r_1^2 = Y_2 = \frac{c}{4\pi I_p} \oint_{(L)} (2rz B_n + r^2 B_\tau) dl.$$

The moment $Y_0$ represents an integral form of Maxwell's equation and allows one to find the total plasma current. Using the moments $Y_1$ and $Y_2$, one can find the mean vertical coordinate and the mean major radius of the plasma column.

It is reasonable to use the above solution for $N = 1$ to determine the shape of an arbitrarily shifted plasma column with a nearly circular cross section (in particular, in the initial stage of the discharge [22]).

To determine the shape of an elongated plasma column, a larger number of current filaments is required. However, the increase in the order of the current density moment (and, thus, the degree of polynomials $\chi_m$ and $\xi_m$) drastically aggravates the conditionality of the set of Eqs. (6), which adversely affects both the computation accuracy and time.

For these reasons, the following two-step algorithm was proposed in [23]. At the first step, the currents are assumed to be known and the coordinates $r_i$ and $z_i$ of all the current filaments are determined by solving the set of Eqs. (6). At the second step, the current amplitudes are determined by minimizing the residual functional between the calculated and measured poloidal field components at the measuring loop. The procedure is repeated until a self-consistent solution with the required accuracy is obtained.

In this study, we implemented the following algorithm: To solve the set of Eqs. (6), we choose a certain initial approximation $(r_i^0, z_i^0)$ and start the iteration process on the basis of the Newton method. Let the pairs of coordinates $(r_i^p, z_i^p)$ be known on the $p$th iteration step. To obtain the $(p + 1)$th iteration $(r_i^{p+1} = r_i^p + \Delta r_i, z_i^{p+1} = z_i^p + \Delta z_i)$, one needs to solve the following set of linear algebraic equations for $\Delta r_i$ and $\Delta z_i$:

$$\sum_{i=1}^{N} \frac{I_i}{I_p} \left( \frac{\partial \chi_m(r_i^p, z_i^p)}{\partial r} \Delta r_i + \frac{\partial \chi_m(r_i^p, z_i^p)}{\partial z} \Delta z_i \right)$$

$$= Y_m - \sum_{i=1}^{N} \frac{I_i}{I_p} \chi_m(r_i^p, z_i^p),$$

$$m = 1\ldots 2N.$$

The solution is assumed to be found when the prescribed accuracy criterion, $\max_i(|\Delta r_i|, |\Delta z_i|) < \varepsilon$, is achieved. It should be noted that the derivatives in the latter expression are determined analytically since the functions $\xi$ and $\chi$ are known polynomials.

At the second step, the currents in the filaments are determined. The currents are found by minimizing the residual functional $W$,

$$W = \sum_{i=1}^{K}\{(B_i^{(n)} - \overline{B_i^{(n)}})^2 + (B_i^{(\tau)} - \overline{B_i^{(\tau)}})^2\}, \qquad (7)$$

where $B_i^{(\tau)}$, $B_i^{(n)}$ and $\overline{B}_i^{(\tau)}$, $\overline{B}_i^{(n)}$ are the calculated and measured field components, respectively, at $K$ points on the measuring loop. The coordinates of the current filaments are assumed to be known.

The algorithm uses certain initial values of the coordinates of all the filaments and currents in them. Given the currents, the solution of the set of Eqs. (6) by the Newton method provides new coordinate values. Given the coordinates, the minimization of residual functional (7) provides new values of the current in the filaments. The iteration process is repeated as long as the residual functional decreases. In the general case, taking into account the inexactness of the initial data that stems from magnetic measurement errors, model approximation errors, and rounding-off errors, a generalized solution reaching the minimum of functional (7) is sought [4, 5]. After the second stage is completed, both the coordinates of all the current filaments and the currents in them turn out to be found.

We note that, under real experimental conditions, it makes sense to use the data on the plasma column parameters obtained at the previous instant of time as an initial approximation to calculate these parameters at the next instant. Such a "tracking" regime significantly reduces the computation time, which is the most crucial requirement for algorithms operating in real time.

Based on the calculated coordinates of the filaments and the currents in them, and taking into account the contributions from the poloidal coils and eddy currents, the points lying on the outermost magnetic surface $\psi(r, z) = \psi_0$ are determined.

Based on this algorithm, the ROMS computer code was developed. At the stage of testing the algorithm and software, the reconstructed outermost magnetic surface was compared to the test plasma boundary obtained using the PET equilibrium code [30]. Figure 2 shows typical results of the reconstruction of the plasma boundary (for a divertor configuration, as an example) for different numbers of the current filaments. As a criterion, one can use the maximum local deviation $\Delta_{max}$ between the reconstructed and test outermost magnetic surfaces (the solid and dashed lines, respectively), i.e., the max-norm $\|\cdot\|_\infty$. The data presented in Fig. 2 (as well

as similar data from other numerical simulations) show that it is quite sufficient to use three to four current filaments to model the plasma current.

Figure 3 presents the field maps obtained using the equilibrium code (Fig. 3a) and the model of three current filaments (Fig. 3b). It can be seen that, in Figs. 3a and 3b, the contours of the module of the poloidal magnetic field are nearly identical beyond the vacuum vessel, in the region where the magnetic probes are located. As the plasma boundary is approached, a slight discrepancy arises. Finally, inside the plasma, the field structure provided by the model is completely incorrect.

Figure 3 can serve to illustrate a doubt frequently discussed in the literature about the possibility of reconstructing the plasma current profile (as well as the pressure profile, etc.) based exclusively on the data from external magnetic measurements (see, e.g., [33]). However, this doubt certainly does not apply to the possibility of determining the position and shape of the plasma column from magnetic measurements. Indeed, the boundary of a divertor plasma in Figs. 2 (for $N = 3$) and 3b is correctly determined using only three current filaments.

To conclude this section, we note that (in our opinion) the relation between the method of fixed current filaments, in which the filament positions are prescribed, and the method of movable current filaments can be likened to the relation between the methods of the Newton numerical integration, in which the nodes are fixed, and the Gauss methods, in which both the nodes and the coefficients in quadrature formulas are to be found. The reason why the number of elementary currents used in the method of movable current filaments is significantly less than that in the methods using fixed current filaments lies in the fact that not only the currents in the filaments (the analogue of the coefficients in quadrature formulas) but also the filament positions (analogue of the quadrature nodes) must be determined.

## 4. ALGORITHM FOR TAKING EDDY CURRENTS INTO ACCOUNT

Taking into account that the magnetic probes measure the total magnetic field produced by the plasma, poloidal coils, and eddy currents induced in the vacuum vessel, the correct determination of the parameters of the adopted model of the plasma current distribution requires extracting the component directly related to the plasma contribution from these measurement results. Evaluating the contribution from the poloidal coils presents no difficulties because the currents in the coils are measured and the coil positions are known. Below, we describe the algorithm for taking into account the effect of eddy currents induced in the vacuum vessel. To verify the algorithm and software, we performed a set of test calculations of the discharge
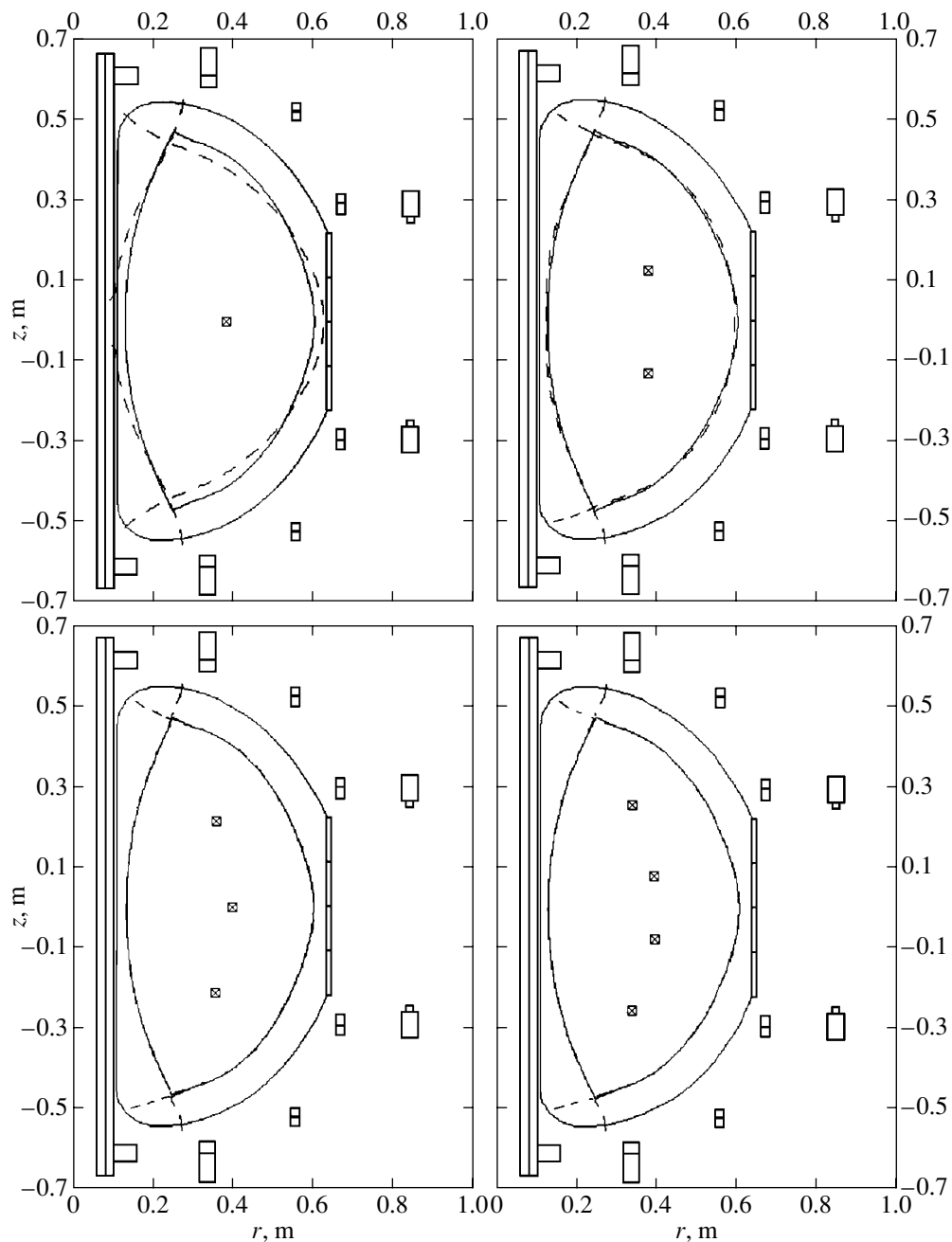
**Fig. 2.** Reconstruction of the boundary of a divertor plasma in the GLOBUS-M tokamak by the ROMS code for different numbers of the current filaments (shown by crossed squares). The solid line shows the plasma boundary calculated by the PET MHD equilibrium code, and the dashed line shows the reconstructed plasma boundary.

behavior with allowance for eddy currents. Figure 4 shows the calculated time evolution of the plasma column shape within the time interval 10–40 ms (from the onset of the discharge) with a time step of 3 ms. Figure 5 shows the calculated dynamics of the plasma current and the total eddy current induced in the vacuum vessel during the discharge. Only the initial stage of the discharge, during which the effect of eddy current is maximum, was considered.

The vortex e.m.f. induced along the major circumference of the torus was measured by seven toroidal loops that were set along the wall of the vacuum vessel of the GLOBUS-M tokamak (Fig. 4). To take into account the effect of eddy currents, the vacuum vessel was modeled by a finite set of conducting rings located along the vessel wall coaxially with the major axis of the torus. Eddy currents induced in these rings act as extra sources of the magnetic field (in addition to the
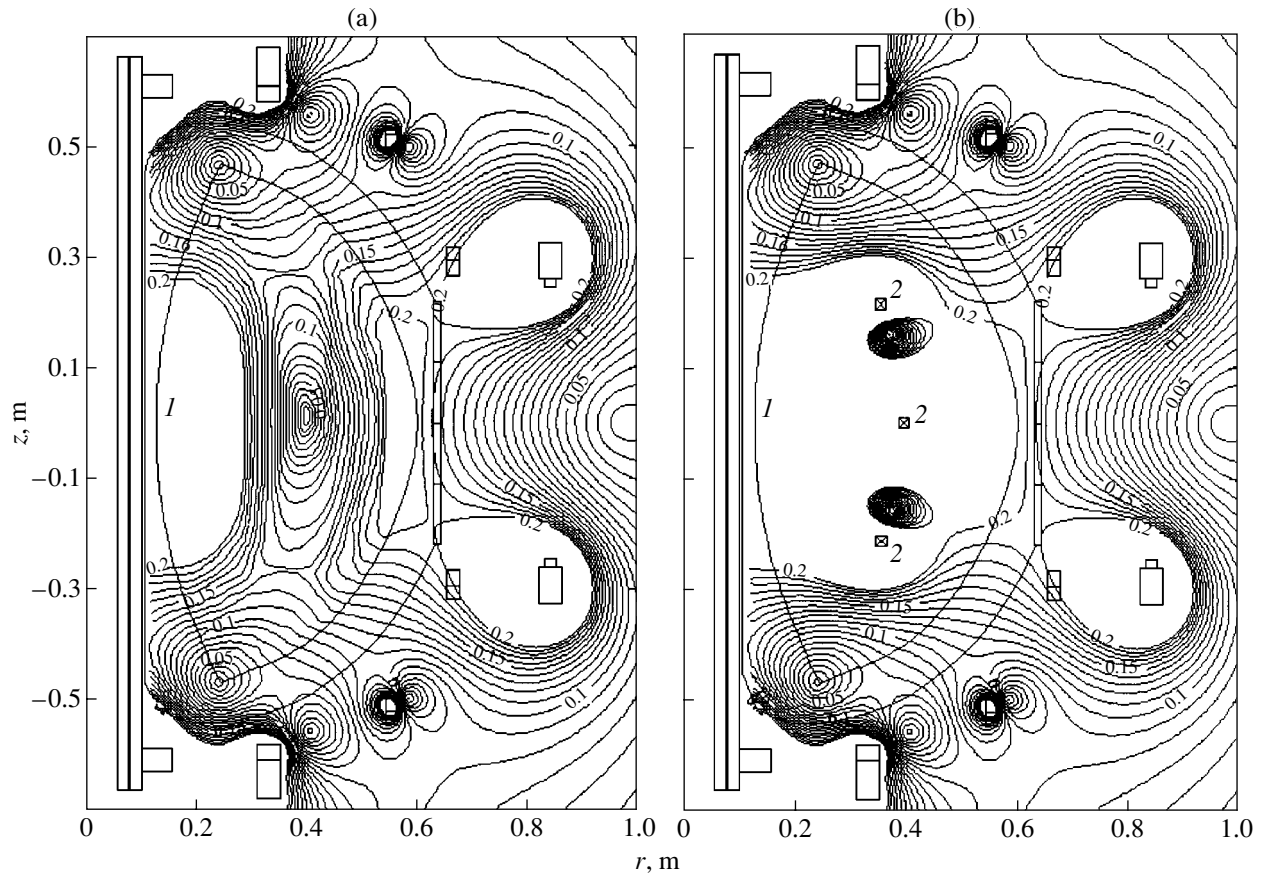
**Fig. 3.** Isolines of the module of the poloidal magnetic field $|\mathbf{B}_p| = \sqrt{B_r^2 + B_z^2}$ calculated for (a) the test (continuous) divertor plasma and (b) the model with three current filaments. Only the range of relatively weak fields $|\mathbf{B}_p| \leq 0.2T$ is shown. The separatrix and current filaments are marked *1* and *2*, respectively.

poloidal coils and plasma current). The discrete axisymmetric model of the vacuum vessel used in the simulations is shown in Fig. 6. There are no conducting rings near the equatorial plane at the outer side of the vessel; this is related to the presence of relatively large horizontal ports in this region. In the model, this region is considered nonconducting. The analysis of eddy currents with allowance for three-dimensional effects can be performed using the numerical simulation technique proposed in [34]. The vessel model shown in Fig. 6 is probably nonoptimal. It will be further refined using the results of simulations with allowance for the calculated spatial distribution of eddy currents in the vessel.

For a sufficiently large number of the conducting rings modeling the vacuum vessel, we can assume that the current distribution in each ring is uniform. Then the total current flowing through the a given ring is equal to

$$I_l^{vv} = \frac{U_l^{vv}}{R_l}.$$

Here, $U_l^{vv}$ is the voltage along the major circumference of the torus for the $l$th conducting ring and $R_l$ is its resistance,

$$R_l = \rho_0 \frac{2\pi r_l}{\Delta r_l \Delta z_l},$$

where $r_l$ is the mean radius of the $l$th ring, $\Delta r_l \Delta z_l$ is the ring cross-sectional area, and $\rho_0$ is the resistivity of the vacuum vessel. It was assumed that $\rho_0 = 0.7 \times 10^{-6}$ Ohm m, which corresponded to the resistivity of stainless steel.

The resistance of each conducting ring modeling the vacuum vessel was calculated in advance and was assumed to be constant during the entire discharge phase.

The vortex e.m.f. induced in any conducting ring can be found by interpolating the signals from the toroidal loops measuring the e.m.f. along the major circumference of the torus.

The solid lines in Fig. 7 show the eddy current distributions computed using the PET code for two different instants [30]. The dashed lines show the current dis-
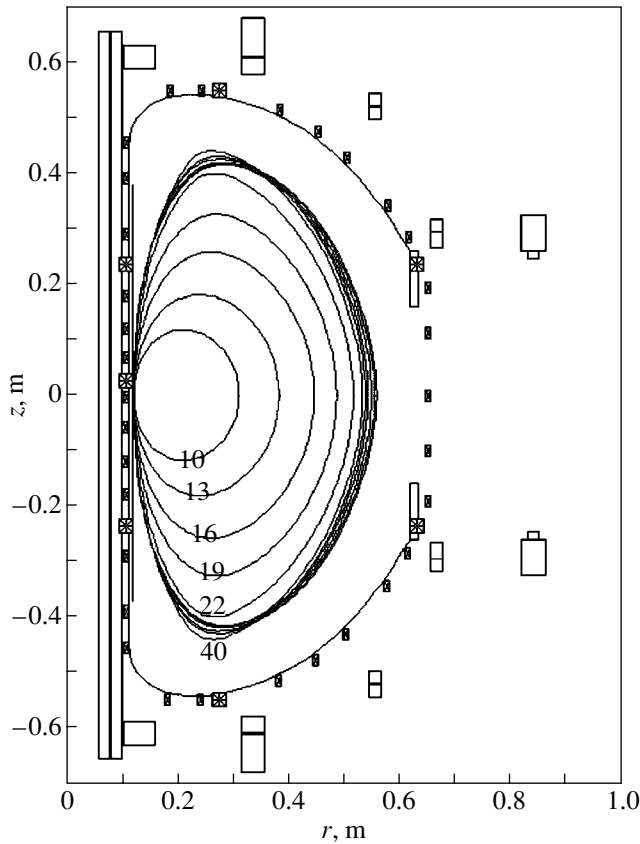
**Fig. 4.** Calculated time evolution of the plasma discharge in the GLOBUS-M tokamak. Closed solid lines show the positions of the outermost magnetic surface (plasma boundary) within the time interval 10–40 ms (from the onset of the discharge). The numerals by the lines show the time (in ms).

tributions calculated under the assumption that the vortex e.m.f. is uniform. The dashed-and-dotted lines show the eddy current distributions obtained by the linear interpolation

$$U_l = \frac{L_{l2}}{L_{12}} U_1 + \frac{L_{l1}}{L_{12}} U_2,$$

where indices 1 and 2 refer to the toroidal loops neighboring to the $l$th conducting ring, $L_{12}$ is the distance between the toroidal loops measured along the vessel wall, and $L_{l1}$ and $L_{l2}$ are the distances from the $l$th conducting ring to the corresponding toroidal loops.

An analysis of Fig. 7 shows that the linear interpolation is quite adequate for describing the eddy current distribution.

## 5. RESULTS OF NUMERICAL SIMULATIONS AND TESTING THE ALGORITHM

First, we investigated the possibility of reconstructing the outermost magnetic surface (plasma boundary) in the GLOBUS-M tokamak using the algorithm based
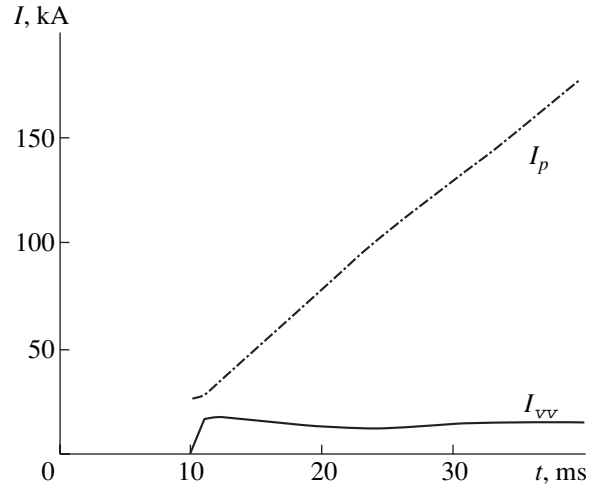
**Fig. 5.** Calculated time evolution of the plasma current $I_p$ (dashed-and-dotted line) and the total eddy current $I_{vv}$ induced in the vacuum vessel (solid line).

on the method of movable current filaments for the instants at which the effect of eddy currents induced in the vessel can be ignored (see Fig. 2) [35]. The measuring loop was composed of 32 two-component magnetic probes. A circular cubic spline was used to provide the required smoothness of the contour passing through these probes when calculating circulation integrals (5).

The results of these investigations are as follows [35]:

(i) For the measuring system of the GLOBUS-M tokamak, assuming that the magnetic measurement error is zero, it is sufficient to use three to four current filaments in order to reconstruct the plasma boundary with an error less than 5 mm. At the very beginning of the discharge, when the plasma column is almost circular, two (or even one) current filaments are quite sufficient. We note that the reduction in the number of the current filaments significantly increases the computation speed.

(ii) The accuracy of reconstructing the boundary of a strongly elongated limiter plasma is generally worse than that of a divertor plasma because the field gradient in the limiter point $(r_{\lim}, z_{\lim})$ is usually higher than that in the X point (Fig. 1).

(iii) When the calculated field components at the location points of the magnetic probes contain a perturbation caused by standard random error with an r.m.s. deviation of $\sigma = 2\%$, the maximum error (by the maxnorm) in reconstructing the outermost magnetic surface increases to 10 mm. For $\sigma = 5\%$, this error increases to 20 mm.

We then studied the possibility of reconstructing the outermost magnetic surface in the initial stage of the discharge, when the effect of eddy currents is maximum (Figs. 4, 5).
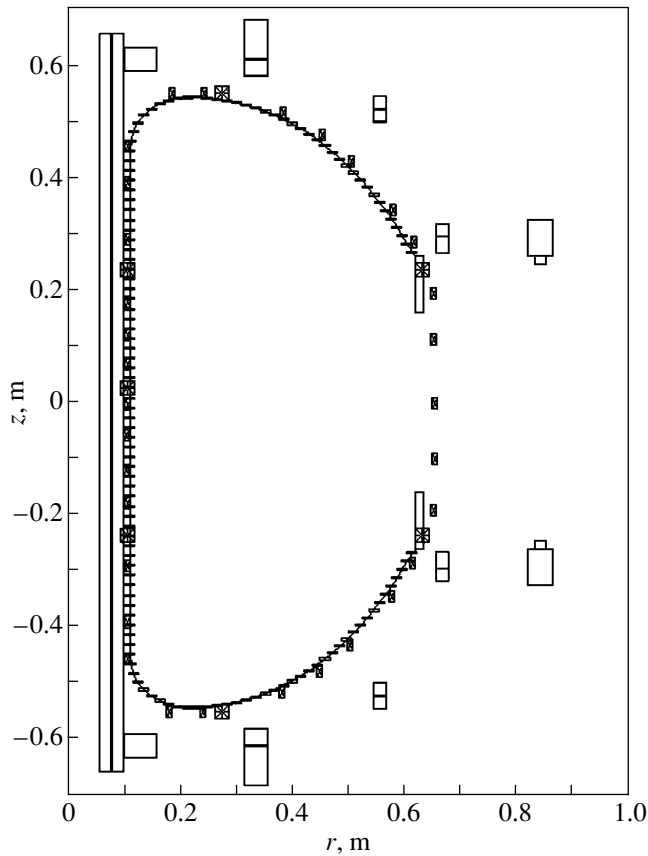
**Fig. 6.** Axisymmetric vacuum vessel model containing 128 conducting rings with rectangular cross section for taking eddy currents into account. The solid line corresponds to the medial line of the vacuum vessel wall.



**Fig. 7.** Profiles of the eddy current density in the vacuum vessel vs. the poloidal angle $\theta$ (see Fig. 1) for the times $t =$ 19 and 40 ms from the onset of the discharge. The solid lines show the eddy current profiles calculated by the PET code, the dashed lines show the profiles calculated under the assumption that e.m.f. is uniform along the poloidal circumference of the vessel, and the dashed-and-dotted lines correspond to the linear interpolation of the vortex e.m.f. between the toroidal loops.

Figure 8 shows the results of reconstructing the position and shape of the plasma column with allowance for eddy currents induced in the vacuum vessel for four characteristic instants of the discharge evolution presented in Fig. 4. The plasma current is modeled by three current rings. A random error corresponding to a normal distribution with $\sigma = 2\%$ around the exact field value was artificially introduced in the magnetic fields at the measurement points.

The characteristic time over which the position and shape of the plasma column should be controlled is on the order of several milliseconds. This time sets the requirements for the computation speed of the controlling algorithm. We note, however, that for a real or calculated plasma discharge, the data obtained at the previous instant can be used as an initial approximation for the current instant. This makes it possible to restrict oneself to only one iteration step when determining the positions of the current filaments and the currents in them at each time step without loss of accuracy in reconstructing the plasma boundary. Estimates of the algorithm speed with the use of a conventional PC (Pentium 1 GHz, 200-MHz data bus) showed that the
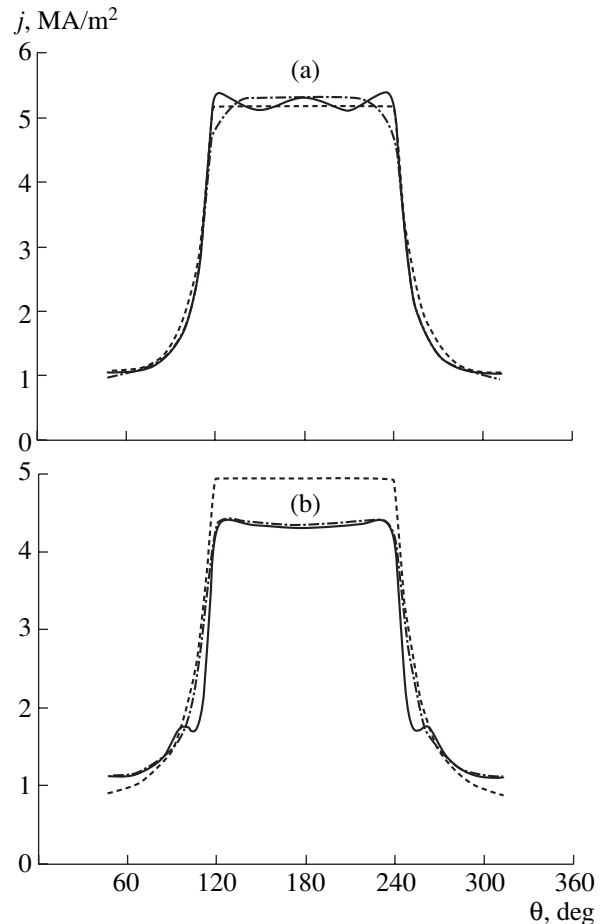
calculation time of the plasma column position in such a tracking regime was less than 3 ms, which offers the possibility of controlling the plasma parameters during the discharge.

Eddy currents are of significance in the initial stage of the discharge, when the plasma current is low and the plasma column is only slightly elliptic. In this case, the plasma boundary can be quite satisfactorily determined using a single movable current filament, in which case the computation speed increases due to the simplicity of the model. As the ellipticity of the plasma column increases with time (to $k > 1.2$), the required accuracy in reconstructing the plasma boundary can be provided for quite varied column shapes by employing a model with two to three movable current filaments.
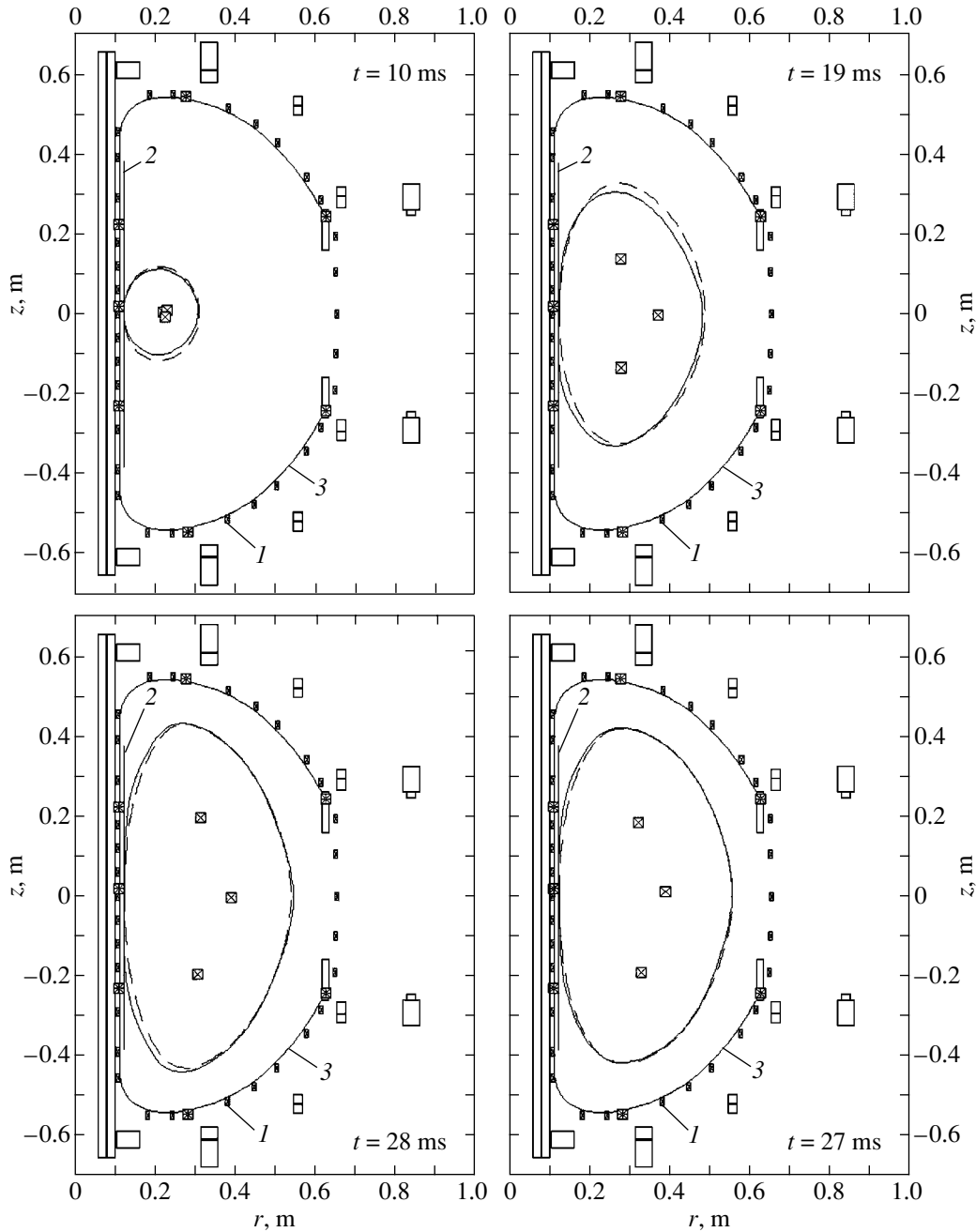
**Fig. 8.** Outermost magnetic surface reconstructed using the model of three current filaments, with allowance for eddy currents induced in the vacuum vessel of the GLOBUS-M tokamak in the case of a limiter plasma: (*1*) magnetic probes, (*2*) limiter, and (*3*) vacuum vessel. The current rings are shown by crossed squares, and the toroidal loops are shown by asterisked squares. A random error with $\sigma = 2\%$ is artificially introduced in the magnetic field at the measurement points. The dashed lines show the outermost magnetic surface calculated by the PET code for the instants $t = 10$, 19, 28, and 37 ms from the onset of the discharge. The solid line shows the reconstructed outermost magnetic surface for $I_p = 26$, 72, 119, and 162.7 kA and $\Delta_{max} \approx 2$, 6, 8, and 7 mm, respectively.

## 6. CONCLUSIONS

(i) Based on the method of movable current filaments, an algorithm and software have been proposed that allow the real-time determination of the position and shape of the plasma column from external magnetic measurements. The algorithm takes into account eddy currents induced in the vacuum vessel using the data from toroidal loops on the distribution of the vortex e.m.f. along the poloidal circumference of the vessel.

(ii) The algorithm and software have been tested under conditions typical of the GLOBUS-M tokamak

and serve as a software component of its magnetic diagnostic system. The algorithm is quite universal: it is almost independent of the type of measurement system and can be applied to other magnetic confinement facilities.

(iii) Using the above algorithm, the following problems have been resolved in the preliminary stage of investigations: (a) the determination of the required number of magnetic probes and toroidal loops and the optimization of their locations and (b) the analysis of the influence of random measurement error on the accuracy with which the plasma boundary is determined.

(iv) It has been shown that, under conditions typical of the GLOBUS-M tokamak, the time required to compute the plasma boundary from external magnetic measurements with the help of a conventional PC amounts to ~3 ms (further progress in PC performance will naturally reduce this time). The algorithm satisfies the requirement that the error in determining the plasma boundary be less than a few millimeters. This allows one to use the algorithm for real-time control of the tokamak plasma for the purpose of sustaining a stable plasma column inside the vacuum vessel throughout the entire discharge phase.

(v) The software developed can also be used to calculate the main integral equilibrium plasma parameters (plasma current $I_p$, poloidal beta $\beta_p$, linear internal plasma inductance $l_i$, etc.) in pauses between shots.

## REFERENCES

1. L. E. Zakharov, and V. D. Shafranov, in *Reviews of Plasma Physics*, Ed. by M. A. Leontovich (Énergoatomizdat, Moscow, 1982; Consultants Bureau, New York, 1986), Vol. 11.

2. B. J. Braams, Preprint No. IPP 5/2 (Max Planck Institut für Plasmaphysik, Garching, 1985).

3. B. J. Braams, Plasma Phys. Controlled Fusion **33**, 715 (1991).

4. A. N. Tikhonov and V. Ya. Arsenin, *Solutions of Ill-Posed Problems* (Nauka, Moscow, 1986; Halsted Press, New York, 1977).

5. M. M. Lavrent'ev, V. G. Romanov, and S. P. Shishatskiĭ, *Ill-Posed Problems of Mathematical Physics* (Nauka, Moscow, 1980; American Mathematical Society, Providence, 1986).

6. Yu. K. Kuznetsov, Fiz. Plazmy **20**, 132 (1994) [Plasma Phys. Rep. **20**, 122 (1994)].

7. D. K. Lee and Y.-K. M. Peng, J. Plasma Phys. **25**, 161 (1981).

8. Yu. K. Kuznetsov and A. M. Naboka, Fiz. Plazmy **7**, 860 (1981) [Sov. J. Plasma Phys. **7**, 474 (1981)].

9. B. Ph. Van Milligen, Nucl. Fusion **30**, 157 (1990).

10. G. N. Deshko, T. G. Kilovataya, Yu. K. Kuznetsov, *et al.*, Nucl. Fusion **23**, 1309 (1983).

11. S. P. Bondarenko, V. E. Golant, M. P. Gryaznevich, *et al.*, Fiz. Plazmy **10**, 910 (1984) [Sov. J. Plasma Phys. **10**, 520 (1984)].

12. K. Kurihara, Fusion Technol. **22**, 334 (1992).

13. F. Hofmann and G. Tonetti, Nucl. Fusion **28**, 519 (1988).

14. D. P. O'Brien, J. J. Ellis, and J. Lingertat, Nucl. Fusion **33**, 467 (1993).

15. A. O. Kaminskiĭ, T. G. Kilovataya, Yu. K. Kuznetsov, and I. V. Yasin, Fiz. Plazmy **20**, 143 (1994) [Plasma Phys. Rep. **20**, 133 (1994)].

16. W. Feneberg, K. Lancker, and P. Martin, Comput. Phys. Commun. **31**, 143 (1984).

17. P. N. Vabishchevich and I. V. Zotov, Fiz. Plazmy **13**, 649 (1987) [Sov. J. Plasma Phys. **13**, 373 (1987)].

18. A. G. Dmitrienko, Yu. K. Kuznetsov, and A. I. Fesenko, Fiz. Plazmy **18**, 1515 (1992) [Sov. J. Plasma Phys. **18**, 785 (1992)].

19. A. J. Wootton, Nucl. Fusion **19**, 987 (1979).

20. D. W. Swain and G. H. Neilson, Nucl. Fusion **22**, 1015 (1982).

21. L. L. Lao, H. St. John, R. D. Stambaugh, *et al.*, Nucl. Fusion **25**, 1611 (1985).

22. Yu. K. Kuznetsov, V. N. Panov, and I. V. Yasin, Preprint No. 85-1, Kharkov Institute for Physics and Technology (Tsniiatominform, Moscow, 1985).

23. I. V. Yasin, Candidate's Dissertation (Kharkov, 1992).

24. V. K. Gusev, V. E. Golant, E. Z. Gusakov, *et al.*, Zh. Tekh. Fiz. **69** (9), 58 (1999) [Tech. Phys. **44**, 1054 (1999)].

25. V. K. Gusev, Plasma Devices Op. **9** (1–2), 1 (2001).

26. N. V. Sakharov, Plasma Devices Op. **9** (1–2), 25 (2001).

27. L. D. Landau and E. M. Lifshitz, *Electrodynamics of Continuous Media* (Nauka, Moscow, 1982; Pergamon, New York, 1984).

28. B. B. Kadomtsev, in *Reviews of Plasma Physics*, Ed. by M. A. Leontovich (Gosatomizdat, Moscow, 1963; Consultants Bureau, New York, 1963), Vol. 2.

29. V. D. Shafranov, in *Reviews of Plasma Physics*, Ed. by M. A. Leontovich (Gosatomizdat, Moscow, 1963; Consultants Bureau, New York, 1966), Vol. 2.

30. S. A. Galkin, A. A. Ivanov, S. Yu. Medvedev, and Yu. Yu. Poshekhonov, Nucl. Fusion **37**, 1455 (1997).

31. V. S. Vladimirov, *Equations of Mathematical Physics* (Nauka, Moscow, 1981; Marcel Dekker, New York, 1971).

32. L. E. Zakharov and V. D. Shafranov, Zh. Tekh. Fiz. **43**, 225 (1973) [Sov. Phys. Tech. Phys. **18**, 151 (1973)].

33. V. D. Pustovitov, Nucl. Fusion **41**, 721 (2001).

34. A. Belov, V. Belyakov, V. Kokotkov, *et al.*, Plasma Devices Op. **8** (2), 79 (2000).

35. V. Amoskov, V. Belyakov, S. Bender, *et al.*, Plasma Devices Op. **9** (9), 159 (2001).

*Translated by N.N. Ustinovskiĭ*